

Electronic Thesis and Dissertation Repository

1-9-2018 10:00 AM

Photocatalytic Hydrogen Production using a Mesoporous TiO₂ Doped with Pt: Semiconductor Synthesis, Oxidation-Reduction Network and Quantum Efficiencies.

Jesus Fabricio Guayaquil-Sosa
The University of Western Ontario

Supervisor

Hugo de Lasa

The University of Western Ontario Joint Supervisor

Benito Serrano Rosales

The University of Western Ontario

Graduate Program in Chemical and Biochemical Engineering

A thesis submitted in partial fulfillment of the requirements for the degree in Doctor of Philosophy

© Jesus Fabricio Guayaquil-Sosa 2018

Follow this and additional works at: <https://ir.lib.uwo.ca/etd>

 Part of the [Catalysis and Reaction Engineering Commons](#)

Recommended Citation

Guayaquil-Sosa, Jesus Fabricio, "Photocatalytic Hydrogen Production using a Mesoporous TiO₂ Doped with Pt: Semiconductor Synthesis, Oxidation-Reduction Network and Quantum Efficiencies." (2018). *Electronic Thesis and Dissertation Repository*. 5191.
<https://ir.lib.uwo.ca/etd/5191>

This Dissertation/Thesis is brought to you for free and open access by Scholarship@Western. It has been accepted for inclusion in Electronic Thesis and Dissertation Repository by an authorized administrator of Scholarship@Western. For more information, please contact wlsadmin@uwo.ca.

Abstract

The present PhD dissertation establishes that hydrogen can be produced using mesoporous TiO₂ as a photocatalyst, doped with platinum atoms (Pt), in a slurry medium, under near-UV irradiation and with ethanol as a sacrificial reagent (scavenger). These mesoporous TiO₂ photocatalysts were prepared using a sol-gel method. The mesoporous Pt-TiO₂ photocatalyst displayed a reduced 2.34 eV band gap compared to the bare TiO₂ (3.20 eV).

Photocatalytic hydrogen production experiments were performed in a Photo-CREC Water II Reactor (PCW-II Reactor). This novel unit provides both radial and axial symmetrical irradiation profiles. Furthermore, macroscopic energy balances developed in this unit, showed a maximum 96% light absorption efficiency.

Runs in the PCW-II Reactor showed that hydrogen molecules were formed through the coupling of H[•] radicals under oxygen-free conditions. The use of 2.00 v/v% ethanol as a sacrificial reagent enabled the production of significant amounts of hydrogen with the simultaneous formation of hydrogen peroxide, methane, ethane, acetaldehyde and carbon dioxide by-products. It was confirmed that the extent of hydrogen generation in the presence of ethanol is a function of the pH level and Pt loading on the mesoporous TiO₂ photocatalyst.

Additionally, it was established that the reaction networks leading to hydrogen production, using the various photocatalysts, shared common reactivity features. For example, it was shown that under an inert gas atmosphere, ethanol consumption takes place sub-stoichiometrically. This points towards the simultaneous formation and consumption of ethanol. Regarding the consumption of the ethanol scavenger, experimental observations were supported by an “in series-parallel” reaction network. With respect to energy efficiencies, it was observed that the maximum 22.6 % Quantum Yields found for hydrogen generation indicates a very good degree of photon utilization (45.2%).

Thus, this PhD dissertation contributes to the development of novel semiconductors for hydrogen production via water dissociation. It is demonstrated that when using the synthesized mesoporous semiconductors with added Pt, in a Photo-CREC-Water II Reactor unit, encouraging Quantum Yields are achieved.

Keywords

Photo-CREC-Water II Reactor, Heterogeneous Photocatalysis, Platinum, TiO₂, Hydrogen production, Quantum Yield.

Co-Authorship Statement

This PhD thesis encloses materials that are published in peer reviewed journals as listed below.

CHAPTER 4

Title of the paper: Photocatalytic hydrogen production using mesoporous TiO₂ doped with Pt.

Authors: Jesús Fabricio Guayaquil Sosa, Benito Serrano Rosales, Patricio Valadés Pelayo and Hugo de Lasa.

Status: Published.

Journal: Applied Catalysis B: Environmental.

Author contributions: Fabricio conceived and designed the experiments, wrote a draft of the paper, contributed by modifying the manuscript and its revisions, performed experiments as well as data analyses. Dr. Serrano assisted with the manuscript writing process. Dr. Valadés helped with the methodology for calculating the optical energy band gaps of synthesized materials. Dr. de Lasa edited and provided the final revision of the manuscript.

Reference: Guayaquil-Sosa, J.F.; Serrano-Rosales, Benito; Valadés-Pelayo, P.J.; de Lasa, H.; Photocatalytic Hydrogen Production using Mesoporous TiO₂ Doped with Pt, *Applied Catalysis B: Environmental*, 2017, 7, 337-348, doi.org/10.1016/j.apcatb.2017.04.029.

CHAPTER 5

Title of the Paper: Hydrogen Production via Water Dissociation Using Pt–TiO₂ Photocatalysts: An Oxidation–Reduction Network.

Authors: Jesús Fabricio Guayaquil Sosa, Alan Calzada, Benito Serrano Rosales, Salvador Escobedo and Hugo de Lasa.

Status: Published.

Journal: Catalysts.

Author Contributions: Fabricio conceived and designed the experiments, wrote a draft of the paper, contributed by modifying the manuscript and its revisions, performed experiments as well as data analyses. Alan Calzada contributed to the synthesis of the impregnated materials and Salvador Escobedo facilitated with the storage hydrogen tank. Dr. Serrano and Dr. de Lasa edited and provided the final revision of the manuscript.

Reference: Guayaquil-Sosa, J.F.; Calzada, A.; Serrano, B.; Escobedo, S.; de Lasa, H. Hydrogen Production via Water Dissociation Using Pt–TiO₂ Photocatalysts: An Oxidation–Reduction Network. *Catalysts* 2017, 7, 324. doi:10.3390/catal7110324.

Acknowledgments

First, my honest appreciation is to Dr. Hugo de Lasa for putting his trust on me. Also for being a very supportive supervisor and admirable professor. His superior standards, constant inspiration, and priceless suggestions made my PhD thesis possible.

I especially thank Professor Benito Serrano for his assistance and friendship during my PhD.

I also wish to extend my sincere respect and thankfulness to my dear friends Dr. Jesus Moreira and Dr. Aaron Ortiz, for their invaluable support in Canada.

I would like to extend my sincere gratitude to my colleague Dr. Kyriakos Manoli for sharing his scientific knowledge with me.

Remarkable thanks to all my friends I met in Canada; Hussein Mahmoud, Lin Su, Hai Su, Yolanda Echeverria, Jimena de la Pena, Rob Lin, Yira Aponte, Angel Lanza, Jose Munoz, Dr. Sameer Al-Ghamdi, Camila Jeres, Nazanin Afghan, Pablo Vizcarra, Jaime Ontiveros, Danielle Luskind, Orelie van Geenhoven, Samira Rostom, Imtiaz Ahmed, Ines Griffoux, Juan Lacayo, Amanda Taylor, Reyna Gomez, Isabella Reinati, Medhavi Gupta, Cindy Torres.

Very sincere thanks to my favourite fellow TA, Daria Popugaeva. I enjoyed our 1050 courses together. Also, I really appreciate your assistance at all time.

I also thank Ying Zhang and Pastor Solano for their technical support in the laboratory. Helping me understand the different principles of a variety of analytical techniques.

I am grateful to my best friends in Mexico; Dr. Gamaliel Che, Helena Aranda, Dr. Omar Castillo, Rocio Villalobos, Dr. Patricio Valadés and Monica Gonzalez. Their invaluable friendship helped for the successful achievement of my PhD.

I would like to thank The National Council of Science and Technology in Mexico (CONACyT) for the scholarship that permitted me to pursue my PhD abroad.

Lastly, and most importantly, this PhD thesis is dedicated to my beloved parents, Hector Guayaquil Arias and Rosa Sosa Gomez, whose love, motivation and work example have been key in my life. Likewise, this effort is committed to my brothers, Hector and Gustavo, who have played an important role in my life.

Table of Contents

Abstract.....	i
Co-Authorship Statement.....	iii
Title of the paper: Photocatalytic hydrogen production using mesoporous TiO ₂ doped with Pt.	iii
Title of the Paper: Hydrogen Production via Water Dissociation Using Pt–TiO ₂ Photocatalysts: An Oxidation–Reduction Network.	iv
Acknowledgments.....	v
Table of Contents.....	vi
List of Tables.....	x
List of Figures.....	xi
Nomenclature.....	xxi
Chapter 1.....	1
1.1 General Objectives.....	4
1.2 References.....	5
Chapter 2.....	7
2 Literature Review.....	7
2.1 Hydrogen from the Dissociation of Water.....	8
2.1.1 Water Electrolysis.....	8
2.1.2 Photobiological Production (bio-photolysis).....	8
2.1.3 Decomposition of Water at High Temperatures.....	9
2.1.4 Thermo-chemical Process.....	9
2.1.5 Photolysis.....	10
2.2 Hydrogen Production via Photocatalysis.....	10
2.2.1 Photoreactor Configurations.....	15
2.2.2 Photo-CREC Water Reactor II.....	18
2.2.3 Photocatalyst Selection for Hydrogen Production.....	20

2.2.4	Mesoporous Titanium Dioxide (TiO ₂) Semiconductor.....	22
2.2.5	Band Gap Energy	25
2.2.6	Porosity and Porous Materials	28
2.2.7	Mesoporous Nanostructured TiO ₂	30
2.3	Block co-polymers, Pluronic P123 and Pluronic F127.....	38
2.4	Quantum Efficiency	40
2.4.1	Maximum Expected Quantum Yields.....	43
2.4.2	Quantum Efficiencies and Quantum Yields (QY).....	46
2.5	Previous Works in the Reactor Photo-CREC Water II.....	47
2.6	Scope of thesis	48
2.7	References.....	49
Chapter 3.....		67
3	Synthesis of Mesoporous Pt Doped TiO ₂ with Block Co-polymers Pluronic P123 and Pluronic F127 as Templates for Photocatalytic Hydrogen Generation.....	67
3.1	Introduction.....	67
3.2	Experimental.....	69
3.3	Characterization	69
3.3.1	N ₂ Adsorption-Desorption Isotherms	70
3.3.2	XRD Diffractograms.....	76
3.3.3	Scanning Electron Microscopy (SEM).....	81
3.4	Photocatalytic Hydrogen Production via Water Dissociation using Mesoporous TiO ₂	85
3.5	Conclusions.....	92
3.6	References.....	93
Chapter 4.....		94
4	Photocatalytic Hydrogen Production Using Mesoporous TiO ₂ Doped with Pt.....	94
4.1	Introduction.....	94

4.2	Photocatalyst Engineering	96
4.3	Experimental Methods	96
4.3.1	Preparation of Mesoporous Titania Nanoparticles	96
4.3.2	Photocatalytic Performance	97
4.3.3	Apparatus	98
4.4	Photocatalyst Characterization.....	99
4.4.1	XRD diffractograms.....	99
4.4.2	N ₂ adsorption-desorption isotherms of mesoporous TiO ₂	101
4.4.3	X-ray photoelectron spectroscopy (XPS)	104
4.4.4	Band gap	105
4.4.5	Scanning electron microscopy (SEM)	112
4.5	Hydrogen Production via Water Splitting.....	113
4.6	Quantum Yields (QYs)	114
4.7	Conclusions.....	115
4.8	References.....	116
	Chapter 5.....	122
5	Hydrogen Production via Water Dissociation Using Pt–TiO ₂ Photocatalysts: An Oxidation–Reduction Network	122
5.1	Introduction.....	122
5.2	Quantum Efficiencies.....	123
5.3	Experimental Methods	124
5.3.1	Photocatalyst Preparation of Pt/TiO ₂	125
5.4	Photocatalytic Reactor	126
5.5	Analytical Methods.....	128
5.6	Photocatalyst Characterization.....	128
5.7	Photocatalytic Reaction Mechanism for Hydrogen Production.....	136

5.8 Hydrogen Formation with Ethanol Scavenger.....	140
5.9 Quantum Yields for Different Semiconducting Materials.....	147
5.10 Conclusions.....	149
5.11 References.....	150
Chapter 6.....	152
6 Conclusions and Recommendations	152
6.1 Conclusions.....	153
6.2 Future Work	154
Appendices.....	155
Appendix A - Supplementary material of Chapter 3	155
Appendix B - Supplementary material of Chapter 4.....	165
Appendix C - Supplementary material of Chapter 4.....	166
Appendix D - Supplementary material of Chapter 4 and 5.....	169
Appendix E - Supplementary material of Chapter 4 and 5	170
Appendix F - Supplementary material of Chapter 4 and 5	172
Appendix G - Supplementary material of Chapter 5	173
Appendix H - Supplementary material of Chapter 5	175
Appendix I - Royal Society of Chemistry License for Chapter 2	176
Curriculum Vitae	180

List of Tables

Table 2.1 Suspended Catalyst Compared with an Immobilized Catalyst.....	17
Table 2.2 Comparison between Hard and Soft-Templating	38
Table 2.3 Quantum Parameters Definitions	40
Table 3.1 Textural Properties of the Synthesized Mesoporous TiO ₂ with Pluronic P123 and Pluronic F127 added.	75
Table 4.1 Crystallite sizes of mesoporous TiO ₂ , Pt-TiO ₂ with different Pt loadings	100
Table 4.2 Specific surface area, pore volume and pore diameter for different photocatalyst materials. Also, metal dispersion for mesoporous TiO ₂ materials is reported.....	102
Table 4.3 Optical band gap of materials calcined at 500°C, calculated with the Kubelka-Munk (K-M) function and Tauc plot method.....	111
Table 4.4 Optical band gap of materials calcined at 550°C, calculated with the Kubelka-Munk (K-M) function and Tauc plot method.....	111
Table 4.5 Quantum yields for mesoporous platinum modified TiO ₂ , showing the effect of different loadings of Pt with a pH = 4.00 ± 0.05 in the Photo-CREC Water-II reactor.	115
Table 5.1 Absorbed photon fluxes for the various photocatalysts of the present study. P _i represents the incident radiation whereas P _t is the transmitted radiation and P _a is the absorbed radiation.	128
Table 5.2 Specific surface areas for the prepared photocatalysts.	130
Table 5.3 Relative composition of rutile and anatase in the prepared photocatalysts as assessed using the 25° Bragg angle and the 27° Bragg angle bands in the 2θ scale.	136
Table 5.4 Proposed oxidation reactions over TiO ₂ sites.	144
Table 5.5 Proposed reduction reactions on Pt sites.....	144

List of Figures

Figure 2.1 Raw Materials and Processes for Production of Hydrogen	7
Figure 2.2 Figure 2.2 Types of Photocatalytic Reactions	12
Figure 2.3 Schematic Description of the Hydrogen Production via Water Dissociation Mechanism in a Semiconductor. Dashed line represents the path that electron would follow in the event of undesirable recombination.	13
Figure 2.4 Diagram of Photo-Electrochemical Cell for Water Dissociation.	15
Figure 2.5 Suspended Photocatalyst Particles in a Water Dissociation Slurry System.	16
Figure 2.6 Energy Potential Diagram for Water Dissociation Using a Semiconductor Material.	19
Figure 2.7 Reaction Scheme of Hydrogen Production with the Presence of a Sacrificial Agent (methanol).	20
Figure 2.8 Energy Band Gaps for Different Semiconductors with respect to their Potentials (NHE) for Water Oxidation and Reduction	21
Figure 2.9 Unitary Cells of (a) Anatase, (b) Rutile and (c) Brookite.	23
Figure 2.10 Photocatalyst TiO ₂ with Pt as Co-Catalyst and organic scavenger.	24
Figure 2.11 Electron Injection in a Semiconductor Composite such as Anatase-Rutile (a)-(b) Type.	26
Figure 2.12 Band Diagram of a Solid Solution of Three Semiconductors.	27
Figure 2.13 Energy Diagram of a Semiconductor Doped with a Cation.	28
Figure 2.14 Schematic Representation of a Porous Solid, Showing the Most Common Types of Pores:	28

Figure 2.15 Representation of the Six Main Types of Isotherms: I, microporous solids; II, non-porous solids; III, macroporous solids; IV and V, mesoporous solids; VI, non-porous solids with a uniform surface.	30
Figure 2.16 Schematic Representation of (A) Soft-Templating and (B) Hard-Templating. ..	33
Figure 2.17 Schematic Description of the Formation of Mesoporous Structures: Cooperative Self-Assembly Process, and Liquid–Crystal Templating Process.	35
Figure 2.18 Schematic Description of Most Representative Steps of Evaporation Induced Self-Assembly (EISA).	36
Figure 2.19 Structure of Pluronic P123.	39
Figure 2.20 Structure of Pluronic F127.	39
Figure 3.1 N ₂ Adsorption-Desorption Isotherms for the Synthesized Mesoporous TiO ₂ Using Pluronic P123, Calcined at 500 °C, 600 °C and 700 °C.	71
Figure 3.2 N ₂ Adsorption-Desorption Isotherms for the Synthesized Mesoporous TiO ₂ Using Pluronic P123 and Doped with 1.00 % wt. Pt, calcined at 500 °C, 600 °C and 700 °C.	71
Figure 3.3 N ₂ Adsorption-Desorption Isotherms for the Synthesized Mesoporous TiO ₂ Using Pluronic P123 and Doped with 2.50 % wt. Pt, Calcined at 500 °C, 600 °C and 700 °C.	72
Figure 3.4 N ₂ Adsorption-Desorption Isotherms for the Synthesized Mesoporous TiO ₂ Using Pluronic P123 and Doped with 5.00 % wt. Pt, calcined at 500 °C, 600 °C and 700 °C.	72
Figure 3.5 N ₂ Adsorption-Desorption Isotherms for the Synthesized Mesoporous TiO ₂ Using Pluronic F127, Calcined at 500 °C, 600 °C and 700 °C.	73
Figure 3.6 N ₂ Adsorption-Desorption Isotherms for the Synthesized Mesoporous TiO ₂ Using Pluronic F127 and Doped with 1.00 % wt. Pt, calcined at 500 °C, 600 °C and 700 °C.	73
Figure 3.7 N ₂ Adsorption-Desorption Isotherms for the Synthesized Mesoporous TiO ₂ Using Pluronic F127 and Doped with 2.50 % wt. Pt, calcined at 500 °C, 600 °C and 700 °C.	74

Figure 3.8 N ₂ Adsorption-Desorption Isotherms for the Synthesized Mesoporous TiO ₂ Using Pluronic F127 and Doped with 5.00 % wt. Platinum Loading, Calcined at 500 °C, 600 °C and 700 °C.....	74
Figure 3.9 XRD Diffractograms of the Synthesized Mesoporous TiO ₂ Using Pluronic P123, Calcined at 500 °C, 600 °C and 700 °C.....	77
Figure 3.10 XRD Diffractograms of the Synthesized Mesoporous TiO ₂ Using Pluronic P123 with 1.00 % wt Pt, Calcined at 500 °C, 600 °C and 700 °C.....	77
Figure 3.11 XRD Diffractograms of the Synthesized Mesoporous TiO ₂ Using Pluronic P123, with 2.50 % wt. Pt, calcined at 500 °C, 600 °C and 700 °C.....	78
Figure 3.12 XRD Diffractograms of the Synthesized Mesoporous TiO ₂ Using Pluronic P123, with 5.00 % wt. Pt, calcined at 500 °C, 600 °C and 700 °C.....	78
Figure 3.13 XRD Diffractograms of the Synthesized Mesoporous TiO ₂ Using Pluronic F127, Calcined at 500 °C, 600 °C and 700 °C.....	79
Figure 3.14 XRD Diffractograms of the Synthesized Mesoporous TiO ₂ Using Pluronic F127 and Doped with 1.00 % wt Pt, calcined at 500 °C, 600 °C and 700 °C.	80
Figure 3.15 XRD Diffractograms of the Synthesized Mesoporous TiO ₂ Using Pluronic F127 and Doped with 2.50 % wt Pt, calcined at 500 °C, 600 °C and 700 °C.	80
Figure 3.16 XRD Diffractograms of the Synthesized Mesoporous TiO ₂ using Pluronic F127 and Doped with 5.00 % wt Pt, calcined at 500 °C, 600 °C and 700 °C.	81
Figure 3.17 SEM Images of Mesoporous TiO ₂ Photocatalysts Prepared Using Pluronic P123 at a 500°C Calcination Temperature.	82
Figure 3.18 SEM Images of Mesoporous Pt–TiO ₂ Photocatalysts Prepared Using Pluronic P123 with 1.00 % wt. Pt at a 500°C Calcination Temperature.	82
Figure 3.19 SEM Images of Mesoporous Pt–TiO ₂ Photocatalysts Prepared Using Pluronic P123 with 2.50 % wt. Pt at a 500°C Calcination Temperature.	83

Figure 3.20 SEM Images of Mesoporous Pt–TiO ₂ Photocatalysts Prepared Using Pluronic F127 at a 500°C Calcination Temperature.....	83
Figure 3.21 SEM Images of Mesoporous Pt–TiO ₂ Photocatalysts Prepared Using Pluronic F127 with 1.00 % wt. Pt at a 500°C Calcination Temperature.	84
Figure 3.22 SEM Images of Mesoporous Pt–TiO ₂ Photocatalysts Prepared Using Pluronic F127 with 2.50 % wt. Platinum Loading at a 500°C Calcination Temperature.	84
Figure 3.23 Changes of Cumulative Hydrogen Produced at Various Irradiation Times with Different Photocatalyst Loadings. Notes: a) Mesoporous TiO ₂ synthesized using Pluronic P123 and calcined at 500 °C, b) Photocatalyst irradiated with a near-UV light of $\lambda=368$ nm, c) pH = 4.00 \pm 0.05, d) 2.00 % v/v ethanol scavenger. Standard deviation for repeats are \pm 6 %	86
Figure 3.24 Changes of Cumulative Hydrogen Produced at Various Irradiation Times and with Different Photocatalyst Loadings. Notes: a) Mesoporous TiO ₂ synthesized using Pluronic P123, doped with 1.00 wt% Pt and calcined at 500 °C, b) Photocatalyst irradiated with a UV light of $\lambda=368$ nm, c) pH = 4.00 \pm 0.05, d) 2.00 % v/v ethanol scavenger. Standard deviation for repeats \pm 6 %	87
Figure 3.25 . Changes of Cumulative Hydrogen Produced at Various Irradiation Times with Different Photocatalyst Loadings. Note: a) Mesoporous TiO ₂ synthesized using Pluronic P123, doped with 2.50 wt% Pt and calcined at 500 °C, b) Photocatalyst irradiated with a UV light of $\lambda=368$ nm, c) pH = 4.00 \pm 0.05 and d) 2.00 % v/v ethanol scavenger. Standard deviation for repeats \pm 6 %	88
Figure 3.26 Changes of Cumulative Hydrogen Produced at Various Irradiation Times with Different Photocatalyst Loadings. Notes: a) Mesoporous TiO ₂ synthesized using Pluronic F127, calcined at 500 °C b) Photocatalyst irradiated with a UV light of $\lambda=368$ nm, c) pH = 4.00 \pm 0.05, d) 2.00 % v/v ethanol scavenger. Standard deviation for repeats \pm 7 %	89
Figure 3.27 Changes of Cumulative Hydrogen Produced at Various Irradiation Times and with Different Photocatalyst Loadings. Notes: a) Mesoporous TiO ₂ synthesized using Pluronic F127, doped with 1.00 wt. % and calcined at 500 °C b) Photocatalyst irradiated with a UV light	

of $\lambda=368$ nm) pH = 4.00 ± 0.05 and d) 2.00 % v/v ethanol scavenger. Standard deviation for repeats ± 7 %	90
Figure 3.28 Changes of Cumulative Hydrogen Produced at Various Irradiation Times and with Different Photocatalyst Loadings. Notes: a) Mesoporous TiO ₂ synthesized using Pluronic F127, doped with 2.50 wt% Pt and calcined at 500°C, b) Photocatalyst irradiated with a UV light of $\lambda=368$ nm, c) pH = 4.00 ± 0.05 , d) 2.00 % v/v ethanol scavenger. Standard deviation for repeats ± 7 %	91
Figure 4.1 Schematic diagram of the Photo-CREC-Water-II photoreactor with a H ₂ mixing tank: (1) BLB lamp, (2) Pyrex glass tube, (3) UV-opaque polyethylene cylinder, (4) fused-silica windows, (5) centrifugal pump, (6) H ₂ storing/mixing tank, (7) gas sampling port, (8) purging gas injector and (9) draining gas valve.....	98
Figure 4.2 XRD diffractograms of the photoactive materials for hydrogen production. XRD diffractograms were overlapped for comparison. (Δ) represents TiO ₂ in the anatase phase and (R) indicates TiO ₂ in the rutile phase.....	99
Figure 4.3 N ₂ adsorption-desorption isotherm of mesoporous TiO ₂ semiconductor calcined at 550 °C.....	101
Figure 4.4 N ₂ adsorption-desorption isotherm of 1.00 wt. %-Pt / Degussa P25 heated at 450 °C.....	102
Figure 4.5 Barrett-Joyner-Halenda (BJH) pore size distribution plot of mesoporous TiO ₂ calcined at 550 °C.	103
Figure 4.6 Barrett-Joyner-Halenda (BJH) pore size distribution plot of 1.00 wt. %-Pt-TiO ₂ Degussa P25 semiconductor heated at 450 °C.....	104
Figure 4.7 X-ray photoelectron spectroscopy (XPS) of 1.00 wt. % Pt-mesoTiO ₂ -550 °C...	105
Figure 4.8 UV-vis absorption spectra of the different semiconductor materials calcined at 500°C: a) Degussa P25, b) 1.00 wt. % Pt / Degussa P25-450°C, c) Meso-TiO ₂ , d) 0.25 wt. % Pt- Meso-TiO ₂ , e) 0.75 wt. % Pt- Meso-TiO ₂ , f) 1.00 wt. % Pt- Meso-TiO ₂ and g) 2.50 wt. % Pt- Meso-TiO ₂	106

Figure 4.9 UV-vis absorption spectra of the different semiconductor materials calcined at 550°C: a) Degussa P25, b) 1.00 wt. % Pt / Degussa P25-450°C, c) Meso-TiO ₂ , d) 0.25 wt. % Pt- Meso-TiO ₂ , e) 0.75 wt. % Pt-Meso-TiO ₂ f) 1.00 wt. % Pt-Meso-TiO ₂ and g) 2.50 wt. % Pt-Meso-TiO ₂	107
Figure 4.10 Optical band gap calculation for Degussa P25 (DP25) using the Tauc plot method. This plot was established using the UV-vis absorption spectra.....	108
Figure 4.11 Optical band gap calculation for Meso-TiO ₂ -550°C using the Tauc plot. This plot was established using the UV-vis absorption spectra.	109
Figure 4.12 Optical band gap determination for a 2.50 wt. % Pt-Meso-TiO ₂ -550°C using the Tauc Plot. This plot was established on the basis of the UV-vis absorption spectra.....	109
Figure 4.13 Effect of platinum loading on the optical band gap of semiconducting materials calcined at 500 °C.	110
Figure 4.14 Effect of platinum loading on the optical band gap of semiconducting materials calcined at 550 °C.	110
Figure 4.15 SEM images of mesoporous Pt–TiO ₂ photocatalysts prepared with different platinum loading at 550°C calcination temperature. (a) 1.00 wt. % Pt-TiO ₂ –Mesoporous; (b) 2.50 wt% Pt-TiO ₂ –Mesoporous; (c) 5.00 wt. % Pt-TiO ₂ –Mesoporous.....	112
Figure 4.16 Hydrogen evolution for different semiconductor materials at pH = 4.00 ± 0.05 and 2 % v/v ethanol. Photocatalyst loading 1.00 g/l. Standard deviation for repeats ± 5 %.....	113
Figure 5.1 Schematic diagram of a TiO ₂ photocatalyst with added Pt. Pt sites are shown inside and outside semiconductor particles. Inner sites are dominant electron reservoirs enhancing hydrogen production.	124
Figure 5.2 Schematic diagrams of the Photo-CREC Water II Reactor with a H ₂ mixing/storage tank:.....	127
Figure 5.3 Adsorption–desorption isotherms for Pt-TiO ₂ . Pt was added by wet impregnation.	129

Figure 5.4 Adsorption–desorption of N ₂ on TiO ₂ with 1.70 wt. % Pt prepared via the sol-gel A method.....	130
Figure 5.5 Pore size distribution of the Pt–TiO ₂ prepared via incipient wetness impregnation; (●) mesoporous TiO ₂ thermally treated at 550 °C (sol-gel B), (■) mesoporous TiO ₂ calcined at 450 °C (sol-gel A), (Δ) Degussa P25 impregnated with 1.00 wt. % Pt and calcined at 450 °C.	131
Figure 5.6 Tauc Plots for sol-gel A based TiO ₂ photocatalysts calcined at 450 °C: (A) TiO ₂ sol-gel A; (B) TiO ₂ sol-gel A with 0.42 wt. % Pt; (C) TiO ₂ sol-gel A with 0.82 wt. % Pt; (D) TiO ₂ sol-gel A with 1.70 wt. % Pt.	132
Figure 5.7 Influence of platinum loading on the band gap of the photocatalysts: (●) TiO ₂ —Mesoporous, thermally treated at 550 °C (sol-gel B) [8], (■) TiO ₂ —Mesoporous, calcined 450 °C (sol-gel A), (Δ) Degussa P25 impregnated and calcined at 450 °C.....	133
Figure 5.8 X-ray diffractogram for: (A) TiO ₂ , Degussa P25; (B) wet impregnated with 1.70 wt. % Pt on TiO ₂ Degussa P25; (C) incipiently impregnated with 1.00 wt. % Pt on TiO ₂ Degussa P25.	135
Figure 5.9 Cumulative hydrogen formation under an argon atmosphere for various photocatalysts: (◆,◇) Pt–TiO ₂ prepared via incipient wetness impregnation with 1.70 wt. % and 0.82 wt. % of Pt loadings on TiO ₂ Degussa P25, (Δ) Degussa P25 and (+) Blank run [no photocatalyst]. Photoreaction conditions: pH = 4.00 ± 0.05, 2.00% v/v ethanol, photocatalyst loading: 0.15 g/L. Standard deviation for repeats was ±4.5%.	137
Figure 5.10 Cumulative hydrogen formation under an argon atmosphere for various photocatalysts using: (■) Pt–TiO ₂ prepared via sol-gel A with 1.70 wt. % of Pt loadings, (□) TiO ₂ prepared via sol-gel A and (Δ) Degussa P25, (+) Blank run [no photo catalyst loaded]. Photoreaction conditions: pH = 4.00 ± 0.05, 2.00% v/v ethanol, photocatalyst loading: 0.15 g/L. Standard deviation for repeats was ±5%.	138
Figure 5.11 Cumulative hydrogen formation under an argon atmosphere for various photocatalysts using: (●) (○) Pt–TiO ₂ prepared via sol-gel B with 2.50 wt. % and 1.00 wt. % Pt, (Δ) Degussa P25, (+) Blank run [no photocatalyst]. Photoreaction conditions: pH = 4.00	

± 0.05, 2.00% v/v ethanol, photocatalyst loading: 0.15 g/L. Standard deviation for repeats was ±5%.....	139
Figure 5.12 Oxidation–reduction network promoted by TiO ₂ and Pt sites in the Pt–TiO ₂ photocatalysts.....	141
Figure 5.13 Methane increase with irradiation time for: (●) 2.50 wt. % Pt–TiO ₂ (sol-gel B), (■) 1.70 wt. % Pt–TiO ₂ (sol-gel A), (◆) 1.70 wt. % Pt–TiO ₂ (wetness impregnation) and (Δ) Degussa P25. Standard deviation for repeats is within ±7.5%.....	142
Figure 5.14 Ethane increase with irradiation time for: (●) 2.50 wt. % Pt–TiO ₂ (sol-gel B), (■) 1.70 wt. % Pt–TiO ₂ (sol-gel A), (◆) 1.70 wt. % Pt–TiO ₂ (wetness impregnation) and (Δ) Degussa P25. Standard deviation for repeats is within ±7%.....	143
Figure 5.15 Acetaldehyde increase with irradiation time: (●) 2.50 wt. % Pt–TiO ₂ (sol-gel B), (■) 1.70 wt. % Pt–TiO ₂ (sol-gel A), (◆) 1.70 wt. % Pt–TiO ₂ (wetness impregnation) and (Δ) Degussa P25. Standard deviation for repeats was within ±6.5%.....	145
Figure 5.16 CO ₂ increase with irradiation time for: (●) 2.50 wt. % Pt–TiO ₂ (sol-gel B), (■) 1.70 wt. % Pt–TiO ₂ (sol-gel A), (◆) 1.70 wt. % Pt–TiO ₂ (wetness impregnation) and (Δ) Degussa P25. Standard deviation for repeats is within ±7.5%.....	146
Figure 5.17 Ethanol concentration changes with irradiation time for: (●) 2.50 wt % Pt–TiO ₂ (sol-gel B), (■) 1.70 wt. % Pt–TiO ₂ (sol-gel A), (◆) 1.70 wt. % Pt–TiO ₂ (wetness impregnation) and (Δ) Degussa P25. Notes: a) Initial ethanol concentration: 2.00% v/v or 0.345 mole/L.	147
Figure 5.18 Quantum yields at various irradiation times for: (●) 2.50 wt. % Pt–TiO ₂ (sol-gel B), (■) 1.70 wt. % Pt–TiO ₂ (sol-gel A), (◆) 1.70 wt. % Pt–TiO ₂ (wetness impregnation) and (Δ) Degussa P25. Note: TiO ₂ (Degussa P25) is reported as a reference.....	148
Figure A.0.1 Changes of Cumulative Hydrogen Produced at Various Irradiation Times with Different Photocatalyst Loadings. Notes: a) Mesoporous TiO ₂ synthesized using Pluronic P123 and calcined at 600 °C, b) Photocatalyst irradiated with a near-UV light of λ=368 nm, c) pH = 4.00 ± 0.05, d) 2.00 % v/v ethanol scavenger. Standard deviation for repeats are ± 5.5 %.....	155

Figure A.0.2 Changes of Cumulative Hydrogen Produced at Various Irradiation Times and with Different Photocatalyst Loadings. Notes: a) Mesoporous TiO₂ synthesized using Pluronic P123, doped with 1.00 wt% Pt and calcined at 600 °C, b) Photocatalyst irradiated with a UV light of $\lambda=368$ nm, c) pH = 4.00 ± 0.05 , d) 2.00 % v/v ethanol scavenger. Standard deviation for repeats ± 5.5 %..... 156

Figure A.0.3 . Changes of Cumulative Hydrogen Produced at Various Irradiation Times with Different Photocatalyst Loadings. Note: a) Mesoporous TiO₂ synthesized using Pluronic P123, doped with 2.50 wt% Pt and calcined at 600 °C, b) Photocatalyst irradiated with a UV light of $\lambda=368$ nm, c) pH = 4.00 ± 0.05 and d) 2.00 % v/v ethanol scavenger. Standard deviation for repeats ± 5.5 %..... 156

Figure A.0.4 Changes of Cumulative Hydrogen Produced at Various Irradiation Times with Different Photocatalyst Loadings. Notes: a) Mesoporous TiO₂ synthesized using Pluronic F127, calcined at 600 °C b) Photocatalyst irradiated with a UV light of $\lambda=368$ nm, c) pH = 4.00 ± 0.05, d) 2.00 % v/v ethanol scavenger . Standard deviation for repeats ± 4.5 % 157

Figure A.0.5 Changes of Cumulative Hydrogen Produced at Various Irradiation Times and with Different Photocatalyst Loadings. Notes: a) Mesoporous TiO₂ synthesized using Pluronic F127, doped with 1.00 wt% and calcined at 600 °C b) Photocatalyst irradiated with a UV light of $\lambda=368$ nm) pH = 4.00 ± 0.05 and d) 2.00 % v/v ethanol scavenger . Standard deviation for repeats ± 4.5 %..... 158

Figure A.0.6 Changes of Cumulative Hydrogen Produced at Various Irradiation Times and with Different Photocatalyst Loadings. Notes: a) Mesoporous TiO₂ synthesized using Pluronic F127, doped with 2.50 wt% Pt and calcined at 500°C, b) Photocatalyst irradiated with a UV light of $\lambda=368$ nm, c) pH = 4.00 ± 0.05, d) 2.00 % v/v ethanol scavenger . Standard deviation for repeats ± 4.5 % 159

Figure A.0.7 Changes of Cumulative Hydrogen Produced at Various Irradiation Times with Different Photocatalyst Loadings. Notes: a) Mesoporous TiO₂ synthesized using Pluronic P123 and calcined at 700 °C, b) Photocatalyst irradiated with a near-UV light of $\lambda=368$ nm, c) pH = 4.00 ± 0.05, d) 2.00 % v/v ethanol scavenger . Standard deviation for repeats are ± 7.5 % 160

Figure A.0.8 Changes of Cumulative Hydrogen Produced at Various Irradiation Times and with Different Photocatalyst Loadings. Notes: a) Mesoporous TiO₂ synthesized using Pluronic P123, doped with 1.00 wt% Pt and calcined at 700 °C, b) Photocatalyst irradiated with a UV light of $\lambda=368$ nm, c) pH = 4.00 \pm 0.05 , d) 2.00 % v/v ethanol scavenger. Standard deviation for repeats \pm 7.5 %..... 161

Figure A.0.9 . Changes of Cumulative Hydrogen Produced at Various Irradiation Times with Different Photocatalyst Loadings. Note: a) Mesoporous TiO₂ synthesized using Pluronic P123, doped with 2.50 wt% Pt and calcined at 700 °C, b) Photocatalyst irradiated with a UV light of $\lambda=368$ nm, c) pH = 4.00 \pm 0.05 and d) 2.00 % v/v ethanol scavenger. Standard deviation for repeats \pm 7.5 %..... 162

Figure A.0.10 Changes of Cumulative Hydrogen Produced at Various Irradiation Times with Different Photocatalyst Loadings. Notes: a) Mesoporous TiO₂ synthesized using Pluronic F127 , calcined at 700 °C b) Photocatalyst irradiated with a UV light of $\lambda=368$ nm, c) pH = 4.00 \pm 0.05, d) 2.00 % v/v ethanol scavenger . Standard deviation for repeats \pm 6.5 % 163

Figure A.0.11 Changes of Cumulative Hydrogen Produced at Various Irradiation Times and with Different Photocatalyst Loadings. Notes: a) Mesoporous TiO₂ synthesized using Pluronic F127, doped with 1.00 wt% and calcined at 700 °C b) Photocatalyst irradiated with a UV light of $\lambda=368$ nm) pH = 4.00 \pm 0.05 and d) 2.00 % v/v ethanol scavenger . Standard deviation for repeats \pm 6.5 %..... 163

Figure A.0.12 Changes of Cumulative Hydrogen Produced At Various Irradiation Times and with Different Photocatalyst Loadings. Notes: a) Mesoporous TiO₂ synthesized using Pluronic F127, doped with 2.50 wt% Pt and calcined at 500°C, b) Photocatalyst irradiated with a UV light of $\lambda=368$ nm, c) pH = 4.00 \pm 0.05, d) 2.00 % v/v ethanol scavenger . Standard deviation for repeats \pm 6.5 %..... 164

Nomenclature

c speed of light (3.0×10^8 m/s)

C Celsius

d_p porous diameter (cm)

e^- electron

h^+ hole

h Planck's constant (6.63×10^{-34} J/s)

E energy of a photon at a given wavelength (J)

E_{av} average energy of a photon at a wavelength range, (J/mol photon).

E_{bg} energy band gap (eV)

eV electron volts

H_2PtCl_6 hexachloroplatinic acid

H^\bullet hydrogen radical

P_a rate of absorbed photons by semiconductor (photons/s)

P_{bs} rate of backscattered photons flying off the system (photons/s)

P_i rate of photons reaching the reactor inner surface (photons/s)

P_t rate of transmitted photons (photons/s)

P_t platinum

OH^- hydroxide ions

$\bullet OH$ hydroxyl radical

t time (h)

TiO₂ titanium dioxide

V_g volume of the gas phase in the storage tank (cm³)

W weight (g)

wt. % weight percent (% m/m)

Greek symbols

α absorbance (a.u.)

θ diffraction angle (°)

λ wavelength (nm)

ν frequency (1/s)

Acronyms

BJH Barrett–Joyner–Halenda model

BLB black light blue lamp

BET Brunauer–Emmett–Teller surface area method

CB conduction band

DP25 TiO₂ Degussa P25

PCWII Photo CREC Water II Reactor

QY quantum yield

UV ultraviolet

VB balance band

Subscripts

a	absorbed photons by the photocatalyst
b_g	band gap
b_s	photons backscattered by the photocatalyst
g	gas phase
i	incident photons to the photocatalyst
t	photons transmitted by the photocatalyst
max	maximum
min	minimum

Chapter 1

1. Introduction

Currently, fossil energy resources are being used extensively to meet most of the world's energy requirements. The projections of energy availability and use suggest that in the near future, there will be major issues and challenges to be faced with energy supply and demand. Additionally, the combustion of fossil fuels leads to atmospheric emissions of carbon particles, CO₂ as well as noxious gases such as NO_x, SO_x. Thus, environmentally friendly fuels, that are both cost-effective and easily storable, are of great importance for the world's sustainable development [1].

Hydrogen is an ideal candidate as an energy vector [2]. Several technologies can be used to generate hydrogen. However, only a few of them can be considered as truly environmentally friendly. Steam hydrocarbon reforming is the current dominant technology for hydrogen production. It requires high temperatures (700–1100 °C) and emits large amounts of CO₂ [3]. Hence, efforts focused on water splitting are of great potential significance. Water splitting using solar energy is one of the most attractive approaches to produce hydrogen. Water splitting is an eco-friendly process that can be operated at ambient temperature and pressure. This process can take advantage of sunlight; an abundant and inexpensive renewable energy source [4,5,6]. This technology has the potential of being of benefit to isolated communities in Canada. Hydrogen could be used as an energy vector. Moreover, it could be used as chemical energy in Winter from the solar energy collected during the Summer.

Alternatively, one could envision the use of current excess of electrical energy in Ontario and Quebec [7-8], in photocatalytic technology for hydrogen production. The hydrogen produced could be used in individual vehicles power-driven by fuel cells. As well, it could be co-fed with other hydrocarbon feedstocks (i.e. methane) as a fuel, in power stations, thus reducing CO₂ emissions [9].

Since the discovery of photocatalytic reactions in 1972 by Honda and Fujishima [10], numerous researchers have work aiming to identify the optimal conditions for degradation of pollutants in water and air, as well as for hydrogen generation. This process takes into account the water splitting as alternative to the energy concerns experienced currently.

In photocatalytic water splitting, photons are absorbed by semiconductors, and as a result, water splits into hydrogen and oxygen as shown in Figure 1.1. Nevertheless, water splitting is not thermodynamically favoured. As well, there are restrictions related to band gap excitation and the recombination of charge carriers in semiconductor photocatalysts. This leads to low hydrogen production which up to date has limited the practical application of this technology on a large scale. As a result, current research focuses on thermodynamic limitations as well as increasing the efficiency and stability of the materials [11,12]. All this is essential to achieve process scale up and process commercialization [13,14].

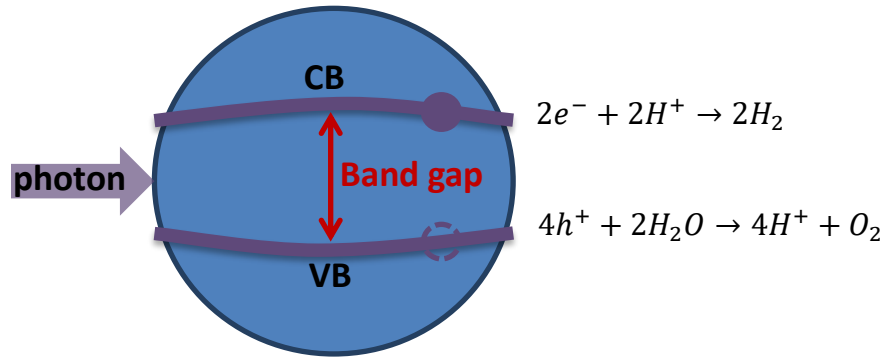


Figure 1.1 Schematic representation of the mechanism of the photocatalytic water splitting over a semiconductor particle

Semiconductors are characterized by two types of mobile carriers: a) electrons in the conduction band and b) holes in the valence band. Both bands are separated by an energy gap. There is a continuous transition of electrons between the bands. When a valence electron is supplied with an energy equal or greater to the energy band gap it is transferred to the conduction band. This leads to the formation of an electron-hole pair. When an electron falls from the conduction band into the valence band, and into a semiconductor hole, a hole-electron pair recombination occurs.

Among the various semiconductors, TiO₂ has been extensively studied due to its photosensitivity, low cost, low toxicity, and good chemical and thermal stability. There are two main issues with TiO₂. On one hand, TiO₂ can be only be activated with near-ultraviolet irradiation (near-UV) due to its wide band gap (3.20 eV for anatase and 3.00 eV for rutile). This limits its application with solar energy, as near-UV light constitutes only 4-5% of sunlight. On the other hand, electron hole recombination reduces the photoelectric conversion efficiency of TiO₂. All these factors, limit the practical application of TiO₂ as a viable semiconductor to be activated with solar light.

TiO₂ can be modified with CdS, ZnO, PbS, Cu₂O, Bi₂S₃, and CdSe, forming TiO₂ composites. Theoretically, combining n-type TiO₂ with p-type semiconductors is effective in improving the photoelectric TiO₂ conversion efficiency. Many of these modified materials have received less attention since, under irradiation and in contact with water, they can experience photocorrosion (*e.g.* Zn²⁺ or Cd²⁺ dissolution) [15]. A reliable alternative to improve photoelectric conversion is the addition of noble metals (*e.g.* Pt, Au, Ag and Pd) during the semiconductor synthesis. Noble metal addition favours water splitting, given that: a) the surface plasmon resonance of noble metal particles can be excited by near-UV and visible light, (b) the energy band gap is reduced, and c) the noble metal nanoparticles act as electron traps. Regarding possible noble metals as co-catalysts, Pt is a prime choice given its ability to trap photogenerated electrons. Interaction of trapped electrons and H⁺, yields H• radicals, and molecular hydrogen.

In recent years, it has been shown quite extensively that the successful development of semiconductors must be accompanied by a rigorous evaluation of photon utilization efficiencies. This approach has been demonstrated extensively in several research studies by CREC-UWO researchers with methodologies summarized in de Lasa et al [16,17]. It is in this context, that it is considered of major importance to extend these methodologies to the photocatalytic production of hydrogen with an evaluation of Quantum Yields.

1.1 General Objectives

The present study aims at advancing photocatalytic hydrogen generation via water dissociation by developing novel semiconductor mesoporous materials using a new synthesis method. It is envisioned that prepared semiconductors will be characterized in terms of structural and physicochemical properties as well as photocatalytic activity. It is anticipated that the high expected mesoporous TiO₂ photocatalytic activity will be further enhanced with highly dispersed noble metals, such as Pt. It is expected that the projected high photoactivity of the prepared photocatalysts will be ranked by evaluating the QYs in a CREC-Water II Reactor.

In this respect, the general objectives of this PhD dissertation can be divided into three main sub-objectives:

- a) The development and establishment of new preparation methods for photocatalytic materials based on mesoporous TiO₂ and using Pt as a co-catalyst. These new semiconductors shall be based on a modified architecture where particle size, particle size distribution, specific surface area, crystalline phases, composition and light absorption are closely controlled.
- b) The demonstration of the high performance of the developed semiconductors for water dissociation to hydrogen under near-UV irradiation and using an environmentally friendly scavenger. This demonstration shall involve a photocatalytic reactor unit where Quantum Yields can be rigorously evaluated.
- c) The elucidation of the oxidation-reduction reaction network for hydrogen production involving ethanol as a scavenger, with the aim of establishing adequate kinetic models suitable for photocatalytic reactor scale-up.

1.2 References

- [1] Mao, S.; Shen, S. & Guo, L. Nanomaterials for renewable hydrogen production, storage and utilization. *Progress in Natural Science: Materials International*. 2012, 22, 522-534.
- [2] Jing, D.; Guo, L.; Zhao, L.; Zhang, X.; Liu, H.; Li, M.; Shen, S.; Liu, G. & Hu, X. Efficient solar hydrogen production by photocatalytic water splitting: From fundamental study to pilot demonstration. *International Journal of Hydrogen Energy*. 2010, 35, 7087-7087.
- [3] Häussinger, P.; Lohmüller, R. & Watson, A. Hydrogen, 1. Properties and Occurrence. *Ullmann's Encyclopedia of Industrial Chemistry*. 2011.
- [4] Navarro, Y.; Rufino M.; Álvarez-Galván, M.C.; Del Valle, F.; Villoria De La Mano, J.A. & Fierro, J.L.G. Water Splitting on Semiconductor Catalysts under Visible-Light Irradiation. *ChemSusChem*. 2009, 2, 471–85.
- [5] Navarro, R.M.; Del Valle, F.; Villoria De La Mano, J.A.; Álvarez-Galván, M.C. & Fierro, J.L.G. Photocatalytic Water Splitting Under Visible Light: Concept and Catalysts Development. *Photocatalytic Technologies. Advances in Chemical Engineering*. 2009, 36, 111–43
- [6] Maeda, K.; Teramura, K.; Lu D.; Takata, T.; Inoue, S.; & Domen, K. Photocatalyst releasing hydrogen from water. *Nature*. 2006, 440, 295–295.
- [7] Taljan G., Canizares C., Fowler M., Verbic G. The Feasibility of Hydrogen Storage for Mixed Wind-Nuclear Power Plants, *Power Systems IEEE Transactions*. 2018, 23, 1507-1518.
- [8] Forsberg C. Future hydrogen markets for large-scale hydrogen production systems. *International Journal of Hydrogen Energy*, 2007, 32 (4), 431-439.

- [9] Prakash D., Meisen P. Hydrogen for Large-scale Electricity Generation in USA. Global Energy Network Institute. 2011.
- [10] Honda, K & Fujishima, A. Electrochemical Photolysis of Water at a Semiconductor Electrode. *Nature*. 1972, 238, 37–38.
- [11] Nakata, K. & Fujishima, A. TiO₂ photocatalysis: Design and applications. *Journal of Photochemistry and Photobiology C: Photochemistry Reviews*, 2012, 13, 169 –189.
- [12] Nowotny J.; Sorrell, C.C.; Sheppard, L.R. & Bak, T. Solar-hydrogen: Environmentally safe fuel for the future. *International Journal of Hydrogen Energy*, 2005, 30 ,521 – 544.
- [13] Honda, K & Fujishima, A. Electrochemical Evidence for the Mechanism of the Primary Stage of Photosynthesis. *Bulletin of the Chemical Society of Japan*. 1971, 44, 1148–1150.
- [14] U.S. Department of Energy. Hydrogen production. Fuel cells and infrastructure technologies program, 2009, 3,1-20.
- [15] Wang Y., Wang Q., Zhan X., Wang F., Safdar M. and He J. Visible light driven type II heterostructures and their enhanced photocatalysis properties: a review. *Nanoscale*, 2013, 5, 8326
- [16] Ibrahim, H.; de Lasa, H. Photo-catalytic degradation of air borne pollutants. Apparent quantum efficiencies in a novel photo-CREC-air reactor. *Chem. Eng. Sci.* 2003, 58, 943-949.
- [17] de Lasa, H.; Serrano, B.; Salices, M. *Photocatalytic Reaction Engineering*, First Ed., Springer: New York, 2005.

Chapter 2

2 Literature Review

Hydrogen can be produced through a wide variety of raw materials. These raw materials include fossil sources, such as gas and coal, as well as renewable sources, such as biomass and water, using renewable energy sources (sunlight, wind, hydraulic). A diversity of technologies can be used, including chemical, biological, electrolytic, photolytic and thermochemical processes.

Figure 2.1 describes some of the raw materials and technologies that can be used to produce hydrogen. Each technology is in a different state of development, and each offers unique opportunities, benefits and challenges. The availability of raw materials, the maturity of technology, political issues and costs are all factors that influence decision making about hydrogen production.

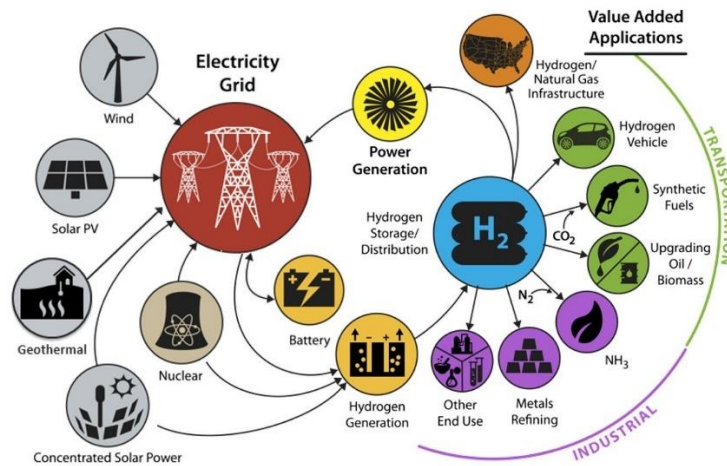


Figure 2.1 Raw Materials and Processes for Production of Hydrogen [1].

Some of these technologies are already available in the market for the industrial production of hydrogen. The first commercial technology, dating back to 1920s, is the water electrolysis to produce pure hydrogen. In the 1960s, industrial hydrogen production moved slowly to the use of fossil-based raw materials, which is the main source of hydrogen production today.

Main technologies to produce hydrogen from water dissociation are discussed in the next sections.

2.1 Hydrogen from the Dissociation of Water

Hydrogen can be generated from the dissociation of water through several processes. Some of these methods are electrolysis, photo electrolysis, photobiological production and the decomposition of water at high temperatures.

2.1.1 Water Electrolysis

Electrolysis is a process by which water is dissociated into hydrogen and oxygen through the application of electrical energy, as shown in Equation 2.1. The total energy that is needed for the electrolysis of water depends on the temperature. For example, at higher temperatures the electrical energy decreases. Therefore, a process of electrolysis at high temperatures is preferable when high temperatures are available as residual heat from another process [2,3].



Most of the electricity produced worldwide, is based on fossil energy sources. Currently, researchers are actively searching for some type of renewable source that could supply electricity to the electrolyzers, and be environmentally friendly.

2.1.2 Photobiological Production (bio-photolysis)

The photobiological production of hydrogen is based on two steps: photosynthesis and hydrogen production catalyzed by hydrogenase. For example, green algae and bacteria [2] could be used. The overall process involves the following two reactions:

Photosynthesis:



Hydrogen production:



2.1.3 Decomposition of Water at High Temperatures

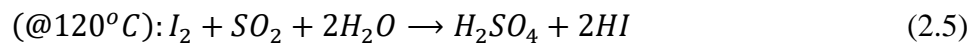
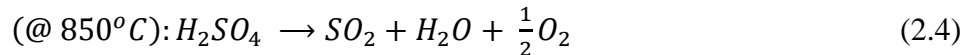
The dissociation of water at high temperatures is carried out at 300°C. At this temperature, 10% of the water is decomposed only, and the remaining 90% has to be recycled.

To reduce the process thermal load, other processes have been suggested for the dissociation of water at high temperatures (up to 850° C), such as: a) thermochemical cycles, b) hybrid systems coupling thermal decomposition and electrolytic decomposition, c) thermo-physical cycles as well as d) water decomposition by chemical plasma. In these kind of processes, efficiencies above 50% can be obtained, reducing the cost of hydrogen production.

The main technical challenge for these types of high temperature processes is the availability of materials that can resist corrosion at high temperatures, plus the development of membranes, heat exchangers, and heat storage media. Design and safety aspects are also very important [3].

2.1.4 Thermo-chemical Process

The dissociation of water by thermochemical processes leads to the conversion of water into hydrogen and oxygen. This approach involves a series of thermochemical reactions. An example of this type of process is the iodine/sulfur cycle, presented in equations (2.4-2.7):



For the implementation of thermochemical processes, research and development is still required to establish the approaches avoiding secondary reactions and eliminating the use

of harmful substances. Corrosion problems associated with the handling of such chemicals still require great attention [3,4].

2.1.5 Photolysis

Artificial photosynthesis is an alternative that involves capturing the energy available in the environment from sunlight, and converting it into a valuable and strategic fuel such as hydrogen. Artificial photocatalysis provides a way to mimic photosynthesis by using a semiconductor material to absorb and utilize solar energy by converting it into chemical species. As well, the dissociation of water using this type of process to produce hydrogen is promising, clean, low cost and environmentally friendly. In the following sections, important concepts for this work are presented [5-10].

2.2 Hydrogen Production via Photocatalysis

The interest in photocatalysis began in 1970, when this process was considered for the water dissociation to produce hydrogen using solar and UV energy. Then in 1980, a new potential application using water dissociation for environmental remediation was proposed [11]. Since then, interest applications of this technology that have been proposed for water purification, air purification, self-cleaning surfaces and the production of high energy content molecules, such as hydrogen, among others [12].

Photocatalysis belongs to the general field of catalysis. By using photocatalysis, many oxidation-reduction reactions with interesting applications can be obtained. These types of oxidation-reduction reactions may be used for water purification and air treatments. Photocatalysis can also be considered an advanced oxidation process, a technology which has been studied thoroughly in recent decades.

Photocatalysis is defined as "the acceleration of a photoreaction in the presence of a catalyst or its initiation under the action of light radiation (ultraviolet, visible or infrared) in the presence of a semiconductor substance that absorbs light continuously with interactions and regeneration of electrons / holes during the photochemical activation." (IUPAC). Photocatalytic reactions can be either homogeneous or heterogeneous. Heterogeneous

photocatalysis is by far the most studied in recent years, given its potential application for environmental and energy applications.

In homogeneous photocatalysis, reagents and photocatalysts are in the same phases. Photochemical degradations found using hydrogen peroxide ($\text{H}_2\text{O}_2/\text{UV}$), ozone (O_3/UV), transition metal oxides and photo-Fenton reagents (Fe^+ and $\text{Fe}^+/\text{H}_2\text{O}_2$) [13] belong to this group.

On the other hand, in heterogeneous photocatalysis, the photocatalyst is in a particulate solid phase while the various pollutants to be converted are in either the gas phase or liquid phase.

From classical heterogeneous catalysis, the overall process can be broken down into six independent steps:

- (a) Transfer of reagents from the fluid bulk to the catalyst surface.
- (b) The adsorption of at least one of the reagents.
- (c) The generation of electron / hole charge pair by absorbed photons.
- (d) The reaction in the adsorbed phase.
- (e) The desorption of the formed products.
- (f) The removal of products from the catalyst-fluid interface region.

Photocatalytic reactions occur in the adsorbed phase (step (c)). The only difference with conventional catalysis is the mode of activation of the catalyst in which thermal activation is replaced by photonic activation [14].

In heterogeneous photocatalysis, the reaction also involves interfaces between the solid photocatalyst (metal or semiconductor) and a fluid containing reactants and products. Processes involving irradiation of these adsorbate-metal interfaces are generally included in the branch of photochemistry. Therefore, the term "heterogeneous photocatalysis" is mainly used in cases where a semiconductor catalyst absorbs light, and is in contact with one gas phase or liquid phase.

Photocatalytic reactions can be classified into two categories: a) "uphill ($\Delta G^o > 0$) and b) downhill ($\Delta G^o < 0$) reactions", as shown in Figure 2.2.

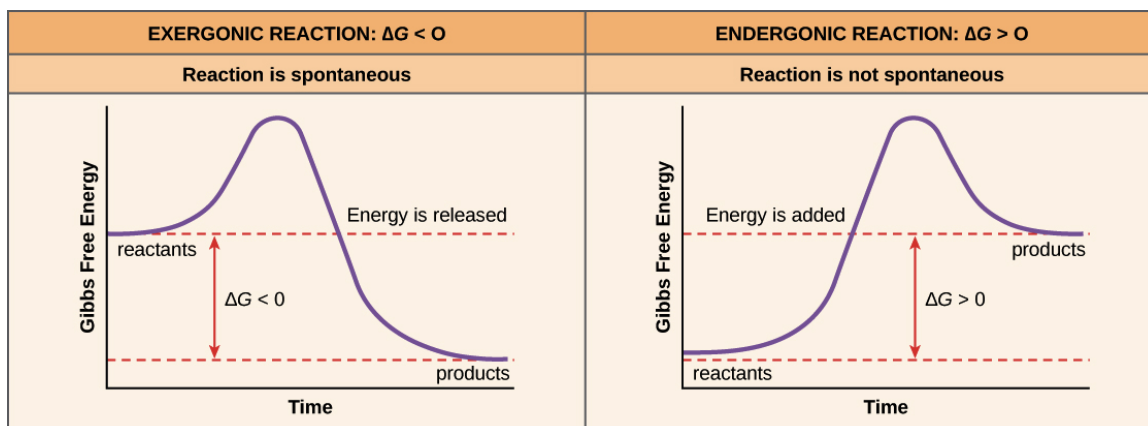


Figure 2.2 Figure 2.2 Types of Photocatalytic Reactions [15].

One should notice that the degradation of organic pollutants such as photooxidation of organic compounds using oxygen is generally a "downhill" ΔG reaction. Thus, the reaction may proceed irreversibly. This type of induced photo-reactions has been extensively studied using titanium dioxide.

On the other hand, water dissociation into H_2 and O_2 is accompanied by a large positive change in the Gibbs Free Energy ($\Delta G^o = 273$ kJ /mole). This is a reaction with an "uphill" ΔG . In this case, photon energy is converted into chemical energy, as it occurs in the photosynthesis by green plants. It is for this reason, that water dissociation, is frequently referred to as artificial photosynthesis [16].

The processes involved in the photocatalytic generation of H_2 are illustrated in Figure 2.3.

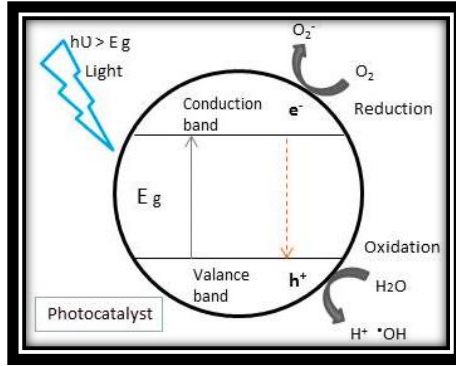


Figure 2.3 Schematic Description of the Hydrogen Production via Water Dissociation Mechanism in a Semiconductor. Dashed line represents the path that electron would follow in the event of undesirable recombination.

The semiconductor absorbs photons, with energy higher than its energy band gap (E_{bg}). This generates a pair of electron charge carriers and vacancies, in the conduction band and in the valence band respectively, as shown in Figure 2.3. After this initial step, the pair of charges separate and migrate towards the surface. On the photocatalyst surface, the charge carriers may reduce and oxidize adsorbed water molecules, producing hydrogen molecules [17]. Competing with this, there is the undesirable and potential charge carrier recombination, with energy being released as heat or photons [18].

Overall, the energy of the photons can be converted into chemical energy (hydrogen) via a combined oxidation and reduction process as follows:

Oxidation:



Reduction



Overall reaction



Hence, the redox potential for both reduction and oxidation processes determine the successful candidate semiconductor for water dissociation, with this being determined by the difference between valence and conduction bands energy levels.

Regarding the electronic structure of a potential photocatalyst for H₂ production, there are two important requirements: (i) The band gap should be $1.24 \text{ eV} < E_g < 3.26 \text{ eV}$, due to the targeted wavelengths $1000 \text{ nm} < \lambda < 380 \text{ nm}$. (ii) The band positions should be located such as the bottom of the conduction band is more negative than the redox potential of H⁺/H₂ (0 V versus NHE at pH=0) and the valence band more positive than the redox potential of the O₂/H₂O (1.23 V).

Thus, from a thermodynamic point of view, the water splitting reaction should be easily achieved using a photoinduced catalytic process involving materials which satisfy the above conditions. However, the overall photocatalytic water splitting reaction is an endothermic reaction. This means that, to overcome such an energy barrier, photons of higher energy are needed.

Within the great number of photoactive semiconductors proposed for water splitting and photo-reforming reactions, TiO₂ has until now been, the most promising. However, the reported photonic efficiencies from solar to hydrogen by TiO₂ photocatalytic water splitting are still low. This is mainly due to the following reasons:

- (a) The recombination of photo-generated electron/hole pairs: conduction band electrons can recombine with valence band holes very quickly and release energy in the form of unproductive heat or photons;
- (b) A competitive fast backward reaction: As mentioned before, water cleavage into hydrogen and oxygen is an energy unfavoured process. Thus, a backward reaction could easily proceed and strongly compete with water splitting;
- (c) The failure to absorb visible light photons: The band gap of TiO₂ is about 3.2 eV and only UV or near UV irradiation can be utilized for hydrogen production. Since the UV light only accounts for about 4% of the solar radiation energy, the efficiency of the process becomes necessarily low.

2.2.1 Photoreactor Configurations

Photocatalysis with water dissociation can be used for hydrogen production with two types of configurations: (i) photo-electrochemical cells and (ii) photocatalytic systems. The photo-electrochemical cells for the dissociation of water are described in Figure 2.4. They involve two electrodes immersed in an aqueous electrolyte, with one of them including an irradiated photocatalyst surface [19].

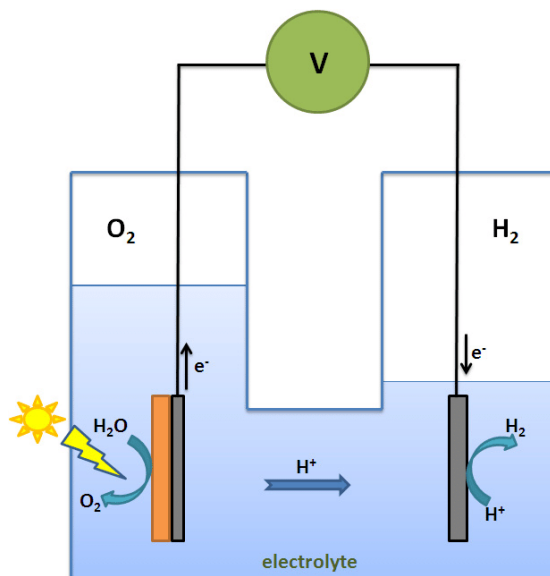


Figure 2.4 Diagram of Photo-Electrochemical Cell for Water Dissociation.

In photo-electrochemical cells, the photo-generated electron/hole pairs, product of the photon absorption by a photoanode, are separated by an external electric field. The holes migrate to the surface of the semiconductor where water molecules are oxidized to oxygen. On the other hand, the electrons are transported by an electric circuit to the counter electrode, reducing H^+ ions and forming hydrogen [20, 21]. Water dissociation using this cell was first reported by Fujishima and Honda in 1979, using TiO_2 as a photoanode and platinum as a cathode. The irradiation of the TiO_2 electrode with UV light allowed both H_2 and O_2 formation [23].

Photocatalytic systems use photocatalytic semiconductors. They can be designed with semiconductor particles in an aqueous suspension. In these slurry systems, each

photocatalyst particle act as a photo-electrochemical microcell, oxidizing and reducing the water on the particle surface as reported in Figure 2.5

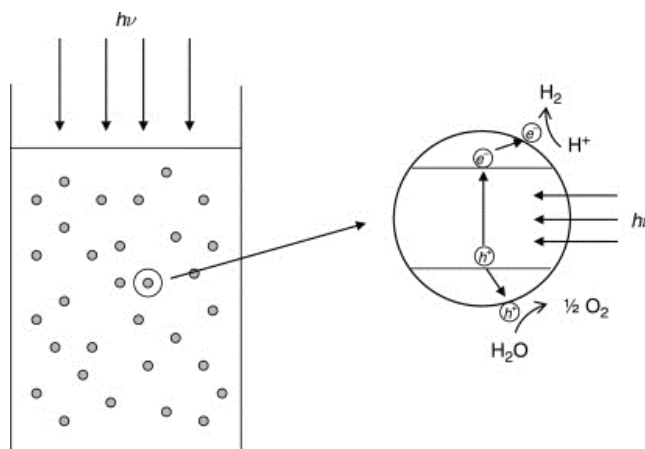


Figure 2.5 Suspended Photocatalyst Particles in a Water Dissociation Slurry System.

The photocatalytic particle suspended system has the advantage of being much simpler and less expensive than a photo-electrochemical cell. In addition, a variety of materials can be used as photocatalysts. Another extra advantage is that the particle slurries do not require high electrical conductivity as photoelectrodes do. An important additional benefit is that the irradiation absorption efficiency by the suspended catalysts can be much higher given the large exposed external particle specific surface areas.

However, photocatalytic particles in water slurry systems have the significant disadvantage of requiring separation of semiconductor materials from slurry.

It is worth mentioning that photocatalytic processes allow H_2 production under ambient conditions, using sunlight. This process is in fact, distinctively different from others such as thermo-reformed hydrocarbons or gasification. As a result of this, we consider this process of special interest for sites where the availability of large amounts of biomass and a high intensity of sunlight coincide.

Table 2.1 reports some of the differences that exist between a system with a suspended catalyst and a system with an immobilized catalyst [22,23].

Table 2.1 Suspended Catalyst Compared with an Immobilized Catalyst [24].

Suspended Photocatalyst	Immobilized Photocatalyst
<p>Advantages.</p> <p>It provides:</p> <ul style="list-style-type: none"> • Fast uniform distribution of the photocatalyst • High photocatalytic surface area per unit reactor volume. • High mass transfer between particles and water solution • Good mixing of suspended particles • Low pressure drops through the reactor 	<p>Advantages.</p> <p>It allows:</p> <ul style="list-style-type: none"> • Continuous operation • Improved removal of organic materials from water • No additional catalyst separation required.
<p>Disadvantages.</p> <p>It involves</p> <ul style="list-style-type: none"> • Expensive post-filtration, in order to recover photocatalytic material. • Significant light scattering and absorption in suspended particle medium 	<p>Disadvantages</p> <p>It involves</p> <ul style="list-style-type: none"> • Low irradiation efficiencies due to the light scattering on the immobilized catalyst • Deactivation of the immobilized photocatalyst deactivation due to particle surface detachment.

2.2.2 Photo-CREC Water Reactor II

The development and design of a hydrogen production systems based on heterogeneous photocatalysis is a research area of great importance. The configuration used to produce hydrogen in this study is based on the suspension system of the catalyst in water, using the Photo-CREC Water II Reactor.

Photo-CREC reactors were designed in early applications for the degradation of pollutants in water/air using UV radiation, having suspended or immobilized photocatalysts [25,26]. Currently, this type of reactors is being considered to produce hydrogen [27, 28].

Regarding the Photo-CREC Water II Reactor, it consists of two concentric tubes. A UV lamp is placed inside a second tube which is transparent. In this second tube, the photocatalytic suspension flows freely. This type of reactor works in a batch mode with high recirculation of water suspended particles. This unit is equipped with an airtight storage and feeding tank, which is always kept in agitation. This allows the photocatalyst to be well suspended and prevents the photocatalyst from settling. The hermetic tank of the unit is equipped with sampling ports for both liquid and gas phase sampling.

2.2.3 Required Energy

The production of H₂ through the dissociation of water is limited thermodynamically by the Gibbs free energy needed (237 kJ / mol, 1.23 eV). It is therefore necessary, as shown in Figure 2.6, that the semiconductor flat band potential exceeds the proton reduction potential (0.0 eV against the normal hydrogen electrode, NHE). In addition, and to facilitate the oxidation of water, the edge of the valence band must exceed the oxidation potential of the water (+1.23 eV against the NHE).

In agreement with this and in order to carry out water dissociation, the theoretical required energy gap necessary for a semiconductor is 1.23 eV [28].

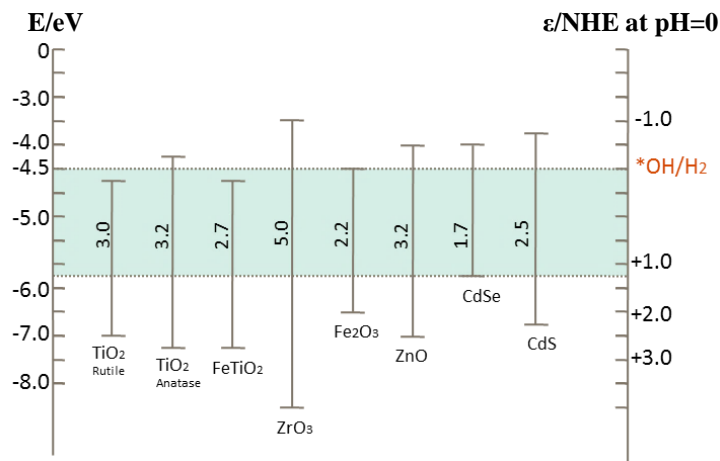


Figure 2.6 Energy Potential Diagram for Water Dissociation Using a Semiconductor Material.

Following the first reports on the dissociation of water on TiO_2 [29] several photocatalysts were considered [30,31]. In spite of the efficiency of these photocatalysts was found to be low. However, and to improve hydrogen production sacrificial agents, such as methanol or EDTA, were proposed due to their chemical nature that act as electron donor. These sacrificial agents have the disadvantage of not being renewable and the competition for implemented alternative sacrificial agents was launched [32,33].

In this respect, pioneering research, focuses on using oxygenates such as methanol, propanol, butanol, ethanol, glycerol, acetaldehyde, acetone, acetic acid among others. It has been reported as well, that glycerol, and butanediol could greatly enhance hydrogen production [33]. However nowadays more directly available biomass derived feedstocks such as ethanol, glucose, and sucrose are being considered. More specifically, ethanol be a sacrificial agent of choice given it can be obtained in low concentrations through sugar fermentation [34].

Figure 2.7 describes the mechanism of water dissociation using a sacrificial agent First an irradiated photon is absorbed on semiconductor. This leads to: a) An electron displacement to the conduction band leading to H_2 formation, b) A positive charge in the valence band (hole) yields a free radical $\bullet\text{OH}$ formation.

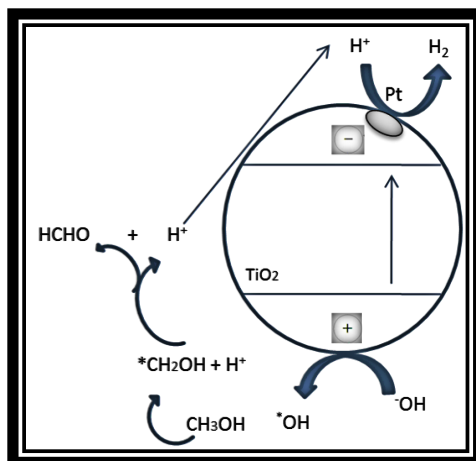


Figure 2.7 Reaction Scheme of Hydrogen Production with the Presence of a Sacrificial Agent (methanol).

The formed $\cdot\text{OH}$ radicals, are highly oxidizing species that can react with the sacrificial hydrocarbon agent (e.g ethanol). This $\cdot\text{OH}$ radicals trapped via the sacrificial agent conversion allows efficient separation of the $\cdot\text{OH}$ and H^+ radicals. $\cdot\text{OH}$ radicals trapping reduces charge recombination, thereof avoiding the reverse reaction leading to water formation [35].

2.2.3 Photocatalyst Selection for Hydrogen Production

The photocatalyst used in order to obtain H_2 , through the photo-dissociation of water has to satisfy certain requirements as follows: (i) To absorb visible light and to carry out the process of dissociation of water given its favourable band gap, (ii) To separate photo-excited electrons and holes, (iii) To minimize energy losses due to load transport and recombination of charge carriers, (iv) To have chemical stability against corrosion and photo-corrosion in aqueous environments, (v) To have an electron transfer capacity of the catalyst surface to water, (vi) To easily synthesize and be cheaply produced.

Therefore, the electronic structure of the semiconductor is a main parameter to be considered to have a viable water dissociation process, as shown in Figure 2.8. In this diagram, different types of semiconductors are examined given their energy band of gap position with respect to the energy potentials for oxidation/reduction of water [36].

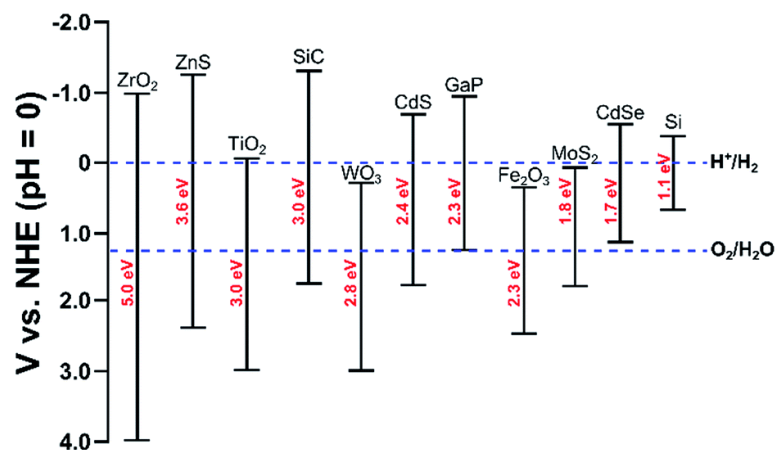


Figure 2.8 Energy Band Gaps for Different Semiconductors with respect to their Potentials (NHE) for Water Oxidation and Reduction [36].

Regarding the semiconductors reported in Figure 2.8, those that are thermodynamically viable for water dissociation are TiO₂, ZnO, CdS and SiC. For these reasons and given its high chemical stability, TiO₂ is considered a good semiconductor candidate for this type of process [2, 37-39].

However, for viable semiconductors it is required they display “forbidden” energy gaps higher than the theoretical value. This is the case given existing activation barrier in the charge transfer between the photocatalyst and water, and the recombination of charge carriers [7].

To reduce energy losses, the photocatalyst microstructure and photocatalyst external surface area must be carefully engineered. In general, high crystallinity has a positive effect on the photoactivity. Similarly, smaller particles reduce grain boundary effects and electron and hole recombination. Furthermore, and to have an efficient charge transport, charge carrier diffusion length must be larger than particle size. Therefore, the possibility of the charge carriers reaching the particle surface, increases with the reduction of the photocatalyst particle sizes [40].

2.2.4 Mesoporous Titanium Dioxide (TiO₂) Semiconductor

TiO₂ is a promising material for technological applications given its versatility [41-44], abundance, low toxicity, good chemical stability, photosensitivity as well as photo-stability [45-48]. In nature, it is found principally in the mineral ilmenite [49], that can be processed industrially by two different routes [50]; First stage, encompasses the reaction of the concentrate of ilmenite with hot sulphuric acid, resulting in the formation of sulphates of titanium, Fe(II) and Fe(III). The resultant solution is then purified and hydrolyzed to produce pure TiO₂ [51].

Another common method of manufacturing TiO₂ involves in combining the mineral with coke and gaseous chlorine under heating. This yields CO₂ and a spongy material rich in TiCl₄. The reaction product is subjected to successive fractional distillation, with the formation of TiCl₂ and TiCl₃. This is allowed given titanium species stability at various oxidation states. Finally, these precursors of titanium are hydrolyzed, forming titanium dioxide [52].

In 1972, Honda [5,23], achieved, for the first time, the successful decomposition of water under irradiation with light and without the application of electricity. These authors reported that when n-type TiO₂ was used as an anode and platinum as cathode, the TiO₂ electrode irradiated under short-circuit conditions, formed hydrogen at the platinum electrode, while oxygen evolved from the anode. Since then, numerous studies aimed at establishing TiO₂ applications were recorded in the open literature [6-14].

TiO₂ can be used in ultraviolet radiation absorbing filters [15, 53], in chemical sensors for gases [16-18], as a bactericide [19], in biomaterials for bone implants [20], in environmental photocatalysis [16, 21, 22, 54], in the photocatalytic hydrogen evolution [9, 55-60], and in dye-sensitized solar cells [13, 61-68].

The photocatalytic efficiency of TiO₂ depends on its structural and morphological characteristics, which are related to the method of synthesis used in the preparation of nanoparticles [10, 13, 21, 36]. To be photoactive and to favour the photocatalysis process, the TiO₂ must possess a high specific surface area, good porosity, with big sized pores [59,

69-70]. Besides this, TiO_2 in crystalline anatase form is also critical. In this context, the search for TiO_2 particles that have differentiated features, with catalytic properties potentiated, constitutes a field of intense activity [11-12, 38-40].

Due to the above, semiconductor properties such as, “forbidden” energy gap, crystallinity and surface area, are issues to consider when planning the synthesis and preparation of semiconductors suitable for water dissociation. In all these respects, the TiO_2 is a good photocatalyst for hydrogen production. As well, TiO_2 in its metallic oxide form is thermally stable, chemically and biologically inert, and non-toxic.

In terms of its crystallinity, TiO_2 forms can be found forming different phases: anatase, rutile and brookite, as shown in Figure 2.9. Out of these three phases, the anatase phase has better photoactivation [71]

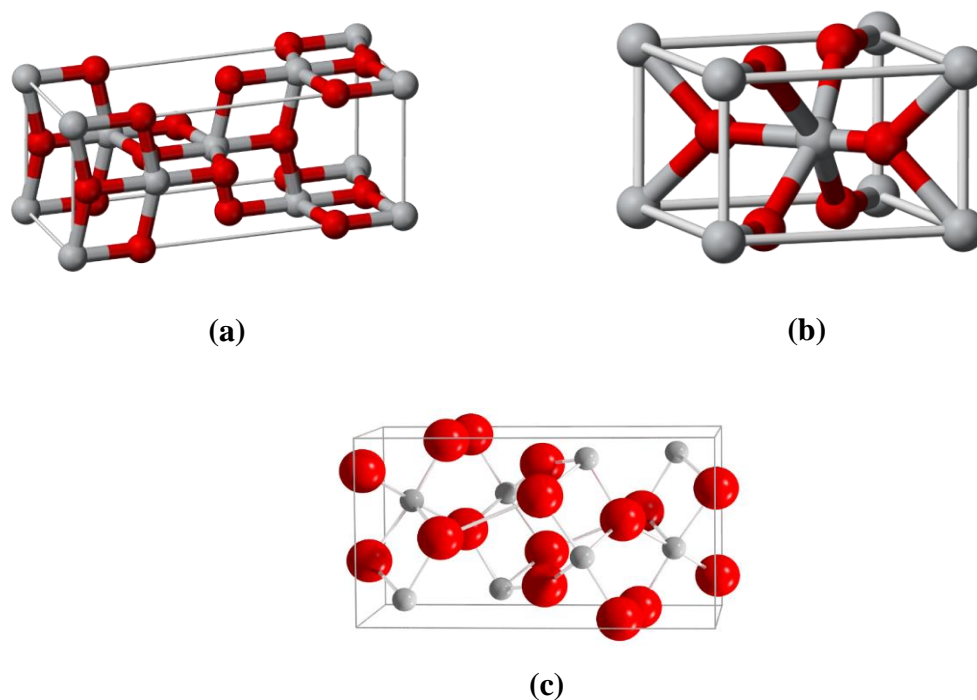


Figure 2.9 Unitary Cells of (a) Anatase, (b) Rutile and (c) Brookite. The gray and red spheres represent the oxygen and titanium atoms, respectively.

The TiO₂ energy band gap is 3.2 eV [71]. Thus, this energy band gap only allows photons in the UV radiation to activate TiO₂. As a result, either modifications of the “forbidden” energy gap or surface modifications can improve TiO₂ photocatalyst performance. Some of these possible photocatalyst modifications enhance H₂ production and will be discussed in following sections of this review.

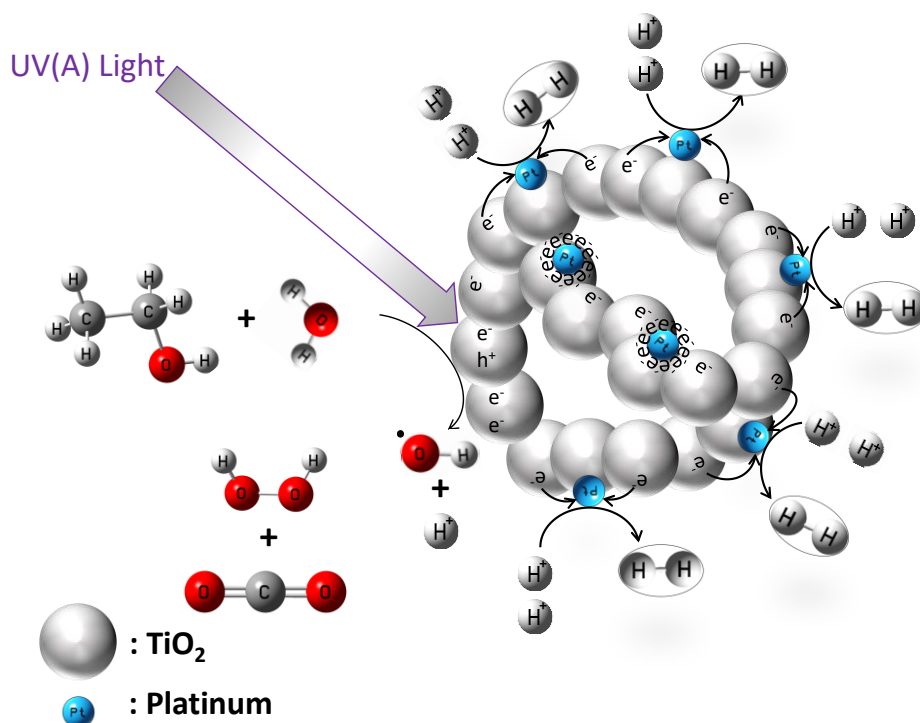


Figure 2.10 Photocatalyst TiO₂ with Pt as Co-Catalyst and organic scavenger.

The co-catalyst activity also depends a great deal on the amount of co-catalyst deposited on the photocatalyst surface. In addition, small metal particles on the TiO₂ may exhibit a higher negative change in the Fermi level, which benefits hydrogen production. [19]. In this respect, methodologies to carry out the deposition of Pt on TiO₂ have already been studied. These deposition methodologies involve precipitation, impregnation and photo-deposition [18,31,31-36].

However, when co-catalyst amounts exceed some limits, the co-catalyst may act as a recombination center of the electron/hole pairs reducing the photocatalyst efficiency [72]

2.1.3.1 Fermi level

The Fermi level is the total chemical potential for electrons (or electrochemical potential for electrons) and is usually denoted by μ or E_F . The Fermi level of a body is a thermodynamic quantity, and its significance is the thermodynamic work required to add one electron to the body (not counting the work required to remove the electron from wherever it came from). A precise understanding of the Fermi level how it relates to electronic band structure in determining electronic properties, how it relates to the voltage and flow of charge in an electronic circuit is essential to an understanding of solid-state physics.

2.2.5 Band Gap Energy

To develop active photocatalysts under visible light, it is necessary to have a close control of the material electronic structure of the material. To accomplish this, there are different possible strategies which can be classified into three categories: (i) synthesis of a semiconductor composite, (ii) synthesis of a semiconductor alloy, (iii) anion or cation doping.

Mixing semiconductors and forming composite semiconductors, is a possible approach to develop a visible light active photocatalyst. This strategy is based on coupling two semiconductor properties. One of them can have a large “forbidden” energy gap (Semiconductor (a)) while the other a small “forbidden” energy gap (Semiconductor (b)). Figure 2.11 describes the “forbidden” energy gap for each of them. Thus, the more negative conduction band (CB) of Semiconductor (a), allows an electron injection at the Semiconductor (b) CB.

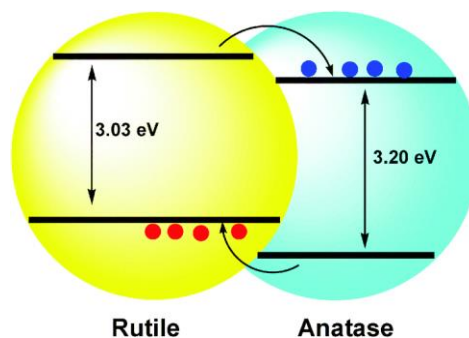


Figure 2.11 Electron Injection in a Semiconductor Composite such as Anatase-Rutile (a)-(b) Type.

Semiconductor composites can couple CdS ($E_g = 2.4$ eV) and SnO_2 ($E_g = 3.5$ eV). These composites can produce hydrogen under irradiation of visible light, using the EDTA sacrificial agent [73]. On the other hand, the coupling of TiO_2 with a semiconductor with a “forbidden” energy gap was also investigated. These TiO_2 composites were proved to be more efficient under UV irradiations [74].

It is anticipated that for semiconductor composites to succeed for hydrogen production the following has to be met: (i) Both semiconductors should not be influenced by photo-corrosion, (ii) electron injection should be possible, (iii) Semiconductor (b) should be excited with visible light, (iv) the Semiconductor (b) CB energy level should be more negative than the Semiconductor (a) CB energy level, (v) the CB of the semiconductor (b) should have a larger negative energy level than the water reduction level.

A second strategy to extend the response of a semiconductor under visible light involves a solid solution between semiconductors with both a wide and narrow “forbidden” energy gap with both materials having a closely similar crystal lattice. Figure 2.12 provides a schematic of such solid solution

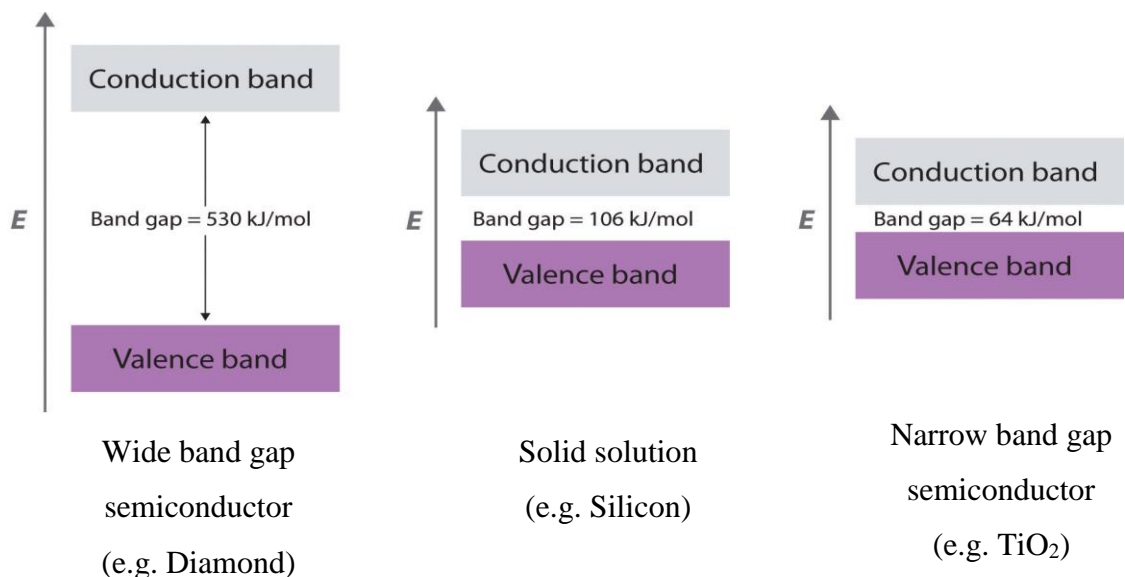


Figure 2.12 Band Diagram of a Solid Solution of Three Semiconductors.

Solid solutions of two or more semiconductors require crystalline structures to be thoroughly interdispersed. In these systems, the “forbidden” energy gap can be modified depending on the solid solution components. The following are the requirements for such a solid solution: a) that each semiconductor is photoactive at a characteristic wavelength, and b) that after interdispersion, the composite material absorbs the entire visible light wavelength range. Examples of these semiconductor alloys are GaN-ZnO, AgInSe₂-ZnSe, g-C₃N₄, and ZnS-AgInS₂ [75-77].

Transition metals and rare earth metals have been investigated considering ions that can be used for doping semiconductor oxides such as TiO₂. In this respect, the replacement of a cation in the semiconductor crystalline lattice having a wide energy gap, creates energetic levels within the photocatalyst “forbidden” energy gap. This facilitates visible spectrum range photon absorption, as described in Figure 2.13 [16].

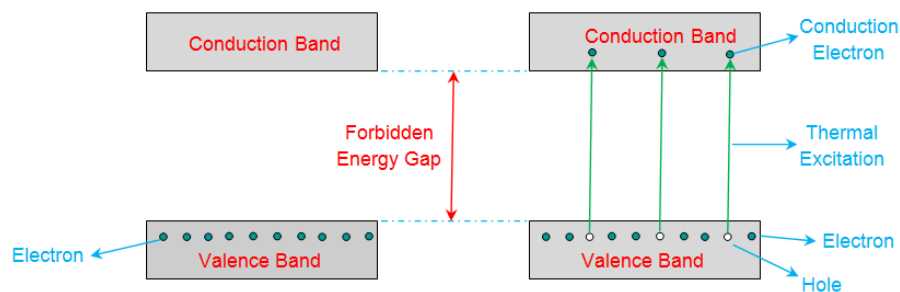


Figure 2.13 Energy Diagram of a Semiconductor Doped with a Cation.

In summary, and in spite of literature reported strategies, they are still pending issues to improve photocatalyst response or to avoid recombination of charge carriers. It is with this goal in mind that synthesis and preparation of photocatalysts based on TiO_2 were planned as important activities in the context of the present PhD dissertation.

2.2.6 Porosity and Porous Materials

Porosity is a physicochemical property related to the cavities (pores), channels or interstices in a solid particle. It is a property of great importance since it is related to the ability of materials to interact with atoms, ions, molecules, and nanoparticles not only on their extended surfaces but also throughout the bulk phase containing these particles [71, 78]. Thus, the control of solid porosity in semiconductors very important [72, 79].

Pores can be classified as open or closed, Figure 2.14 shows various types of open and closed pores as well as typical shapes.



Figure 2.15 Schematic Representation of a Porous Solid, Showing the Most Common Types of Pores: a: closed pores, b,c,d,e,f : open pores, b,f: blind pores, e: through pores

and most common shapes, c: cylindrical open, f: cylindrical blind, b: ink-bottle-shaped, d: funnel shaped and g: roughness.

Open pores have continuous channels that communicate to the outer surface of the material, generating a cross-linked structure. Pores are related to catalyst macroscopic properties such as mechanical resistance and thermal conductivity [80]. Closed pores are inactive for the flow of liquids, gases and other substrates, being totally isolated from their vicinity. Pores can also be interconnected and can be classified as (a) bottleneck, (b), cylindrical, (c), and funnel type, (d). The surface roughness, can also be an important property to account for [80].

The three classes of porous materials, according to the International Union of Pure and Applied Chemistry (IUPAC) definition, include the following: microporous (pore diameter <2 nm); mesoporous (pore diameter in the range of 2–50 nm); and macroporous (pore diameter >50 nm) materials [5]. Microporous materials have relatively small pore sizes, such as with the zeolite family. However, mesoporous materials have the potential to remove these barriers due to their large pore diameters (2–50 nm), large pore volumes, and ordered pore channel arrangements. Moreover, the high surface and large pore volume provide an avenue to disperse active sites. The final class, macroporous materials have very large pore diameters but usually low surface areas and are employed in photonic applications, such as waveguides. This pore size classification is based on measurements of adsorption-desorption of N_2 at boiling temperature and on the statistical width of layers of adsorbed N_2 .

The analysis of these data is usually done by using the Brunauer-Emmett-Teller Method (BET), proposed by Stephen Brunauer, Paul Hugh Emmett e Edward Teller [81-83]. By employing BET, it is possible to describe the forms of the adsorption and desorption isotherms for a specific solid. By knowing the form of the isotherm, it is possible to define its porosity [84].

Figure 2.15 reports typical isotherms for various solids.

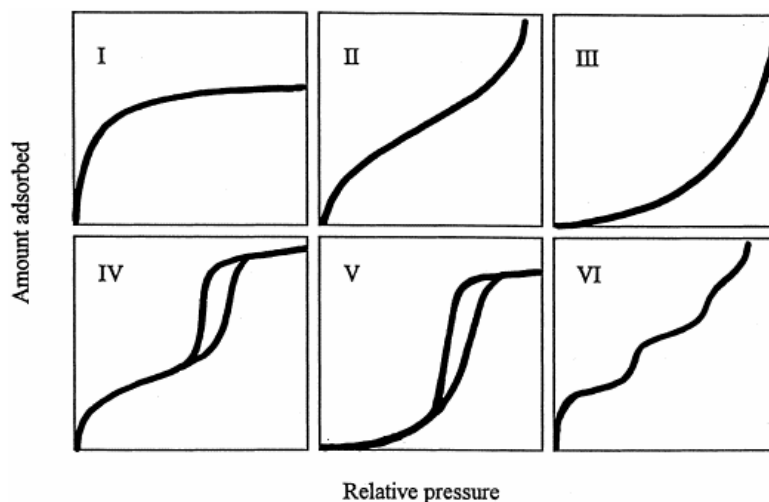


Figure 2.16 Representation of the Six Main Types of Isotherms: I, microporous solids; II, non-porous solids; III, macroporous solids; IV and V, mesoporous solids; VI, non-porous solids with a uniform surface.

In this respect, isotherm I belongs to microporous solids, while isotherms II and III are related to finely divided non-porous solids or macroporous solids. As well, isotherms type IV and V present a hysteresis loops, which are characteristic of N₂ condensation in mesopores. The type IV hysteresis represents materials with uniform porosity, while type V hysteresis refers to pores with non-defined shapes and sizes. Finally, the type VI hysteresis is related to non-porous solids with an almost uniform surface [73,84].

2.2.7 Mesoporous Nanostructured TiO₂

Organized mesoporous nanostructured titanium dioxide (TiO₂) is one of the most promising semiconductor materials [11-13, 35, 74-77, 84-90]. The presence of pores in nanostructured materials tends to enhance their physical and chemical properties. Compared with bulk TiO₂, the uniform channels in mesoporous TiO₂ do not only increase the density of active sites with high accessibility. They also facilitate the diffusion of reactants and products. Furthermore, the high surface area and large pore volume provide an enhanced capability for dye loading and pollutant adsorption [84,85]. It is also possible to produce mesoporous TiO₂ using template-free methods. However, these materials

usually present disordered mesostructures, and this because of the irregular packing of their building blocks [84].

2.2.7.1 Surfactants as Drive Agents in Obtaining Mesoporous Ordered Materials

Certain surfactants can act as structural templates, during the semiconductor synthesis. Structural templates promote specific semiconductor architectures. This process occurs due to the spontaneous oxide nuclei forming around a surfactant molecule. This condition controls the initially microstructure formation and the later growth. This mesoporous semiconductor synthesis yields an ordered material. The architecture and its physicochemical properties can be controlled with the concentration of the surfactant employed [13, 91].

For a successful mesoporous semiconductor synthesis, the surfactant (X) and the inorganic species (I) need to interact as [91]:

- 1) X^+I^- : cationic surfactants are needed as structural drivers for negatively charged inorganic species;
- 2) X^-I^+ : anionic surfactants are required as structural drivers for positively charged inorganic species;
- 3) $X^+X^-I^+$: Both the surfactant and inorganic species must be positively charged and this in the presence of opposite charged species. These species act as counter ions;
- 4) $X^-X^+I^-$: Both the surfactant and inorganic species must be negatively charged and this in the presence of a species of opposite charge. These species act as counter ions;
- 5) $X^0 I^0$: Both the surfactant and the medium must favour neutrality for the inorganic species. In this case, the interaction between the species occurs through hydrogen bonds or dipoles.

Thus, the concentration of the surfactant in the reaction medium must be higher than the critical micelle concentration (CMC), and favour the auto-assembling of micelles. This phenomenon promotes bi and three-dimensional arrays responsible for the empty spaces that lead to nanopores material synthesis [91].

2.2.7.2 Sol-Gel method

The sol-gel method has become the most widely used for the synthesis of semiconductor photocatalysts. It is a powerful method for tailoring metal oxides to fit particular applications due to a great number of parameters can be controlled; i.e., the nature of the precursors, reagent concentrations, aging temperature and time, temperature as well as time of reaction, pH, catalyst nature and concentration, the amount of added water, addition of organic additives. One of the main advantages of the sol-gel method is the homogeneous mixing at the molecular level of metal ion which promotes the formation of polycrystalline particles with characteristic properties. Another important advantage of the sol-gel method is that through some stage of the process it is possible to incorporate different types of dopants. The incorporation of an active dopant in the sol during the gelation stage allows doping elements to have a direct interaction with support in such a way that the photocatalytic properties of the material can be enhanced.

2.2.7.3 Synthesis of mesoporous TiO₂ using Sol-Gel method

Among the methodologies of TiO₂ mesoporous synthesis, the methods of sol-gel and homogeneous precipitation best favour the control of morphology [82, 92, 93]. The term sol-gel involves several synthesis methodologies based on hydrolytic processes [11, 12, 83, 94]. Hydrolysis and condensation reactions involving the precursor, allow the formation of colloidal particles (sol) and the subsequent formation of three-dimensional networks (gel). This process ensures a good homogeneity for the reaction product, leading, in general, to metastable phases, amorphous or not [95]. In the case of amorphous materials, a step for the crystallization of the oxides formed, is required.

The use of solvothermal conditions is an alternative to the conversion of the amorphous material to crystalline material without the use of high temperatures [84, 93]. The solvothermal method consists in the dissolution of a metallic precursor in anhydrous benzyl alcohol while being heated at temperatures above 423 K. Under these conditions, the alcoholic hydroxyl group connects partially to the metal ion, starting a polycondensation reaction. Due to the greater volume of the organic group, steric hindrance, tends to control

the formation of nanoparticles. This is the case since nanoparticles tend to stabilize in smaller sizes and narrower size dispersions than those obtained in the sol-gel process [96].

The hydrothermal method represents a variation of solvothermal method in which the solvent is water. Under hydrothermal conditions, the solubility of the amorphous particles increases significantly. Furthermore, crystal formation can occur concurrently with re-dissolution and re-precipitation [95, 97, 98]. This method has been widely used, since small variations in the main synthesis parameters (pH, concentration of precursor, among others) can cause significant changes in morphology, size, chemical constitution, and other properties of the synthesized nanostructures.

The homogeneous precipitation method has also been studied widely due to its great versatility. In this case, chlorinated precursors of titanium or even titanium tetra-isopropoxide react with a base (sodium or ammonium hydroxide) forming titanium hydroxide. This compound is converted through the loss of water into amorphous TiO_2 , which, under different thermal treatments, gives rise to the three known crystalline forms [99].

The combination between these synthesis strategies and the use of molecular templates warrants better control in ordered mesoporous materials. In this sense, two approaches can be highlighted: the soft template and hard template methods [84].

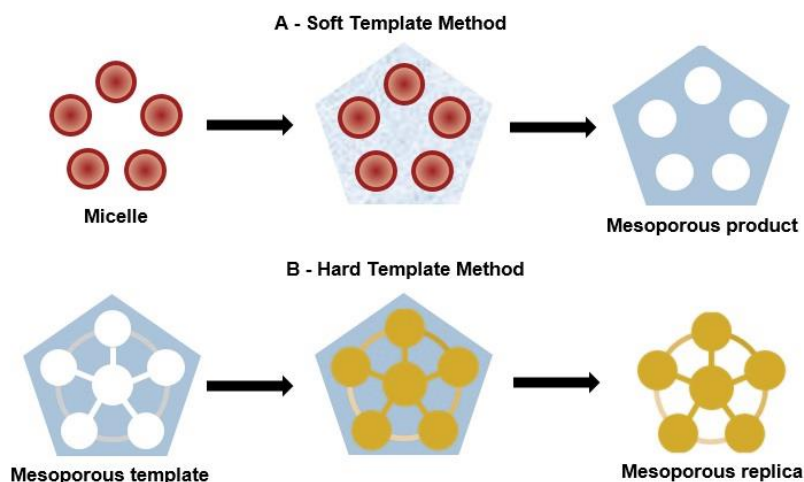


Figure 2.17 Schematic Representation of (A) Soft-Templating and (B) Hard-Templating.

The soft-templating method consists in the use of a template in the liquid phase. It is widely used in the sol-gel processes based on titanium precursors. Due to its high chemical reactivity, these precursors tend to suffer hydrolysis, giving rise to dense precipitates very quickly. The self-structuration of surfactants can lead to mesostructured sol particles. This occurs through the spontaneous organization of molecules around automounted micelle structures, usually in an aqueous medium, and gives rise to colloidal nanocrystals.

Studies have suggested that two mechanisms are related to the formation of mesoporous materials via the soft-templating method [91, 100-102]. The first is known as the Cooperative Self-Assembly (CSA), and the second, is identified as the Liquid Crystal Template (LCT). In the CSA, there is a simultaneous aggregation between the inorganic precursor and the surfactant. This includes the formation of a liquid crystal-like phase with cubic, hexagonal or lamellar arrangements, containing both micelles and the inorganic precursor. On the other hand, in the LCT mechanism the concentration of surfactant is so high that a liquid-crystalline phase is formed without the presence of inorganic precursors. In both mechanisms, after the formation of the material, it is necessary to remove the template to obtain the porosity. For this, the procedure most commonly used is calcination [91].

In 1992, scientists from Mobil Oil Corporation [103], reported mesoporous silicate molecular sieves synthesis, denoted by M41s. These were synthesized using a macro-molecule-templating process, that gave rise to a new and fascinating field of research. Subsequently, efforts have been concentrated in studies related to the synthesis and application of mesoporous materials [2, 92, 104-111].

In 1995, the preparation of mesoporous TiO₂ using a sol-gel method associated with a surfactant as a structural template was at first reported [112]. Since then, efforts have been made to propose methods of synthesis of ordered mesoporous TiO₂. These aim at contributing to the improvement of the photocatalytic activity of this material, by using diverse applications [113-116].

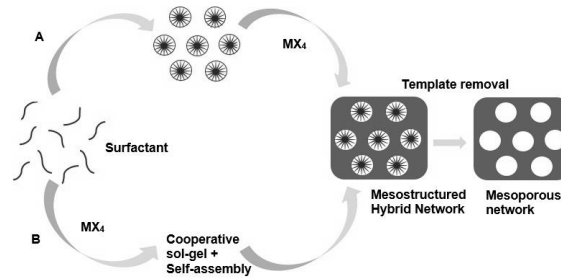


Figure 2.18 Schematic Description of the Formation of Mesoporous Structures: Cooperative Self-Assembly Process, and Liquid–Crystal Templating Process.

Nanometric structures of mesoporous TiO₂ were produced using the sol-gel methodology, under acidic (pH 3 to 4) and alkaline (pH 7 to 9) media, using cetyl trimethyl ammonium bromide (CTAB), sodium dodecyl benzene-sulphonate (DBS) and nonylphenol ethoxylate as surfactants (NPE) [92]. In this respect, the effects of the surfactant and the pH on the morphology, the particle size, the surface area, and the pore size distribution were studied. The synthesized oxides were evaluated for the degradation of naphthalene.

Using CTAB under acidic pH, the nanometric material was 100% anatase, while under alkaline pH, the material was produced in two crystalline phases, anatase (85%) and brookite (15%). In the presence of DBS, under acidic pH, an 85% anatase and 15% rutile was obtained. Additionally, under alkaline pH, the crystalline phase was 100% anatase. Nevertheless, by using NPE under acidic pH, a mixture of 94% anatase and 6% rutile was produced, while under alkaline pH, the phases were anatase and brookite (8%). The authors [92] suggested that the good results obtained for the degradation of naphthalene (96% up to 4 h under irradiation in the visible at $\lambda > 400$ nm), using the mesoporous material obtained in the presence of CTAB in acidic medium, was due to the resulting specific surface area ($87 \text{ cm}^2 \text{ g}^{-1}$) and to the mean pore volume ($0.057 \text{ cm}^3 \text{ g}^{-1}$).

A variant of the Soft-Templating Method is the Evaporation Induced Self Assembly (EISA) [117, 118]. This method was originally designed for the preparation of thin films of mesostructured silica [100]. It has been successful in obtaining different mesoporous materials (TiO₂, ZrO₂, Al₂O₃, Nb₂O₅, Ta₂O₅, WO₃, HfO₂, SnO₂,) [79, 80]. In this method, organic solvents such as ethanol, propanol, are used as a reaction medium. Using non-

aqueous medium and block copolymer surfactants, the rate of hydrolysis as well as redox reactions and phase transformation are minimized. EISA presents advantages when compared to aqueous sol-gel reactions, such as better control and homogeneity in the formation of particles, high crystallinity at reaction temperatures between 373 and 573K.

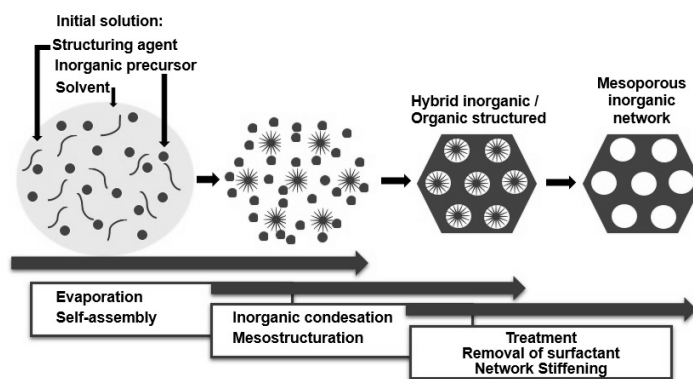


Figure 2.19 Schematic Description of Most Representative Steps of Evaporation Induced Self-Assembly (EISA).

A methodology capable of producing monodisperse spheres of TiO_2 at room temperature, using titanium (IV) butoxide (TBT) mixed to ethylene glycol, as template, was proposed by Yang et al. [99]. The mixture was subsequently subjected to a conventional hydrothermal treatment. Thus, it was possible to obtain nanoparticles with a surface area up to $233.2 \text{ m}^2 \text{ g}^{-1}$ and a mean pore volume of $0.27 \text{ cm}^3 \text{ g}^{-1}$. The photocatalytic activity of the synthesized material was evaluated using the degradation of methylene blue, Red MX-5B and phenolphthalein under UV irradiation. Kinetic constants of degradation of 6.7, 13.2, and 14.7 min^{-1} , respectively, were attributed to the higher specific surface area of the catalyst.

As well, the synthesis of TiO_2 spheres based on EISA, using titanium (IV) tetra-isopropoxide and Triton X-100 was reported, aiming their application in the DSSC as described in Figure 2.18 [100]. The particle size could be controlled by changing the Ti/ H_2O molar ratio and adjusted between 500 and 1100 nm, with a surface area in the range of $55\text{-}150 \text{ cm}^2 \text{ g}^{-1}$.

By using the EISA strategy, excellent photocatalysts based on CeO₂, capable of oxidizing harmful gases, such as CO, NO_x and hydrocarbons, in non-toxic gases, were synthesized [102]. The triblock copolymer P123 and polyvinyl pyrrolidone (PVP) were used as templates. In this sense, photocatalysts with different pore sizes (about 40 μm, 2 μm and < 0.3 μm) and the specific surface area of 32.5 m² g⁻¹ were produced.

Collapse to the mesoporous structure may occur due to the presence of residual template. Possible damage may involve the blocking of pores or even the poisoning of photocatalytic sites on the surface of the mesoporous material. In this sense, calcination has been identified as a method to eliminate some surfactants [119]. Non-ionic surfactants, as Triton X-100, can be simply removed by washing the oxide formed [120].

Concerning the hard-templating method the solid is formed around a template, usually composed of zeolites and meso- and macroporous silica, via interactions between the template and the precursor [84]. This methodology is more complex when compared to the soft-templating method. Nevertheless, hard templating is highly effective in obtaining mesoporous structures [121]. Through this methodology, nanostructures are formed on surface of templates [122].

The synthesis of uniform TiO₂ sized nano-spheres, based on hard-templating and using silica as template and (NH₄)₂TiF₆ as precursor, was proposed by Tang et.al. [123]. This synthesized material displayed a 54.2 m² g⁻¹ surface area and 0.15 cm³ g⁻¹ pore volume. The photocatalytic activity was evaluated by using the degradation of the dyes of methylene blue, rhodamine B and methyl-orange. The levels of degradation were 95%, 95% and 90%, respectively. These excellent results were attributed to the high specific surface area and charge separation in the monodispersed resulting materials.

Chen et.al. [124] proposed synthesizing mesoporous TiO₂ by using a combination of hard- and soft-templating methods. By using mesoporous silica in the first step (hard-templating), and Pluronic P123 as structure directing agent at the soft-templating stage, this allows particle morphology control. This yielded three-dimensionally ordered mesopores with a 145 m² g⁻¹ specific surface area and 0.246 cm³ g⁻¹ specific pore volume. Due to the porous nature of the material obtained and due to the three-dimensional

periodicity of the spheres, the authors highlighted the possible applications of these materials for environmental photocatalysis, solar cells and lithium rechargeable batteries.

Table 2.2 reports the main differences between the hard and soft-templating methods. As well, Table 2.2 reports the structures of the main surfactants suggested as structure directing agents, for the synthesis of mesoporous materials.

Table 2.2 Comparison between Hard and Soft-Templating

Differences between Hard and Soft-Templating Methods	Hard-Template Features and Issues	Soft-Template Features and Issues
➤ Synthesis Procedure	❖ Multiple steps involved in its preparation	✓ Fewer steps involved in its preparation
➤ Template Used	❖ Mesoporous silica obtained	✓ Surfactants (Block copolymers) required e.g. Pluronic P123 or F127
➤ Mesoporosity Control	❖ Fixed and restricted applications due to the pre-formed structures of the hard template	✓ Tunable architectures and surface properties which are pH and temperature dependent.
➤ Prospect of Applications	❖ Expensive, time-consuming, unsuitable for large scale industrial production	✓ Low cost, convenient, suitable for large scale industrial applications.

2.3 Block co-polymers, Pluronic P123 and Pluronic F127

Block co-polymers, at appropriately strong degrees of block segregation, self-organize into nanoscale domains with an interfacial curvature and conforming domain structure that depend on the volume fraction of one block relative to that of the other block. The Pluronic types are block co-polymers based on ethylene oxide and propylene oxide. They can

function as antifoaming agents, wetting agents, dispersants, thickeners, emulsifiers and structure directing agents.

Pluronic P123, is a non-ionic symmetric triblock co-polymer constitutes of *poly(ethylene oxide)-poly(propylene oxide)-poly(ethylene oxide)*, $(-\text{CH}_2\text{CH}_2\text{O}-)_{20}-(\text{CH}_2(\text{CH}_3)\text{CHO})_{70}(-\text{CH}_2\text{CH}_2\text{O}-)_{20}$, ($M_{\text{AVG}}=5,800$). The structure of Pluronic P123 is presented in Figure 2.20.

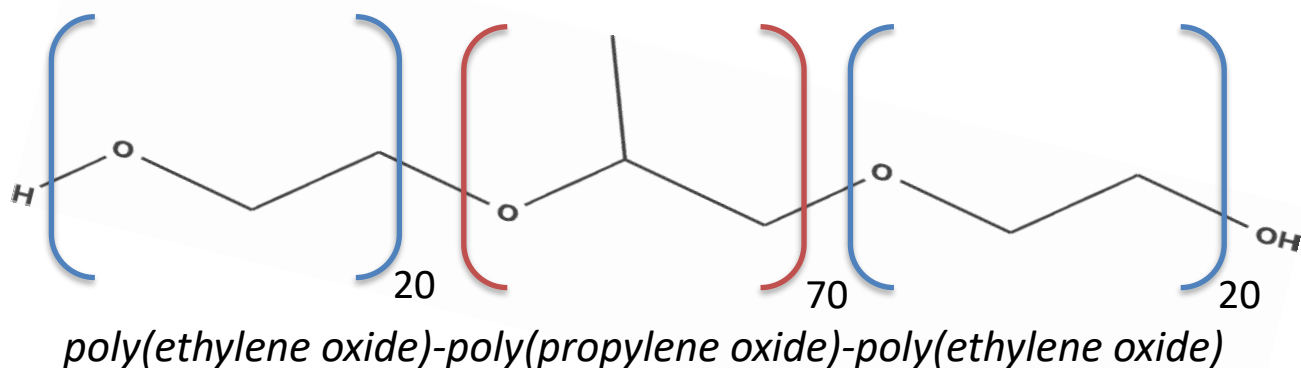


Figure 2.21 Structure of Pluronic P123.

Pluronic F127, is a non-ionic symmetric triblock co-polymer created of *poly(ethylene oxide)-poly(propylene oxide)-poly(ethylene oxide)*, $(-\text{CH}_2\text{CH}_2\text{O}-)_{106}-(\text{CH}_2(\text{CH}_3)\text{CHO})_{70}(-\text{CH}_2\text{CH}_2\text{O}-)_{106}$, ($M_{\text{AVG}}=12,600$). The structure of Pluronic F127 is presented in Figure 2.22.

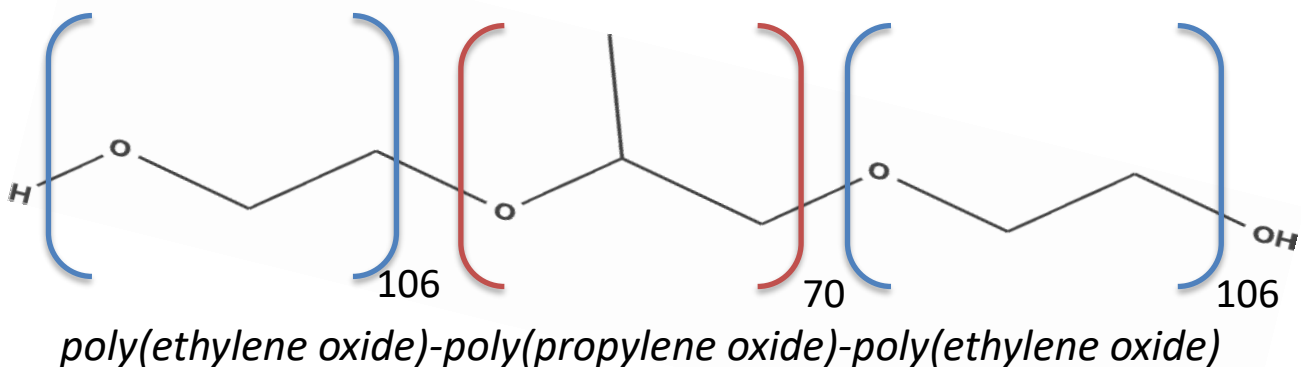


Figure 2.23 Structure of Pluronic F127.

2.4 Quantum Efficiency

The specialized literature is densely populated by photocatalysis studies which require important additional specifics about photocatalytic efficiency. In this respect, photocatalytic conversion alone does not allow adequate assessment of conductor materials and photocatalytic reactor designs. Not having this important data hinders scientific and technological progress.

A key parameter in this analysis is the quantum efficiency. This is a parameter that can also help in reaction pathway discrimination. Different definitions for quantum efficiency have been proposed, leading to different approaches in assessing their photoreactor energy efficiency [25-26]. Ibrahim [125] and de Lasa et al. [126] have provided detailed summaries of possible quantum yield definitions. Other definitions using the incident photon flux [127-135] can be found in the literature, but most of them are of uncertain utility.

Quantum parameters are key and useful efficiency estimators in photocatalysis. These parameters are based on “*number ratio*”, either of photoconverted molecules over absorbed photons, or photoconverted molecules over photons entering the reactor, as illustrated in the following table.

- I. Primary Quantum Yield,
- II. Overall quantum yield and,
- III. Apparent quantum yield or global quantum yield.

Table 2.3 Quantum Parameters Definitions (Ibrahim, 2001)

Parameter	Definition and Literature Reference
Primary Quantum Yield (Primary QY)	$\frac{\text{number of pollutant molecules degraded from a primary process}}{\text{number of a photons absorbed}}$ <p style="text-align: center;">Cassano et al., (1995), Davydov et al., (1999)</p>
Overall Quantum Yield (Overall QY)	$\frac{\text{number of pollutant molecules degraded from a primary and second process}}{\text{number of a photons absorbed}}$ <p style="text-align: center;">Cassano et al., (1995)</p>

Quantum Yield (Apparent QY)	$\varphi = \frac{\text{number of pollutant molecules degraded}}{\text{number of photons absorbed}}$
	Valladares and Bolton (1993), Yamazaki-Nishida et al., (1994), Peil and Hoffman (1995)
Apparent Quantum Yield (*) or Global Quantum Yield (QE)	$\varphi_{app} = \frac{\text{number of pollutant molecules degraded from a primary process}}{\text{number of photons entering the reactor}}$
	Fox and Dulay (1993), Nimlos et al., (1993), Zhang et al., (1994), Sczechowski et al., (1995).

(*) the term “apparent or app” is also introduced to highlight the difficulty of measuring absorbed photons.

The *Primary Quantum Yield* (Primary QY) establishes the number of molecules degraded from a primary process or event that involves direct absorption of radiation over the number of photons absorbed [127, 128]. Cassano et al., [127] argue that according to the second law of photochemistry, the absorption of light by a molecule is a one-quantum process. Therefore, a quantum yield factor involving the sum of all primary processes must be less than or equal to unity. This is the result that the energy absorbed by the molecule is partially lost by re-emission, collision or other processes.

The *Overall Quantum Yield* (Overall QY) is defined as the ratio of the total number of pollutant molecules degraded via primary and secondary processes over the total number of photons absorbed [127]. This Overall Quantum Yield can, in principle, be higher than 100 % [127]. This fact puts forward interesting prospects for photocatalytic processes.

There are, in this regard, several studies that consider photocatalytic efficiencies with significant differences in their definitions. As an illustration, one could use the empirical/semi-empirical factors, like the electrical energy per order (EE/O) for efficiency calculations. The EE/O is defined as the electrical energy used, to reduce the concentration of a pollutant by an order of magnitude. The EE/O assumes a first order photoconversion rate.

Additionally, there are other further fundamentally based efficiency factors which equate the rate of photoconversion with the rate of irradiated photons. These types of evaluations,

can be implemented at any time during the irradiation period and lead to the so-called “rate based efficiencies”. One can note that the “rate based efficiency” does not require any specific assumption regarding the reaction order of the photoconversion kinetics as is the case of the EE/O.

A typical example of the “rate based efficiencies” is the Photonic Efficiency (PE). This parameter relates, the rates of reactant molecules transformed, or product molecules formed, to the rate of incident photons on the reactor walls [29] as follows:

$$\text{Photonic Efficiency (PE)} = \frac{\text{Rate of Reactant Molecules Transformed}}{\text{Flux of Incident Photons}} \quad (2.11)$$

The *PE* as in Eq. (2.11), provides an overall photonic efficiency. This is the case given that it involves a numerator (rate of reactant molecules transformed) and a denominator (rate of incident photons). Both are not directly related to the central and primary photocatalytic event.

This essential and primary photocatalytic step is, however, the one leading to $\bullet OH$ radicals being promoted by the separation of charges and the absorbed photons. It is on this basis, that a more adequate photocatalytic efficiency should be established using the *QY* quantum yield. The *QY* is a parameter defined as the number of primary $\bullet OH$ radicals produced on the catalyst surface (e.g. $\bullet OH$) over the flux of photons absorbed by the photocatalyst.

$$QY = \frac{\text{Rate of Primary Radical Produced}}{\text{Flux of Photons Absorbed}} \quad (2.12)$$

Quantum Yields, in the case of hydrogen production, can be represented as follows:

$$\varphi = \frac{\text{number of } H_2 \text{ molecules produced}}{\text{number of photons absorbed by the photocatalyst}}$$

Consequently, one could define the “Theoretical Quantum Yield” based on the photon production as follows:

$$\varphi_{theor} = \frac{\text{moles of } H\bullet}{\text{moles of photons}}$$

However, a more valuable definition of quantum yields for hydrogen production via water splitting using a scavenger is as follows:

$$\varphi_{theor} = \frac{\text{moles of } H\bullet + \text{Mole of } \bullet OH}{\text{moles of photons}}$$

In contrast to Eq. (2.11), it can be observed that the *QY* in Eq. (2.12) is based on the absorbed photons reaching the reactor walls or catalyst surface. One should note that this *QY* definition is of general applicability and can be used for either internally or externally irradiated photoreactors. Even if the *QY* is a most appropriate efficiency parameter to describe photochemical activity, there are still discrepancies between authors regarding its proper application.

One could note that there are still authors which base their quantum yields on the rate of incident photons instead of on the phenomenologically sound photon absorbed rate. These quantum yields provide an underestimated *QY* value only.

Finally, one can define a “Relative Photonic Efficiency” parameter as: the ratio between the actual *QY* and the *QY* for a reference photocatalyst and model pollutant (e.g. conversion of phenol on Degussa P25). This reported “Relative Photonic Efficiency” may have a limited practical value,

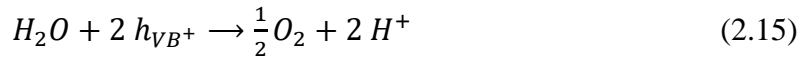
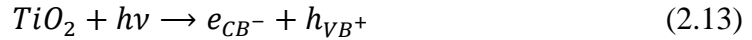
2.4.1 Maximum Expected Quantum Yields

Regarding *QYs*, one can consider the following issues:

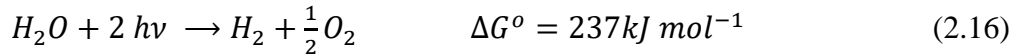
- a) Are *QYs* observed smaller or equal to 1 or the equivalent $QY \leq 1$? If this is proven, one can hypothesize with confidence, that a photocatalytic reaction mechanism based on 1 photon hitting the semiconductor surface, and yielding both 1 vacant site (h^+) and 1 electron, is adequate. Furthermore, if this assumption is proven, it could also allow one to discard other claimed chain reaction mechanisms.
- b) Are the *QYs* complying with $QY < 1$, displaying large and close to one values? Evidence of these *QYs* allow questioning or discarding altogether the potential significance of electron-charge recombination. If demonstrated, this may validate photocatalysis as a technology of

great potential, creating opportunities for performing photocatalysis in unique reactor designs with high QYs [29].

As shown in Figure 2.3, in the case of water cleavage, the electron-acceptor species are H^+ ions (protons), whereas water molecules, or hydroxyl anions, are the electron-donor species, according to the following series of reactions:



Hence, the global photocatalytic water splitting reaction is:



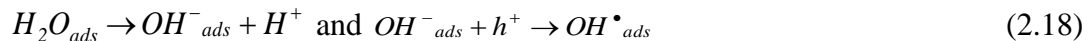
The above-mentioned reaction is accompanied by a positive Gibbs Free Energy Change. It is a thermodynamically up-hill reaction. Consequently, it may be regarded as a sort of artificial photosynthesis process, in which photon energy is converted and stored in the form of chemical energy.

However, de Lasa and Garcia Hernandez [136] described the photoconversion of organic pollutants via photocatalysis as follows:

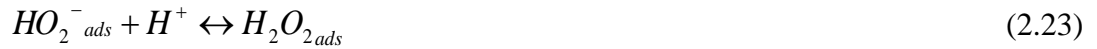
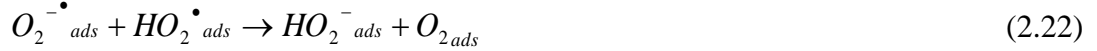
- a) The electron/hole pairs react with water molecules or hydroxyl ions adsorbed on the surface of the TiO_2 producing hydroxyl radicals:



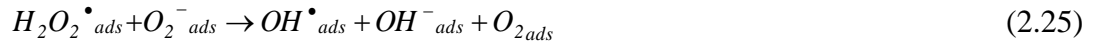
or



- b) The electrons react with oxygen to form superoxide radicals. The hydrogen peroxide is formed according to Equations as follows:



c) Hydroxyl radicals ($\bullet OH$) are generated from the hydrogen peroxide formed, as follows:



The linear combination of the previous equations leads to the following expressions:



or



As a result, once one considers the “overall” stoichiometry for the formation of $4OH^{\bullet}$ radicals given by Eq. (2.18), one can see that this involves: a) 2 H_2O molecules, 2 photons, 2 vacant sites and 2 electrons yielding 2 $\bullet OH$ radicals, as per Eq. (2.10)-(2.18), b) 1 extra photon however, is needed for the conversion of H_2O_2 into 2 $\bullet OH$, as shown in Eq. (2.19)[136]. Thus, this yields the following:



or a maximum quantum yield as follows:

$$QY_{max} = 1.33 \text{ or } 133\% \quad (2.30)$$

Thus, one can notice that the highest Quantum Yield or QY_{max} percentage that one can be obtained, neglecting all possible electron-vacant site recombination is 1.33 or 133%.

In this respect, if one would like to analyze mechanisms in photocatalysis using QYs , one should check that the QYs , do not surpass the $QY_{max} = 1.33$ upper limit, with this being in compliance with the overall 1 vacant site -1 one electron mechanism.

It is interesting to notice that the 1.33 stoichiometric limit for QY or QY_{max} is an observed constraint for the photocatalysis of organic pollutants both in air and water, as shown by Garcia Hernandez et. al. [136].

2.4.2 Quantum Efficiencies and Quantum Yields (QY)

One of the important parameters in photocatalytic systems is the Quantum Efficiency which allows comparing different types of photocatalysts for the same process. The quantum efficiency of a photocatalyst is defined by the number of photo-produced or photo-converted molecules over the number of photons absorbed by the catalyst. The quantum efficiency for the production of hydrogen is presented below:

$$QY_{theor} = \frac{\text{moles of } H^{\bullet}}{\text{moles of irradiated photons}}$$

However, in hydrogen production systems, where a sacrificial agent is present, the above definition changes, to take into account the number of $\bullet OH$ radicals that are produced simultaneously and react with the sacrificial agent.

Furthermore, a more relevant Quantum Yield for hydrogen production via water splitting using a scavenger can be defined as follows:

$$QY_{H^{*+OH^{*}}} = \frac{\text{moles of } H^{\bullet} + \text{Mole of } \bullet OH}{\text{moles of photons absorbed by the photocatalyst}}$$

or alternatively

$$QY_{2H} = \frac{2 \text{ moles of } H^{\bullet}}{\text{moles of photons absorbed by the photocatalyst}}$$

and

$$QY_{H_2} = \frac{\text{moles of } H_2}{\text{moles of photons absorbed by the photocatalyst}}$$

2.5 Previous Works in the Reactor Photo-CREC Water II

There are already reported studies of hydrogen production using the Photo-CREC Water II Reactor, where TiO₂ was used as the photocatalyst and 1.00 % wt. Pt as the co-catalyst [25,26]. Ethanol was employed as sacrificial agents. The zero order, hydrogen production reached at pH=4 after 6 hours of irradiation, 0.30 micromole H₂/cm³ h. QYs in these studies yielded the encouraging levels of 8 %.

2.6 Scope of thesis

Given the above reviewed research progress and the state-of-the-art in photocatalysis, it is found that there is a need for research and development in photocatalysis, specifically in the area of hydrogen production via water dissociation as follows:

- a) New mesoporous semiconductors should be implemented via synthesis methods allowing modification of semiconductor 's morphology, particle size and particle size distribution, crystalline phase, composition and light absorption efficiency.
- b) These TiO₂ mesoporous supports should be engineered based on a soft-templating synthesis strategy, with a significant increase of anatase content and highly dispersed Pt co-catalyst.
- c) These mesoporous semiconductors should be demonstrated for hydrogen production via water dissociation under near-UV irradiation and using environmentally friendly scavenger such as ethanol at low concentrations (i.e. 1.00-2.00 wt. %)
- d) These mesoporous semiconductors should be tested using most advanced photocatalytic reactors, the case of Photo-CREC-Water II Reactor, where high anticipated QYs are rigorously established and demonstrated.

2.7 References

- [1] Satyapal, S. (2017, October 4). The Unique Potential of Hydrogen in Energy Infrastructure, Storage and Resiliency. Office of Energy Efficiency and Renewable Energy, Department of Energy U.S.A. <http://newscenter.lbl.gov/2017/10/06/reimagining-hydrogen-small-molecule-large-scale-ideas/>
- [2] Wu MM, Shen Y, Gu F, Xie YA, Zhang JC, Wang LJ. Preparation and photoelectric properties of mesoporous ZnO films. *Journal of Sol-Gel Science and Technology* 2010;53(2) 470-474.
- [3] Xiong XH, Wang ZX, Wu FX, Li XH, Guo HJ. Preparation of TiO₂ from ilmenite using sulfuric acid decomposition of the titania residue combined with separation of Fe³⁺ with EDTA during hydrolysis. *Advanced Powder Technology* 2013;24(1) 60-67.
- [4] El-Hazek N, Lasheen TA, El-Sheikh R, Zaki SA. Hydrometallurgical criteria for TiO₂ leaching from Rosetta ilmenite by hydrochloric acid. *Hydrometallurgy* 2007;87(1-2) 45-50.
- [5] Fujishima A, Honda K. Electrochemical photolysis of water at semiconductor electrode. *Nature* 1972(238) 37-38.
- [6] He LF, Wang CD, Yao XL, Ma RG, Wang HK, Chen PR, et al. Synthesis of carbon nanotube/mesoporous TiO₂ coaxial nanocables with enhanced lithium ion battery performance. *Carbon* 2014;75 345-352.
- [7] Hu LY, Wang JY, Zhang JX, Zhang QY, Liu ZH. An N-doped anatase/rutile TiO₂ hybrid from low-temperature direct nitridization: enhanced photoactivity under UV-/visible-light. *Rsc Advances* 2014;4(1) 420-427.

- [8] Lan X, Wang LZ, Zhang BY, Tian BZ, Zhang JL. Preparation of lanthanum and boron co-doped TiO₂ by modified sol-gel method and study their photocatalytic activity. *Catalysis Today* 2014;224 163-170.
- [9] Liu GQ, Liu LC, Song JR, Liang JD, Luo QZ, Wang DS. Visible light photocatalytic activity of TiO₂ nanoparticles hybridized by conjugated derivative of polybutadiene. *Superlattices and Microstructures* 2014;69 164-174.
- [10] Neubert S, Ramakrishnan A, Strunk J, Shi HY, Mei B, Wang LD, et al. Surface-Modified TiO₂ Photocatalysts Prepared by a Photosynthetic Route: Mechanism, Enhancement, and Limits. *Chempluschem* 2014;79(1) 163-170.
- [11] A. E. H. Machado, A. O. T. Patrocínio, M. D. França, L. M. Santos, K. A. Borges, L. F. Paula. Metal oxides for photoinduced hydrogen production and dye-sensitized solar cell applications. In: Méndez-Vilas A. (ed.) *Materials and processes for energy: communicating current research and technological developments*. Badajoz: Formatex; 2013. 867-879.
- [12] A. E. H. Machado, L. M. Santos, K. A. Borges, P. S. Batista, V. A. B. Paiva, P. S. Müller Jr., et al. Potential Applications for Solar Photocatalysis: From Environmental Remediation to Energy Conversion. In: Babatunde E. B. (ed.) *Solar Radiation*. Rijeka: InTech; 2012. 339-378.
- [13] F. Sordello, V. Maurino, C. Minero. Improved photochemistry of TiO₂ inverse opals and some examples. In: Saha S (ed.) *Molecular Photochemistry-Variou s Aspects*. Rijeka: InTech; 2012. 63-87.
- [14] M. Valenzuela. Photocatalytic deposition of metal oxides on semiconductor particles: a review. In: Saha S (ed.) *Molecular Photochemistry-Variou s Aspects*. Rijeka: InTech; 2012. 25-41.

- [15] Jaroenworarluck A, Pijarn N, Kosachan N, Stevens R. Nanocomposite TiO₂-SiO₂ gel for UV absorption. *Chemical Engineering Journal* 2012;181 45-55.
- [16] Affam AC, Chaudhuri M. Degradation of pesticides chlorpyrifos, cypermethrin and chlorothalonil in aqueous solution by TiO₂ photocatalysis *Journal of Environmental Management* 2013;130 160-165.
- [17] Hirakawa T, Sato K, Komano A, Kishi S, Nishimoto CK, Mera N. Specific properties on TiO₂ photocatalysis to decompose isopropyl methylphosphonofluoridate and dimethyl methylphosphonate in Gas Phase. *Journal of Photochemistry and Photobiology a-Chemistry* 2013;264 12-17.
- [18] Chen JW, Shi JW, Wang X, Ai HY, Cui HJ, Fu ML. Hybrid metal oxides quantum dots/TiO₂ block composites: Facile synthesis and photocatalysis application. *Powder Technology* 2013;246 108 116.
- [19] A. Eremenko, N. Smirnova, I. Gnatiuk, O. Linnik, N. Vityuk, Y. Mukha. Silver and gold nanoparticles on sol-gel TiO₂, ZrO₂, SiO₂ surfaces: optical spectra, photocatalytic activity, bactericide properties. In: Cuppoletti J (ed.) *Nanocomposites and Polymers with Analytical Methods*. Rijeka: InTech; 2011. 51-83.
- [20] V. S. Viteri, E. Fuentes. Titanium and Titanium Alloys as Biomaterials. In: Gegner J (ed.) *Tribology-Fundamentals and Advancements*. Rijeka: InTech; 2013. 155-181.
- [21] Grcic I, Vujevic D, Zizek K, Koprivanac N. Treatment of organic pollutants in water using TiO₂ powders: photocatalysis versus sonocatalysis. *Reaction Kinetics Mechanisms and Catalysis* 2013;109(2) 335-354.
- [22] Machado AEH, França MD, Velani V, Magnino GA, Velani HMM, Freitas FS. Characterization and evaluation of the efficiency of TiO₂/zinc phthalocyanine nano- Solar

- Radiation Applications composites as photocatalysts for wastewater treatment using solar irradiation. *International Journal of Photoenergy* 2008; 2008.
- [23] Fujishima A, Honda K. Electrochemical Photolysis of Water at a Semiconductor Electrode. *Nature* 1972;238(5358) 37
- [24] Gao P, Sun DD. Hierarchical sulfonated graphene oxide-TiO₂ composites for highly efficient hydrogen production with a wide pH range. *Applied Catalysis B-Environmental* 2014;147 888-896.
- [25] Escobedo-Salas, S.; Serrano-Rosales B., de Lasa, H. Quantum Yield with Platinum Modified TiO₂ Photocatalyst for Hydrogen Production. *Applied Catalysis-B; Environmental*. 2013; 140 523-536.
- [26] Escobedo, S.; Serrano, B.; Calzada, A.; Moreira, J.; de Lasa, H. Hydrogen production using a platinum modified TiO₂ photocatalyst and an organic scavenger. *Kinetic modeling. Fuel*; 2016; 181 438-449.
- [27] Guayaquil-Sosa, J.F.; Serrano-Rosales, B.; Valadés-Pelayo, P.J.; de Lasa, H. Photocatalytic hydrogen production using mesoporous TiO₂ doped with Pt. *Applied Catalysis-B; Environmental*. 2017; 211 337-348.
- [28] Guayaquil-Sosa, J.F.; Calzada, A.; Serrano, B.; Escobedo, S.; de Lasa, H. Hydrogen Production via Water Dissociation Using Pt-TiO₂ Photocatalysts: An Oxidation-Reduction Network. *Catalysts*; 2017; 7 324.
- [29] Hagfeldt A., Gratzel M. Light-Induced Redox Reactions in Nanocrystalline Systems. *Chemical Reviews* 1995;9549-68.
- [30] Hagfeldt A, Gratzel M. Molecular photovoltaics. *Accounts Chemistry Reserarch* 2000(33) 269-277.

- [31] Peter LM. Dye-sensitized nanocrystalline solar cells. *Physical Chemistry Chemical Physics* 2007;9 2630-2642.
- [32] Fujishima A, Honda K. Electrochemical Photolysis of Water at a Semiconductor Electrode. *Nature* 1972;238(5358) 37-+. DOI: 10.1038/238037a0.
- [33] Melian E.P, Suarez MN, Jardiel T, Rodriguez JMD, Caballero AC, Arana J, et al. Influence of nickel in the hydrogen production activity of TiO₂. *Applied Catalysis B-Environmental* 2014;152 192-201. DOI: 10.1016/j.apcatb.2014.01.039.
- [34] Mendez J.A.O., Lopez C.R., Melian E.P., Diaz OG, Rodriguez J.M.D, Hevia D.F., et al. Production of hydrogen by water photo-splitting over commercial and synthesised Au/TiO₂ catalysts. *Applied Catalysis B-Environmental* 2014;147 439-452. DOI: 10.1016/j.apcatb.2013.09.029.
- [35] Paula LF, Amaral RC, Iha NYM, Paniago RM, Machado AEH, Patrocinio AOT. New layer-by-layer Nb₂O₅-TiO₂ film as an effective underlayer in dye-sensitised solar cells. *RSC Advances* 2014;4(20) 10310-10316.
- [36] Kudo A. and Miseki Y. Heterogeneous photocatalyst materials for water splitting. *Chem. Soc. Rev.*, 2009;(8), 253–278
- [37] Kumar N, Maitra U, Hegde VI, Waghmare UV, Sundaresan A, Rao CNR. Synthesis, Characterization, Photocatalysis, and Varied Properties of TiO₂ Co-substituted with Nitrogen and Fluorine. *Inorganic Chemistry* 2013;52(18) 10512-10519.
- [38] Gupta SK, Singh J, Anbalagan K, Kothari P, Bhatia RR, Mishra PK. Synthesis, phase to phase deposition and characterization of rutile nanocrystalline titanium dioxide (TiO₂) thin films. *Applied Surface Science* 2013;264 737-742.

- [39] Ji YF, Zhou L, Ferronato C, Salvador A, Yang X, Chovelon JM. Degradation of sunscreen agent 2-phenylbenzimidazole-5-sulfonic acid by TiO₂ photocatalysis: Kinetics, photoproducts and comparison to structurally related compounds. *Applied Catalysis B-Environmental* 2013;140 457-467.
- [40] Kim DS, Kwak SY. The hydrothermal synthesis of mesoporous TiO₂ with high crystallinity, thermal stability, large surface area, and enhanced photocatalytic activity. *Applied Catalysis a General* 2007;323 110-118.
- [41] Hidalgo D, Messina R, Sacco A, Manfredi D, Vankova S, Garrone E. Thick mesoporous TiO₂ films through a sol-gel method involving a non-ionic surfactant: Characterization and enhanced performance for water photo-electrolysis. *International Journal of Hydrogen Energy* 2014.
- [42] Sanchez-Quiles D, Tovar-Sanchez A. Sunscreens as a source of hydrogen peroxide production in coastal waters. *Environmental Science & Technology* 2014;48(16) 9037-9042.
- [43] Xi BJ, Chu XN, Hu JY, Bhatia CS, Danner AJ, Yang H. Preparation of Ag/TiO₂/SiO₂ films via photo-assisted deposition and adsorptive self-assembly for catalytic bactericidal application. *Applied Surface Science* 2014;311 582-592.
- [44] Yeh SW, Ko HH, Chiang HM, Chen YL, Lee JH, Wen CM. Characteristics and properties of a novel in situ method of synthesizing mesoporous TiO₂ nanopowders by a simple coprecipitation process without adding surfactant. *Journal of Alloys and Compounds* 2014;613 107-116.
- [45] Wang ZY, Yao N, Hu X. Single material TiO₂ double layers antireflection coating with photocatalytic property prepared by magnetron sputtering technique. *Vacuum* 2014;108 20-26.

- [46] Zhaoyong Wang, Ning Yao, Xing Hu, Xinwei Shi, Structural and photocatalytic study of titanium dioxide films deposited by DC sputtering, In *Materials Science in Semiconductor Processing*. 2014;21 91-97.
- [47] Chen KC, Wang YH. The effects of Fe-Mn oxide and TiO₂/alpha-Al₂O₃ on the formation of disinfection by-products in catalytic ozonation. *Chemical Engineering Journal* 2014;253 84-92.
- [48] A. Oliveira, E. M. Saggiaro, T. Pavesi, J. C. Moreira, L. F. V. Ferreira. Solar photochemistry for environmental remediation-advanced oxidation processes for industrial wastewater treatment. In: Saha S (ed.) *Molecular Photochemistry-Variou Aspects*. Rijeka: InTech; 2012. 195-223.
- [49] Wu MM, Shen Y, Gu F, Xie YA, Zhang JC, Wang LJ. Preparation and photoelectric properties of mesoporous ZnO films. *Journal of Sol-Gel Science and Technology* 2010;53(2) 470-474.
- [50] Xiong XH, Wang ZX, Wu FX, Li XH, Guo HJ. Preparation of TiO₂ from ilmenite using sulfuric acid decomposition of the titania residue combined with separation of Fe³⁺ with EDTA during hydrolysis. *Advanced Powder Technology* 2013;24(1) 60-67.
- [51] Sasikumar C, Rao DS, Srikanth S, Ravikumar B, Mukhopadhyay NK, Mehrotra SP. Effect of mechanical activation on the kinetics of sulfuric acid leaching of beach sand ilmenite from Orissa, India. *Hydrometallurgy* 2004;75(1-4) 189-204.
- [52] El-Hazek N, Lasheen TA, El-Sheikh R, Zaki SA. Hydrometallurgical criteria for TiO₂ leaching from Rosetta ilmenite by hydrochloric acid. *Hydrometallurgy* 2007;87(1-2) 45-50.
- [53] Sanchez-Quiles D, Tovar-Sanchez A. Sunscreens as a source of hydrogen peroxide production in coastal waters. *Environmental Science & Technology* 2014;48(16) 9037-9042.

- [54] Hu LY, Wang JY, Zhang JX, Zhang QY, Liu ZH. An N-doped anatase/rutile TiO₂ hybrid from low-temperature direct nitridization: enhanced photoactivity under UV-/visible-light. *RSC Advances* 2014;4(1) 420-427.
- [55] Machado AEH, França MD, Velani V, Magnino GA, Velani HMM, Freitas FS. Characterization and evaluation of the efficiency of TiO₂/zinc phthalocyanine nano-Solar Radiation Applications.
- [56] Gao P, Sun DD. Hierarchical sulfonated graphene oxide-TiO₂ composites for highly efficient hydrogen production with a wide pH range. *Applied Catalysis B-Environmental* 2014;147 888-896.
- [57] Melian EP, Suarez MN, Jardiel T, Rodriguez JMD, Caballero AC, Arana J. Influence of nickel in the hydrogen production activity of TiO₂. *Applied Catalysis B-Environmental* 2014;152 192-201. DOI: 10.1016/j.apcatb.2014.01.039.
- [58] Mendez JAO, Lopez CR, Melian EP, Diaz OG, Rodriguez JMD, Hevia DF. Production of hydrogen by water photo-splitting over commercial and synthesised Au/TiO₂ catalysts. *Applied Catalysis B-Environmental* 2014;147 439-452.
- [59] Taboada E, Angurell I, Llorca J. Dynamic photocatalytic hydrogen production from ethanol-water mixtures in an optical fiber honeycomb reactor loaded with Au/TiO₂. *Journal of Catalysis* 2014;309 460-467.
- [60] Wu ZF, Zhang WH, Xiong F, Yuan Q, Jin YK, Yang JL. Active hydrogen species on TiO₂ for photocatalytic H₂ production. *Physical Chemistry Chemical Physics* 2014;16(15) 7051-7057.

- [61] Idigoras J, Berger T, Anta JA. Modification of Mesoporous TiO₂ Films by Electrochemical Doping: Impact on Photoelectrocatalytic and Photovoltaic Performance. *Journal of Physical Chemistry C* 2013;117(4) 1561-1570.
- [62] Higashijima S, Miura H, Fujita T, Kubota Y, Funabiki K, Yoshida T. Highly efficient new indoline dye having strong electron-withdrawing group for zinc oxide dye-sensitized solar cell. *Tetrahedron* 2011;67(43) 8421-8421.
- [63] Jayaweera PVV, Perera AGU, Tennakone K. Why Gratzel's cells works so well. *Inorganica Chimica Acta* 2008(361) 707-711.
- [64] Park SH, Roy A, Beaupré S, Cho S, Coates N, Moon JS. Bulk heterojunction solar cells with internal quantum efficiency approaching 100%. *Nature Photonics* 2009;3 297-302.
- [65] Gratzel M. Solar energy conversion by dye-sensitized photovoltaic cells. *Inorganic Chemistry* 2005;44(20) 6841-6851.
- [66] O'Regan B, Grätzel M. A Low-Cost, High-Efficiency Solar-Cell Based on Dye-Sensitized Colloidal TiO₂ Films. *Nature* 1991;353(6346) 737-740.
- [67] Gratzel M. Photoelectrochemical cells. *Nature* 2001;414(6861) 338-344.
- [68] Chiba Y, Islam A, Watanabe Y, Komiya R, Koide N, Han LY. Dye-sensitized solar cells with conversion efficiency of 11.1%. *Japanese Journal of Applied Physics, Part 2: Letters & Express Letters* 2006;45(24-28).
- [69] Kroon JM, Bakker NJ, Smit HJP, Liska P, Thampi KR, Wang P. Nanocrystalline dye-sensitized solar cells having maximum performance. *Progress in Photovoltaics* 2007;15(1) 1-18.

- [70] Kalyanasundaram K, Gratzel M. Applications of functionalized transition metal complexes in photonic and optoelectronic devices. *Coordination Chemistry Reviews* 1998;177 347-414.
- [71] Davis ME. Ordered porous materials for emerging applications. *Nature* 2002;417(6891) 813-821.
- [72] Zheng XL, Kuang Q, Yan KY, Qiu YC, Qiu JH, Yang SH. Mesoporous TiO₂ Single Crystals: Facile Shape-, Size-, and Phase-Controlled Growth and Efficient Photocatalytic Performance. *Applied Materials & Interfaces* 2013;5(21) 11249-11257.
- [73] Kim DS, Han SJ, Kwak SY. Synthesis and photocatalytic activity of mesoporous TiO₂ with the surface area, crystallite size, and pore size. *Journal of Colloid and Interface Science* 2007;316(1) 85-91.
- [74] Blin JL, Stebe MJ, Roques-Carnes T. Use of ordered mesoporous titania with semicrystalline framework as photocatalyst. *Colloids and Surfaces a-Physicochemical and Engineering Aspects* 2012;407 177-185.
- [75] Li W, Wu ZX, Wang JX, Elzatahry AA, Zhao DY. A Perspective on Mesoporous TiO₂ Materials. *Chemistry of Materials* 2014;26(1) 287-298.
- [76] Crossland EJW, Noel N, Sivaram V, Leijtens T, Alexander-Webber JA, Snaith HJ. Mesoporous TiO₂ single crystals delivering enhanced mobility and optoelectronic device performance. *Nature* 2013;495(7440) 215-219. DOI: 10.1038/Nature11936.
- [77] Herrero C, Quaranta A, Leibl W, Rutherford AW, Aukauloo A. Artificial photosynthetic systems. Using light and water to provide electrons and protons for the synthesis of a fuel. *Energy & Environmental Science* 2011;4(7) 2353-2365.

- [78] Lee ES, Lee KM, Yoon SI, Ko YG, Shin DH. Influence of CNT incorporation on the photovoltaic behavior of TiO₂ films formed by high-voltage electrophoretic deposition. *Current Applied Physics* 2013;13 526-529.
- [79] Kondo JN, Domen K. Crystallization of mesoporous metal oxides. *Chemistry of Materials* 2008;20(3) 835-847.
- [80] Ferreira OP, Alves OL, Macedo JD, Gimenez ID, Barreto LS. Ecomaterials: Development and application of functional porous materials for environmental protection. *Química Nova* 2007;30(2) 464-467.
- [81] Guo SY, Han S, Chi B, Pu J, Li J. Synthesis of shape-controlled mesoporous titanium phosphate nanocrystals: The hexagonal titanium phosphate with enhanced hydrogen generation from water splitting. *International Journal of Hydrogen Energy* 2014;39(6) 2446-2453.
- [82] Kao LH, Hsu TC, Cheng KK. Novel synthesis of high-surface-area ordered mesoporous TiO₂ with anatase framework for photocatalytic applications. *Journal of Colloid and Interface Science* 2010;341(2) 359-365.
- [83] Yang H, Coombs N, Sokolov I, Ozin GA. Free-standing and oriented mesoporous silica films grown at the air-water interface. *Nature* 1996;381(6583) 589-592. DOI: 10.1038/381589a0.
- [84] Li W, Wu ZX, Wang JX, Elzatahry AA, Zhao DY. A Perspective on Mesoporous TiO₂ Materials. *Chemistry of Materials* 2014;26(1) 287-298.
- [85] Kandiel TA, Ivanova I, Bahnemann DW. Long-term investigation of the photocatalytic hydrogen production on platinized TiO₂: an isotopic study. *Energy & Environmental Science* 2014;7(4) 1420-1425.

- [86] Rungjaroentawon N, Onsuratoom S, Chavadej S. Hydrogen production from water splitting under visible light irradiation using sensitized mesoporous-assembled TiO₂-Applications of Mesoporous Ordered Semiconductor Materials — Case Study of TiO₂-SiO₂ mixed oxide photocatalysts. *International Journal of Hydrogen Energy* 2012;37(15) 11061-11071.
- [87] Taffa DH, Kathiresan M, Arnold T, Walder L, Erbacher M, Bauer D. Dye sensitized membranes within mesoporous TiO₂ Photocurrents in aqueous solution. *Journal of Photochemistry and Photobiology a-Chemistry* 2010;216(1) 35-43.
- [88] Tan HQ, Zhao Z, Niu M, Mao CY, Cao DP, Cheng DJ. A facile and versatile method for preparation of colored TiO₂ with enhanced solar-driven photocatalytic activity. *Nanoscale* 2014;6(17) 10216-10223.
- [89] Zhang RY, Elzatahry AA, Al-Deyab SS, Zhao DY. Mesoporous titania: From synthesis to application. *Nano Today* 2012;7(4) 344-366.
- [90] Zhou XF, Lu J, Jiang JJ, Li XB, Lu MN, Yuan GT. Simple fabrication of N-doped mesoporous TiO₂ nanorods with the enhanced visible light photocatalytic activity. *Nanoscale Research Letters* 2014;9 DOI: 10.1186/1556-276x-9-34.
- [91] Pal N, Bhaumik A. Soft templating strategies for the synthesis of mesoporous materials: Inorganic, organic-inorganic hybrid and purely organic solids. *Advances in Colloid and Interface Science* 2013;189 21-41.
- [92] Abdel-Azim SM, Aboul-Gheit AK, Ahmed SM, El-Desouki DS, Abdel-Mottaleb MSA. Preparation and Application of Mesoporous Nanotitania Photocatalysts Using Different Templates and pH Media. *International Journal of Photoenergy* 2014;2014.

- [93] Song HJ, Chen T, Sun YL, Zhang XQ, Jia XH. Controlled synthesis of porous flowerlike TiO₂ nanostructure with enhanced photocatalytic activity. *Ceramics International* 2014;40(7) 11015-11022.
- [94] Patrocínio A. O. T., El-Bachá A. S., Paniago E. B., Paniago R. M., and Murakami Iha N. Y., Influence of the Sol-Gel pH Process and Compact Film on the Efficiency of -Based Dye-Sensitized Solar Cells. *International Journal of Photoenergy*, 2012;2012 (7) doi:10.1155/2012/638571
- [95] Kim DS, Kwak SY. The hydrothermal synthesis of mesoporous TiO₂ with high crystallinity, thermal stability, large surface area, and enhanced photocatalytic activity. *Applied Catalysis A-General* 2007;323 110-118.
- [96] Niederberger M, Garnweitner G, Buha J, Polleux J, Ba JH, Pinna N. Non-aqueous synthesis of metal oxide nanoparticles: Review and indium oxide as case study for the dependence of particle morphology on precursors and solvents. *Journal of Sol-Gel Science and Technology* 2006;40(2-3) 259-266.
- [97] Ribeiro C, Malagutti, A. R., Mendonça, V. R. E Mourão, A. J. L. Nanostructures in Photocatalysis: A review on strategies of photocatalysts' synthesis for nanometric scale. *Química Nova* 2009;32(8).
- [98] Muniz EC, Goes MS, Silva JJ, Varela JA, Joanni E, Parra R. Synthesis and characterization of mesoporous TiO₂ nanostructured films prepared by a modified sol-gel method for application in dye solar cells. *Ceramics International* 2011;37(3) 1017-1024.
- [99] Yang XH, Fu HT, Yu AB, Jiang XC. Large-surface mesoporous TiO₂ nanoparticles: Synthesis, growth and photocatalytic performance. *Journal of Colloid and Interface Science* 2012;38 774-783.

- [100] Mahoney L, Koodali RT. Versatility of evaporation-induced self-assembly (EISA) method for preparation of mesoporous TiO₂ for energy and environmental applications. *Materials* 2014;7(4) 2697-2746.
- [101] Arconada N, Castro Y, Duran A, Hequet V. Photocatalytic oxidation of methyl ethyl ketones over sol-gel mesoporous and meso-structured TiO₂ films obtained by EISA method. *Applied Catalysis B-Environmental* 2011;107(1-2) 52-58.
- [102] Ouyang J, Li XY, Jin J, Yang HM, Tang AD. Surface status and reduction behavior of porous ceria (CeO₂) via amended EISA method. *Journal of Alloys and Compounds* 2014;606 236-241.
- [103] Beck, J.S.; Calabro, D.C.; McCullen, S.B.; Pelrine, B.P.; Schmitt, K.D.; Vartuli, J.C. Method for Functionalizing Synthetic Mesoporous Crystalline Material. U.S. Patent 2,069,722, 27 May 1992.
- [104] Badawy MI, Ghaly MY, Ali MEM. Photocatalytic hydrogen production over nanostructured mesoporous titania from olive mill wastewater. *Desalination* 2011;267(2-3) 250-255.
- [105] Bian YR, Wang XH, Hu ZY. Synthesis of mesoporous titania thin films by a simple route at low-temperature via plasma treatment. *Journal of Materials Science* 2013;48(11) 4088-4096.
- [106] Zhou W, Li W, Wang JQ, Qu Y, Yang Y, Xie Y. Ordered Mesoporous Black TiO₂ as Highly Efficient Hydrogen Evolution Photocatalyst. *Journal of the American Chemical Society* 2014;136(26) 9280-9283.
- [107] Xiang P, Li X, Wang H, Liu GH, Shu T, Zhou ZM. Mesoporous nitrogen-doped TiO₂ sphere applied for quasi-solid-state dye-sensitized solar cell. *Nanoscale Research Letters* 2011;6.

- [108] Wu ZY, Tao YF, Lin Z, Liu L, Fan XX, Wang Y. Hydrothermal Synthesis and Morphological Evolution of Mesoporous Titania-Silica. *Journal of Physical Chemistry C* 2009;113(47) 20335-20348.
- [109] Wen ZH, Wu W, Liu Z, Zhang H, Li JH, Chen JH. Ultrahigh-efficiency photocatalysts based on mesoporous Pt-WO₃ nanohybrids. *Physical Chemistry Chemical Physics* 2013;15(18) 6773-6778.
- [110] Wang YZ, Zhu SP, Chen XR, Tang YG, Jiang YF, Peng ZG. One-step template free fabrication of mesoporous ZnO/TiO₂ hollow microspheres with enhanced photocatalytic activity. *Applied Surface Science* 2014;307 263-271.
- [111] Shamaila S, Khan A, Sajjad L, Chen F, Zhang JL. Mesoporous titania with high crystallinity during synthesis by dual template system as an efficient photocatalyst. *Catalysis Today* 2011;175(1) 568-575.
- [112] Antonelli DM, Ying JY. Synthesis of Hexagonally Packed Mesoporous TiO₂ by a Modified Sol-Gel Method. *Angewandte Chemie-International Edition in English* 1995;34(18) 2014-2017.
- [113] Joo JB, Lee I, Dahl M, Moon GD, Zaera F, Yin YD. Controllable Synthesis of Mesoporous TiO₂ Hollow Shells: Toward an Efficient Photocatalyst. *Advanced Functional Materials* 2013;23(34) 4246-4254.
- [114] Lopez A, Acosta D, Martinez AI, Santiago J. Nanostructured low crystallized titanium dioxide thin films with good photocatalytic activity. *Powder Technology* 2010;202(1-3) 111-117.
- [115] Ramasamy E, Jo C, Anthonysamy A, Jeong I, Kim JK, Lee J. Soft-template simple synthesis of ordered mesoporous titanium nitride-carbon nanocomposite for high

performance dye-sensitized solar cell counter electrodes. *Chemistry of Materials* 2012;24(9) 1575-1582.

- [116] Tran TH, Nosaka AY, Nosaka Y. Adsorption and decomposition of a dipeptide in TiO₂ photocatalytic systems. *Journal of Photochemistry and Photobiology a-Chemistry* 2007;192(2-3) 105-113.
- [117] Lu YF, Fan HY, Stump A, Ward TL, Rieker T, Brinker CJ. Aerosol-assisted self-assembly of mesostructured spherical nanoparticles. *Nature* 1999;398(6724) 223-226.
- [118] Yang H, Coombs N, Sokolov I, Ozin GA. Free-standing and oriented mesoporous silica films grown at the air-water interface. *Nature* 1996;381(6583) 589-592.
- [119] Gao J, Li HR, Rong H, Dai YH. Large pore nanocrystalline TiO₂ films for quasi-solid state dye-sensitized solar cells. *Nanotechnology and Precision Engineering, Pts 1 and 2* 2013;662 177-181.
- [120] Wang Y, Jiang ZH, Yang FJ. Preparation and photocatalytic activity of mesoporous TiO₂ derived from hydrolysis condensation with TX-100 as template. *Materials Science and Engineering B-Solid State Materials for Advanced Technology* 2006;128(1-3) 229-233.
- [121] Rodriguez-Abreu C, Vilanova N, Solans C, Ujihara M, Imae T, Lopez-Quintela A. A combination of hard and soft templating for the fabrication of silica hollow microcoils with nanostructured walls. *Nanoscale Research Letters* 2011;6.
- [122] Hu CY, Xu YJ, Duo SW, Li WK, Xiang JH, Li MS. Preparation of Inorganic Hollow Spheres Based on Different Methods. *Journal of the Chinese Chemical Society* 2010;57(5A) 1091-1098.

- [123] Tang H, Zhang D, Tang GG, Ji XR, Li CS, Yan XH. Low temperature synthesis and photocatalytic properties of mesoporous TiO₂ Nano spheres. *Journal of Alloys and Compounds* 2014;591 52-57.
- [124] Chen JF, Hua ZJ, Yan YS, Zakhidov AA, Baughman RH, Xu LB. Template synthesis of ordered arrays of mesoporous titania spheres. *Chemical Communications* 2010;46(11) 1872-1874.
- [125] Ibrahim, H.; de Lasa, H. Photo-catalytic degradation of air borne pollutants. Apparent quantum efficiencies in a novel photo-CREC-air reactor. *Chem. Eng. Sci.* 58 (2003) 943-949.
- [126] de Lasa, H.; Serrano, B.; Salaices, M. *Photocatalytic Reaction Engineering*, First Ed., Springer: New York, 2005.
- [127] Cassano, A., Martin, C., Brandi, R., and Alfano, Photoreactor analysis and design: Fundamentals and applications, *Ind. and Eng. Chem. Res.*, 34 (1995) 2155-2201.
- [128] Davydov, L., Srairiotis, G., and Pratsinis, E., Novel differential reactor for the measurement of overall quantum yields, *Ind. and Eng. Chem. Res.*, 38 (1999) 1375-1383.
- [129] Peil, N., and Hoffmann, M., Development and optimization of a TiO₂ coated fiber optic cable reactor: Photocatalytic degradation of 4-chlorophenol, *Environ. Sci. and Tech.* 29 (1995) 2974-2981.
- [130] Valladares, J., and Bolton, J., A method for the determination of quantum yields in heterogeneous systems: The titanium dioxide photocatalyzed bleaching of methylene blue. *Trace Metals in the Environment*, 3 (1993) 111-120.
- [131] Yamazaki-Nishida, S., Read, H., Nagano, J., Jarosch, T., Eddy, C., Cervera-March, S.,

and Anderson, M., Gas phase photocatalytic degradation on TiO₂ pellets of volatile chlorinated compounds from a soil vapor extraction well. *J. Soil Contam.*, 3 (1994) 363–378.

[132] Fox, M. and Dulay, M., Heterogeneous photocatalysis, *Chem. Rev.*, 93 (1993) 341–357.

[133] Nimlos, M., Jacoby, W., Blake, D., and Milne T., Direct mass spectrometric studies of the destruction of hazardous wastes. 2. Gas phase photocatalytic oxidation of trichloroethylene over TiO₂: Products and mechanisms, *Environ. Sci. and Tech.*, 27 (1993) 732–740.

[134] Sczechowski, J., Koval, C., and Noble, R., A Taylor vortex reactor for heterogeneous photocatalysis, *Chem. Eng. Sci.*, 50 (1995) 3163–3173.

[135] Zhang, Y., Crittenden, J., and Hand, D., 1994a, The solar photocatalytic decontamination of water, *Chem. and Ind.*, 18 (1994) 714–717.

[136] Garcia Hernandez J.M., Serrano Rosales B. and de Lasa Hugo, The photochemical thermodynamic efficiency factor (PTEF) in photocatalytic reactors for air treatment, *In Chemical Engineering Journal*, 165 (2010) 891-901.

Chapter 3

3 Synthesis of Mesoporous Pt Doped TiO₂ with Block Copolymers Pluronic P123 and Pluronic F127 as Templates for Photocatalytic Hydrogen Generation.

3.1 Introduction

Titanium dioxide (TiO₂) has outstanding optical, semiconductor and chemical properties. Due to this, in the near future, TiO₂ is expected to play an increasingly significant role in photocatalysis, chemical sensors, electrochromic devices, solar cells and in other fields. TiO₂ can be directly used as a photocatalyst under ultraviolet irradiation. In this case, the photons from the light source interact with the TiO₂ making possible the elimination of organic pollutants in air and in water and contributing to hydrogen generation.

Among current synthesis methods, the sol-gel method is very suitable to produce nanomaterials. This method can be implemented under ambient conditions and does not require complex configurations and synthesis procedures. The sol-gel synthesis is based on the hydrolysis/condensation of a titanium precursor to produce a sol and then a gel. After solvent evaporation, a xerogel is obtained, which is milled and heat treated to produce a highly crystalline TiO₂ mesoporous material. It is important to state that titanium dioxide with a mesoporous structure has gained great interest in recent years, due to its large surface area, as well as its higher adsorption capacity and higher catalytic activity than the more conventional non-porous TiO₂ [1-7].

It is well known that by increasing the available specific surface area of a TiO₂ photocatalyst, one can promote the adsorption and diffusion of reactants which leads to an enhanced photocatalytic performance. To increase the active surface area, pore formers are usually added to the sol-gel synthesis. As discussed in Chapter 2, hard- and soft-templating syntheses have been widely reported in the literature to produce porous arrays. In fact, hard-templates are attractive because a high degree of self-organization can be obtained. This can be done, for instance, with inverse opals by using templating nanoparticles (i.e., silica or polystyrene particles) [8-10].

Nevertheless, the hard-template technique requires the synthesis of nanoparticles which is not cost effective. Instead, the soft-template synthesis using polymers is relatively simple and does not require the complex synthesis used in the hard-template procedure. In the soft-template synthesis, a polymeric precursor is added to the sol. The porosity is created by removing the polymeric chains using high temperature annealing to form mesoporous anatase or rutile particles. Hence, as reported in the literature, polymeric precursors have been employed to increase the photocatalytic activity of TiO₂ nanoparticles. These are: P123 and F127. P123 or similar non-ionic surfactants, display low periodicity (ordering) of the pores. In this regard, improvements in pore ordering have been achieved using these non-ionic surfactants.

The templates in the syntheses of mesoporous TiO₂ can be anionic surfactants, cationic surfactants or non-ionic surfactants. These templates have strong electrostatic interactions between ionic surfactants and inorganic species. Calcinations at high temperatures are needed to remove the templates. However, this process can result in a collapse of the pore structure. Both the block copolymers P123 and F127 have been used as templates for the syntheses of mesoporous silica and titania. Due to the small binding force between the inorganic species and the general non-ionic surfactants, it is still challenging to produce ordered mesoporous TiO₂.

In the synthesis of mesoporous TiO₂, when using P123 and F127, a low acidity tends to form anatase, whereas a high acidity forms rutile phases. Citric acid functionalizes the surface of the hydrophilic titania nanoparticles and enhances the binding of these particles to the ethylene oxide units of F127. P123 and F127 molecules bind to the surface of titania nanoparticles and prevent collapse of pores. They also prevent the transformation of anatase to rutile, despite the use of calcination temperatures as high as 700 °C.

In this chapter, the ordered and pure TiO₂ mesoporous materials were synthesized by sol-gel method using P123 and F127 as templates. The influence of the various factors on the syntheses of the ordered mesoporous catalysts are discussed in detail.

3.2 Experimental

The triblock co-polymer surfactants, *poly(ethylene oxide)-poly(propylene oxide)-poly(ethylene oxide)*, $(-\text{CH}_2\text{CH}_2\text{O}-)_{106}(\text{CH}_2(\text{CH}_3)\text{CHO})_{70}(-\text{CH}_2\text{CH}_2\text{O}-)_{106}$, (Pluronic F127, $M_{\text{AVG}} = 12600$, Sigma Aldrich) and $(-\text{CH}_2\text{CH}_2\text{O}-)_{20}(\text{CH}_2(\text{CH}_3)\text{CHO})_{70}(-\text{CH}_2\text{CH}_2\text{O}-)_{20}$ (Pluronic P123, $M_{\text{AVG}} = 5800$, Sigma Aldrich) were used as soft-templates. These soft-templates help in the sol-gel synthesis method, directing the structure reagents in the mesoporous TiO_2 synthesis. Hydrochloric acid of 37% purity, citric acid and titanium (IV) isopropoxide ($\text{Ti}(\text{OC}_3\text{H}_7)_4$, Sigma Aldrich), were employed as co-reactants.

For the synthesis of mesoporous TiO_2 , 400 mL of ethanol ($\text{CH}_3\text{CH}_2\text{OH}$) from Commercial Alcohols company were acidified using 33.00 g of hydrochloric acid (37 wt. % purity, Sigma Aldrich). After combining these reagents, 20.00 g of Pluronic F127 or Pluronic P123 were added, and the suspension was mixed until dissolution (0.5 h). Then, 6.30 g of citric acid were incorporated under intense stirring. Following this procedure, the solution pH was adjusted to 0.75. Mixing continued at ambient temperature for 1 h. Once this step was completed, 28.50 g of titanium (IV) isopropoxide were added into the mixture dropwise. The resultant liquid phase, displaying a sol-gel appearance, was mixed for 24 h. The resulting sol-gel phases were evaporated and calcined by gradually increasing the temperature, from room temperature up to the target temperature (i.e., 773 K (500°C), 873 K (600°C) and 973 K (700°C)). As soon as the desired thermal level was achieved, this temperature was kept under ambient air for 6 h to calcine the sample and combust the organic template.

Mesoporous TiO_2 was doped with Pt as a co-catalyst for water dissociation. A titanium (IV) isopropoxide template method was modified with hexachloroplatinic acid hydrate (Sigma Aldrich $\text{H}_2\text{PtCl}_6 \cdot x\text{H}_2\text{O}$, 99.9% purity). Titanium (IV) isopropoxide was added to the sol-gel, concurrently with the Pt containing species.

3.3 Characterization

Three photocatalyst characterization techniques were employed in this study: (a) Specific Surface Area determined using a Micromeritics, ASAP 2010 unit, through nitrogen

adsorption; (b) X-Ray Diffraction (XRD) developed by using a diffractometer RIGAKU Ultima IV and a multi-purpose diffractometer; and (c) Scanning Electron Microscopy (SEM) analyses which were carried out using a Hitachi S-4500 Field Emission SEM Instrument with a Quartz PCI X One SSD X-Ray Analyzer. The mesoporous TiO₂ were dispersed using sonication in methanol, with platinum oxide glass used as the conductive substrate during SEM analyses.

3.3.1 N₂ Adsorption-Desorption Isotherms

Specific surface areas were calculated using the Brunauer–Emmett–Teller (BET) method while the pore volume distributions were measured with the Barrett–Joyner–Halenda (BJH) model. Nitrogen adsorption was carried out at 77.8 K using a 3 Flex 3.02 Analyzer Model from Micromeritics. The materials were degassed at 300 °C for 6 h. Nitrogen adsorption covered the 10⁻⁸ to 1 relative partial pressure range. Pore size distributions were calculated using the BJH method [10]. The pore diameter distribution was established using the N₂ isotherm data for each material as reported in Table 3.1.

Figure 3.1 to 3.8 report both adsorption and desorption isotherms of type V for the synthesized mesoporous TiO₂ using Pluronic P123 and Pluronic F127, and calcined at 500 °C, 600 °C and 700 °C.

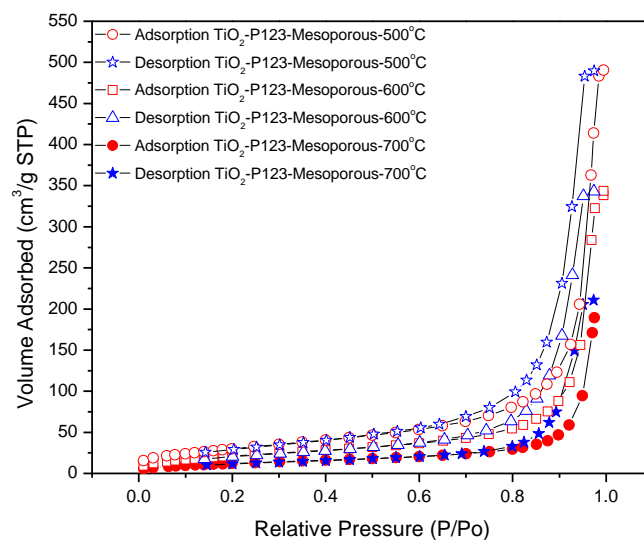


Figure 3.1 N₂ Adsorption-Desorption Isotherms for the Synthesized Mesoporous TiO₂ Using Pluronic P123, Calcined at 500 °C, 600 °C and 700 °C.

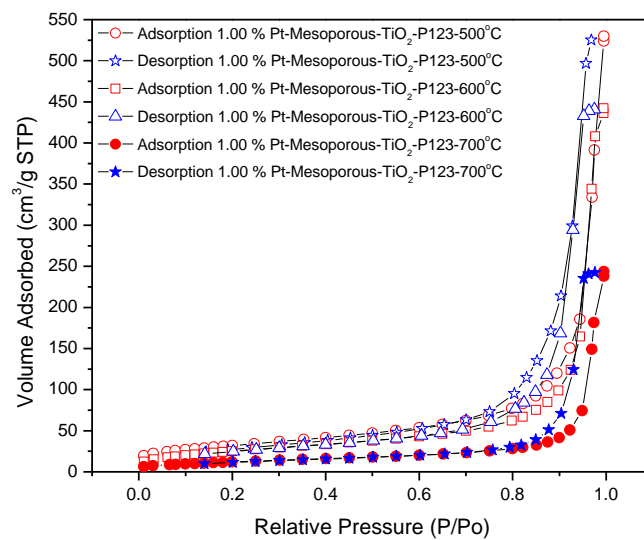


Figure 3.2 N₂ Adsorption-Desorption Isotherms for the Synthesized Mesoporous TiO₂ Using Pluronic P123 and Doped with 1.00 % wt. Pt, calcined at 500 °C, 600 °C and 700 °C.

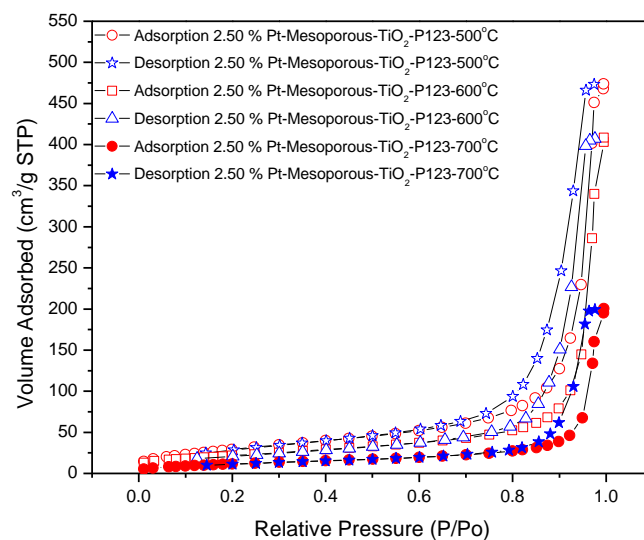


Figure 3.3 N₂ Adsorption-Desorption Isotherms for the Synthesized Mesoporous TiO₂ Using Pluronic P123 and Doped with 2.50 % wt. Pt, Calcined at 500 °C, 600 °C and 700 °C.

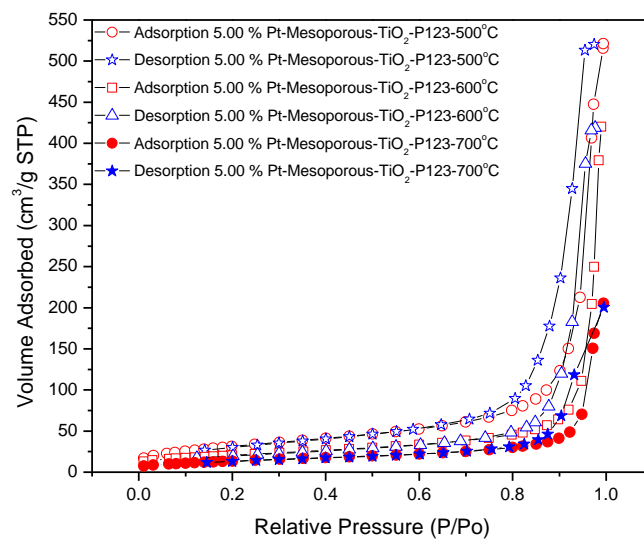


Figure 3.4 N₂ Adsorption-Desorption Isotherms for the Synthesized Mesoporous TiO₂ Using Pluronic P123 and Doped with 5.00 % wt. Pt, calcined at 500 °C, 600 °C and 700 °C.

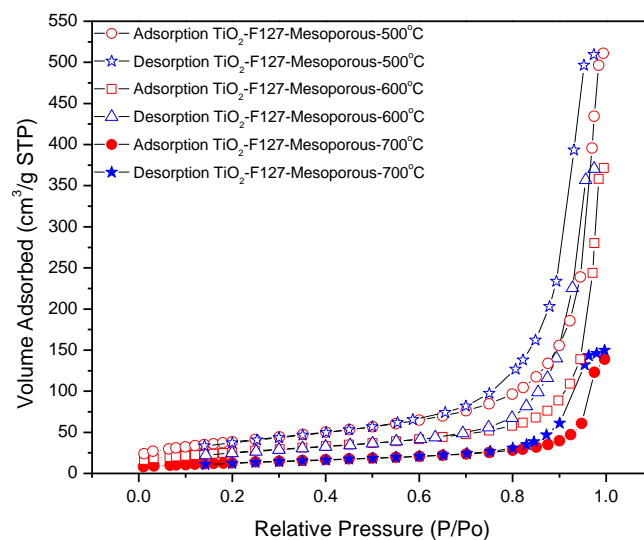


Figure 3.5 N₂ Adsorption-Desorption Isotherms for the Synthesized Mesoporous TiO₂ Using Pluronic F127, Calcined at 500 °C, 600 °C and 700 °C.

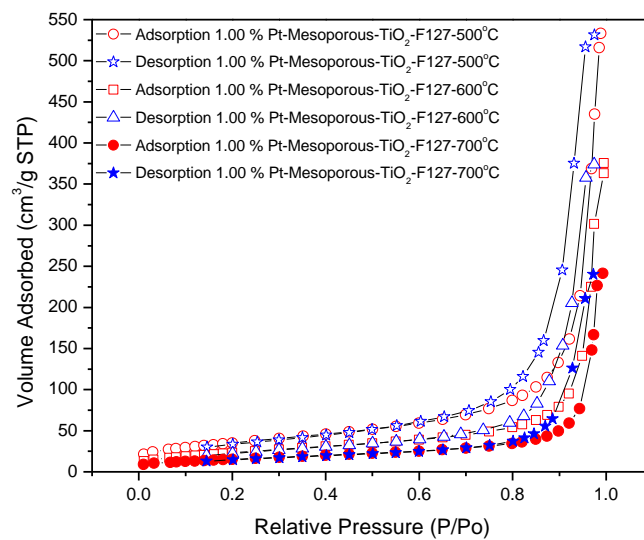


Figure 3.6 N₂ Adsorption-Desorption Isotherms for the Synthesized Mesoporous TiO₂ Using Pluronic F127 and Doped with 1.00 % wt. Pt, calcined at 500 °C, 600 °C and 700 °C.

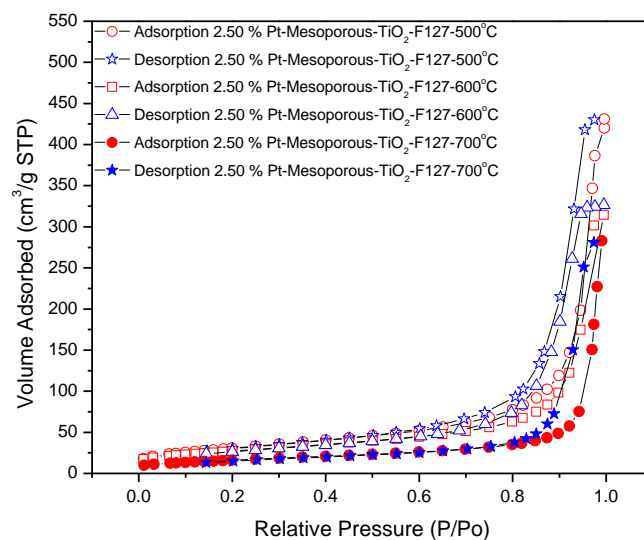


Figure 3.7 N₂ Adsorption-Desorption Isotherms for the Synthesized Mesoporous TiO₂ Using Pluronic F127 and Doped with 2.50 % wt. Pt, calcined at 500 °C, 600 °C and 700 °C.

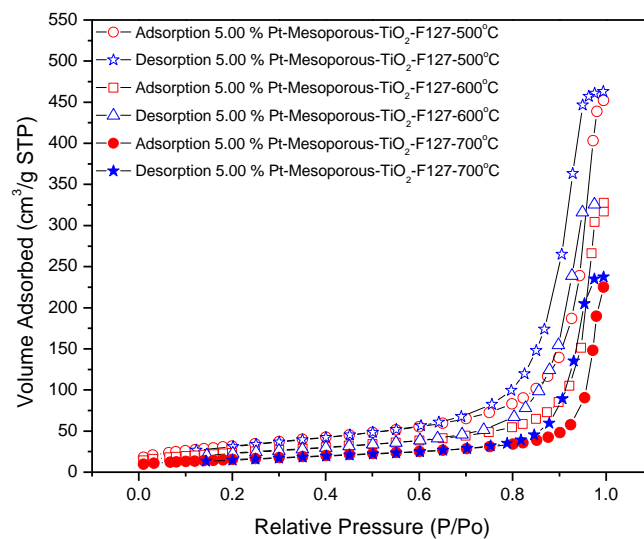


Figure 3.8 N₂ Adsorption-Desorption Isotherms for the Synthesized Mesoporous TiO₂ Using Pluronic F127 and Doped with 5.00 % wt. Platinum Loading, Calcined at 500 °C, 600 °C and 700 °C.

Table 3.1 summarizes the calculated specific surface areas, pore volumes and average pore diameters. One can notice that the calcinations at 500°C, which the lowest calcination temperature employed, allowed one to preserve the largest specific surface area. As a result, the mesoporous materials calcined at 500°C, and synthesized with both P123 and F127, were selected for further hydrogen formation via water dissociation studies.

Table 3.1 Textural Properties of the Synthesized Mesoporous TiO₂ with Pluronic P123 and Pluronic F127 added.

Photocatalyst	Calcination Temperature (°C)	Directing-Structure Template	Platinum Loading % (wt.)	S _{BET} (m ² g ⁻¹)	V _p ^{BJH} (cm ³ g ⁻¹)
Meso-TiO ₂	500	P123	0	113	0.56
	600			81	0.44
	700			46	0.26
1.00 wt. % Pt / Meso-TiO ₂	500	P123	1.00	116	0.52
	600			96	0.53
	700			45	0.23
2.50 wt. % Pt / Meso-TiO ₂	500	P123	2.50	110	0.62
	600			78	0.44
	700			44	0.21
5.00 wt. % Pt / Meso-TiO ₂	500	P123	5.00	116	0.63
	600			74	0.31
	700			50	0.23
Meso-TiO ₂	500	F127	0	160	0.69
	600			92	0.37
	700			47	0.19
1.00 wt. % Pt / Meso-TiO ₂	500	F127	1.00	138	0.59
	600			86	0.35
	700			56	0.23
	500	F127	2.50	142	0.64
	600			98	0.49

2.50 wt. % Pt / Meso-TiO ₂	700			59	0.24
5.00 wt. % Pt / Meso-TiO ₂	500	F127	5.00	127	0.61
	600			85	0.41
	700			56	0.23

3.3.2 XRD Diffractograms

XRD analyses were developed by using Cu as an anode material, and by utilizing Ni filtered CuK α radiation ($\lambda = 0.15406$ nm) in an Ultima IV X-Ray Diffractometer from Rigaku. The XRD analyses were recorded in the 20° to 80° range of the 2 θ degrees scale.

Figure 3.9 to Figure 3.12 report the XRD diffractograms for the synthesized mesoporous TiO₂ materials prepared by sol-gel method using PluronicP123, as a directing structure reagent. When reviewing the XRD diffractograms, one can recognize the characteristic peaks of the crystalline anatase phase of titanium dioxide, with platinum included as a dopant material.

In this respect, one can notice that all photocatalysts show the anatase (101) crystal plane given the characteristic 27° Bragg angle band in the 2 θ degrees scale. On the other hand, and as an interesting observation, the various sol-gel Pt–TiO₂ photocatalysts showed recordable 27° Bragg angles. Hence, this demonstrates that the various synthesized sol-gel Pt–TiO₂ catalysts using Pluronic P123 are free of a rutile as revealed by the absence of the rutile (110) facet plane.

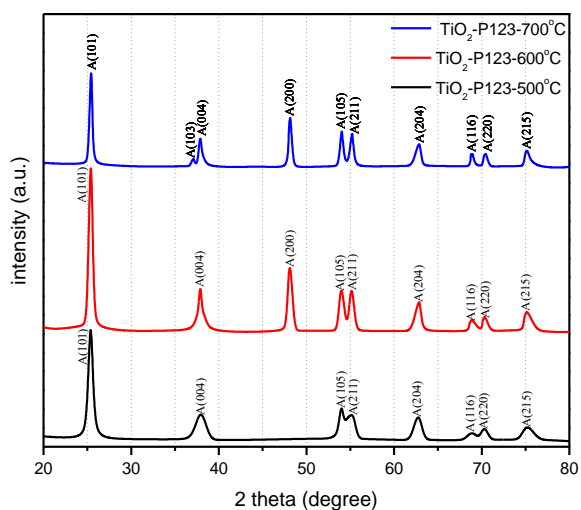


Figure 3.9 XRD Diffractograms of the Synthesized Mesoporous TiO₂ Using Pluronic P123, Calcined at 500 °C, 600 °C and 700 °C. XRD diffractograms were overlapped for comparison. (A) represents TiO₂ in the anatase phase.

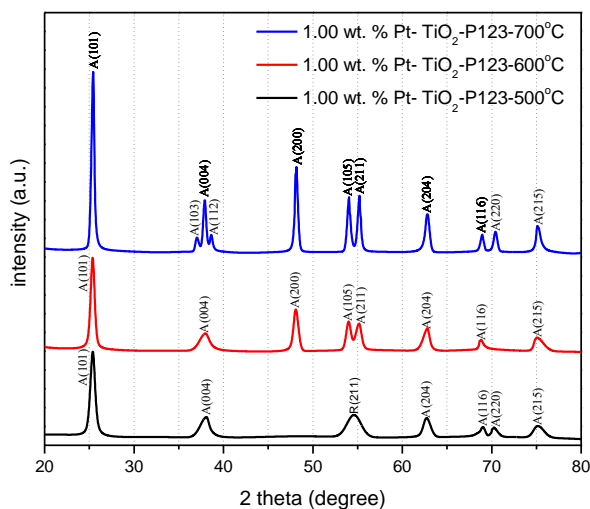


Figure 3.10 XRD Diffractograms of the Synthesized Mesoporous TiO₂ Using Pluronic P123 with 1.00 % wt Pt, Calcined at 500 °C, 600 °C and 700 °C. XRD diffractograms were overlapped for comparison. (A) represents TiO₂ in the anatase phase and (R) indicates TiO₂ in the rutile phase.

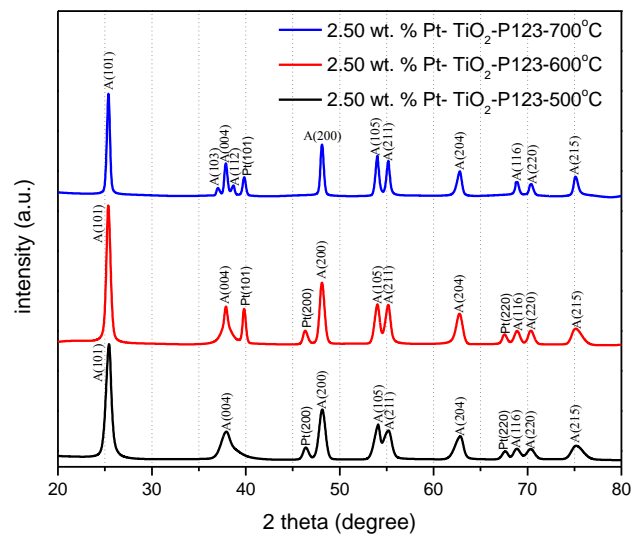


Figure 3.11 XRD Diffractograms of the Synthesized Mesoporous TiO₂ Using Pluronic P123, with 2.50 % wt. Pt, calcined at 500 °C, 600 °C and 700 °C. XRD diffractograms were overlapped for comparison. (A) represents TiO₂ in the anatase phase.

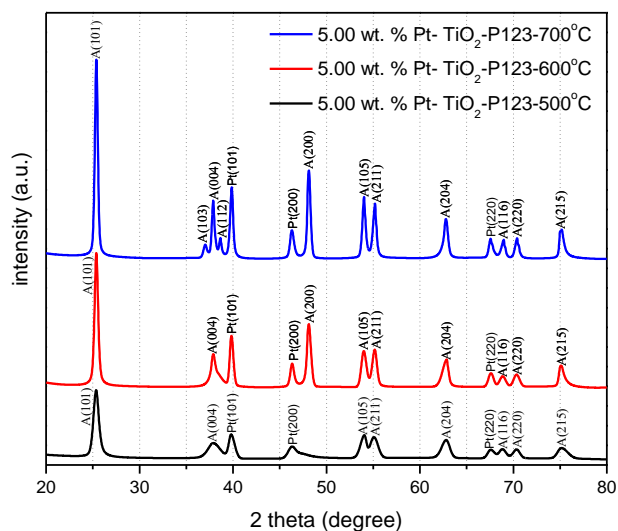


Figure 3.12 XRD Diffractograms of the Synthesized Mesoporous TiO₂ Using Pluronic P123, with 5.00 % wt. Pt, calcined at 500 °C, 600 °C and 700 °C. XRD diffractograms were overlapped for comparison. (A) represents TiO₂ in the anatase phase.

Furthermore, XRD diffractograms as reported in Figure 3.13 to Figure 3.15, were obtained for the synthesized mesoporous TiO₂ materials prepared by sol-gel method using Pluronic F127, as a structure directing agent. One can distinguish in the XRD diffractogram, the characteristic anatase titanium dioxide phase peaks as well as the platinum added as dopant.

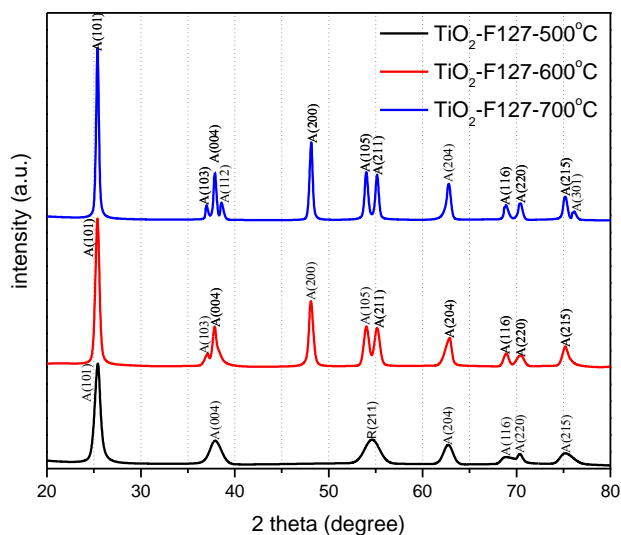


Figure 3.13 XRD Diffractograms of the Synthesized Mesoporous TiO₂ Using Pluronic F127, Calcined at 500 °C, 600 °C and 700 °C. XRD diffractograms were overlapped for comparison. (A) represents TiO₂ in the anatase phase and (R) indicates TiO₂ in the rutile phase.

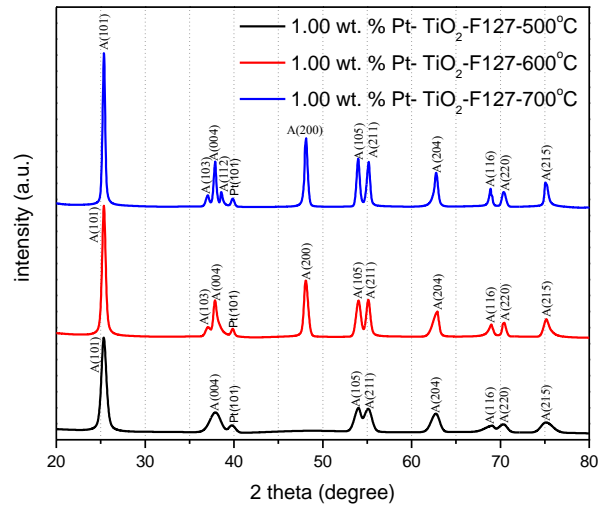


Figure 3.14 XRD Diffractograms of the Synthesized Mesoporous TiO₂ Using Pluronic F127 and Doped with 1.00 % wt Pt, calcined at 500 °C, 600 °C and 700 °C. XRD diffractograms were overlapped for comparison. (A) represents TiO₂ in the anatase phase.

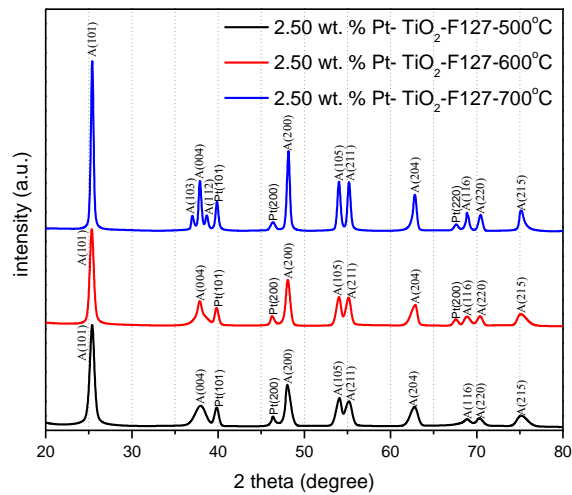


Figure 3.15 XRD Diffractograms of the Synthesized Mesoporous TiO₂ Using Pluronic F127 and Doped with 2.50 % wt Pt, calcined at 500 °C, 600 °C and 700 °C. XRD diffractograms were overlapped for comparison. (A) represents TiO₂ in the anatase phase and (R) indicates TiO₂ in the rutile phase.

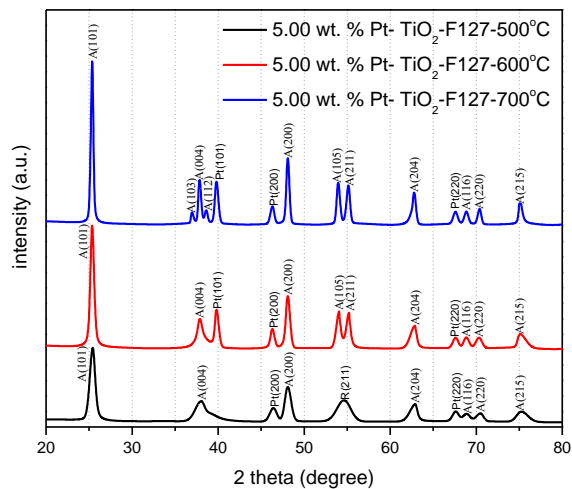


Figure 3.16 XRD Diffractograms of the Synthesized Mesoporous TiO₂ using Pluronic F127 and Doped with 5.00 % wt Pt, calcined at 500 °C, 600 °C and 700 °C. XRD diffractograms were overlapped for comparison. (A) represents TiO₂ in the anatase phase and (R) indicates TiO₂ in the rutile phase.

Figure 3.13 shows that for the TiO₂ mesoporous photocatalyst synthesized with Pluronic F127, there is no rutile (110) crystal plane at the characteristic 27° Bragg angle band in the 2θ scale. As can also be observed, and as reported in Figures 3.14 to 3.16, with the sol-gel synthesized Pt–TiO₂ using PluronicF127, there is no detectable 27° Bragg angle. Thus, this confirms that the several synthesized sol-gel Pt–TiO₂ using Pluronic F127 are free of a rutile (110) facet.

3.3.3 Scanning Electron Microscopy (SEM)

SEM micrographs, of the synthesized mesoporous TiO₂ photocatalysts, using both Pluronic P123 and F127, with different Pt loadings and calcined at 500 °C, are reported in Figure 3.22 to 3.22.

One can notice that the Pt-TiO₂ powders, synthesized with both Pluronic P123 and F127 and calcined at 500 °C, exhibit uniform crystallite sizes, with an average grain size assessed at 30nm. These close crystallite sizes may be assigned to the mild and favourable calcination temperature of 500°C, averting crystallite agglomeration.

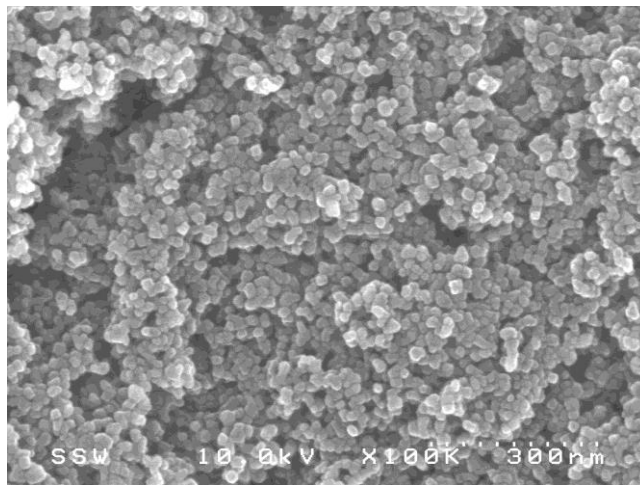


Figure 3.17 SEM Images of Mesoporous TiO₂ Photocatalysts Prepared Using Pluronic P123 at a 500°C Calcination Temperature.

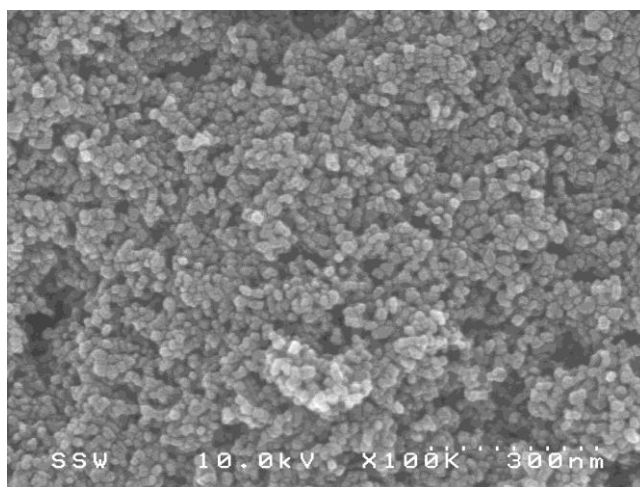


Figure 3.18 SEM Images of Mesoporous Pt-TiO₂ Photocatalysts Prepared Using Pluronic P123 with 1.00 % wt. Pt at a 500°C Calcination Temperature.

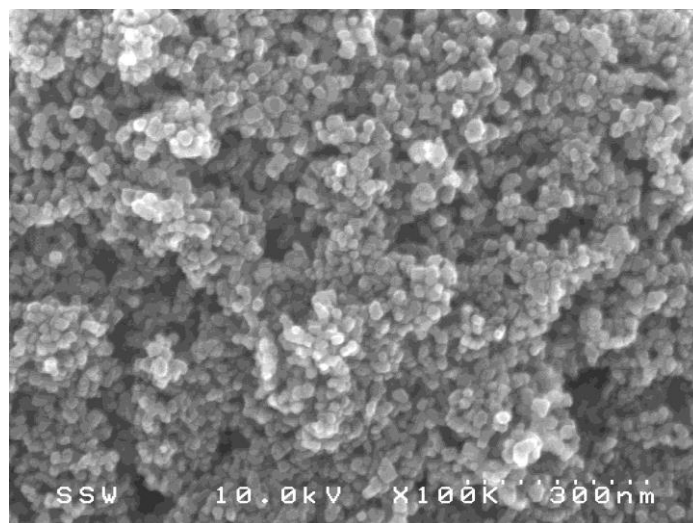


Figure 3.19 SEM Images of Mesoporous Pt–TiO₂ Photocatalysts Prepared Using Pluronic P123 with 2.50 % wt. Pt at a 500°C Calcination Temperature.

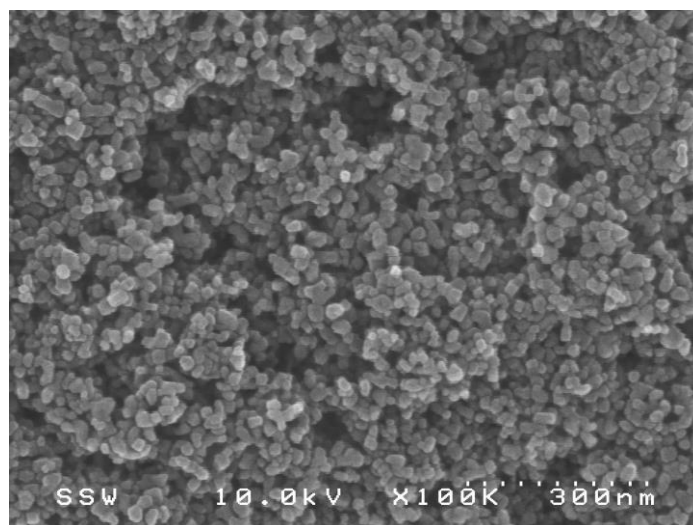


Figure 3.20 SEM Images of Mesoporous Pt–TiO₂ Photocatalysts Prepared Using Pluronic F127 at a 500°C Calcination Temperature.

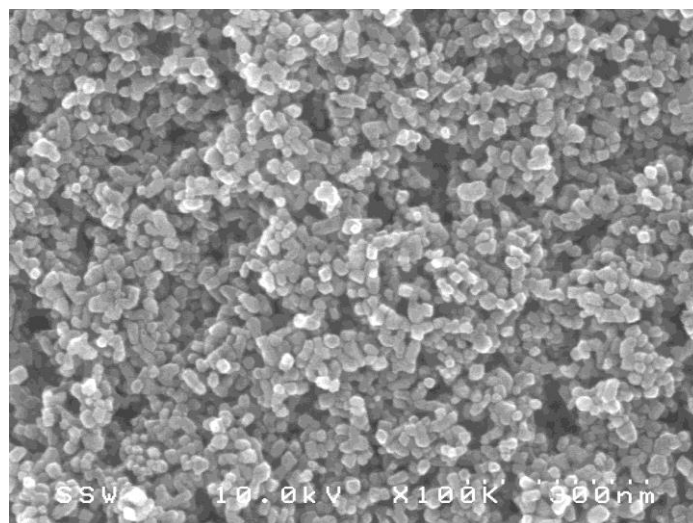


Figure 3.21 SEM Images of Mesoporous Pt–TiO₂ Photocatalysts Prepared Using Pluronic F127 with 1.00 % wt. Pt at a 500°C Calcination Temperature.

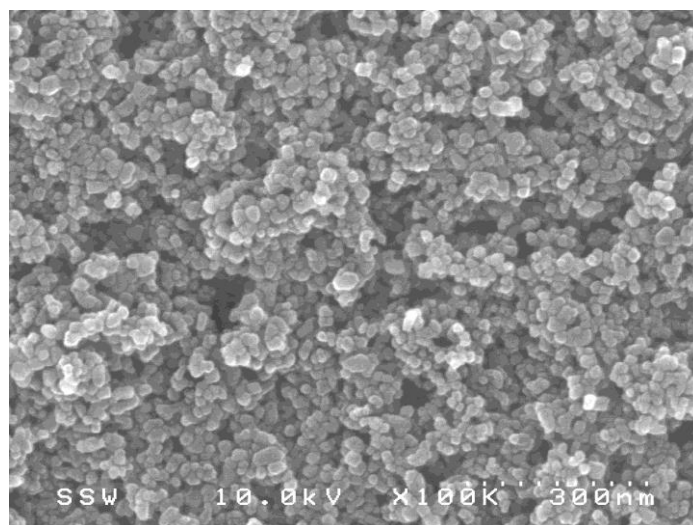


Figure 3.22 SEM Images of Mesoporous Pt–TiO₂ Photocatalysts Prepared Using Pluronic F127 with 2.50 % wt. Platinum Loading at a 500°C Calcination Temperature.

3.4 Photocatalytic Hydrogen Production via Water Dissociation using Mesoporous TiO₂

Experiments of hydrogen generation via photocatalytic water dissociation were carried out in a Photo-CREC-Water II Reactor. This unit was used with a specifically designed H₂ storage tank and a BLB lamp that permitted the entire use of the near-UV light irradiation spectrum with a main emission peak at 268 nm. Furthermore, 2.00 v/v% ethanol (EtOH) was utilized as a scavenger. The results of the photoactivity of a mesoporous semiconductor nanopowder of TiO₂, synthesized using Pluronic P123 and Pluronic 127, and doped with Pt, for photocatalytic hydrogen production, are presented in this section. In this respect, synthesized photocatalysts were studied for hydrogen production using different photocatalyst loadings under the above-mentioned photoreaction conditions.

Figures 3.23 to 3.25 report the increase of the cumulative hydrogen produced with irradiation time. In this case, the photocatalyst was synthesized with P123 and no Pt was added. The three photocatalysts considered were calcined at 500°C. Similar information for the photocatalyst calcined at 600°C and 700°C is reported in Appendix A. Given the more significant value of the mesoporous TiO₂ photocatalyst calcined at 500°C, only these data are reported in this Chapter.

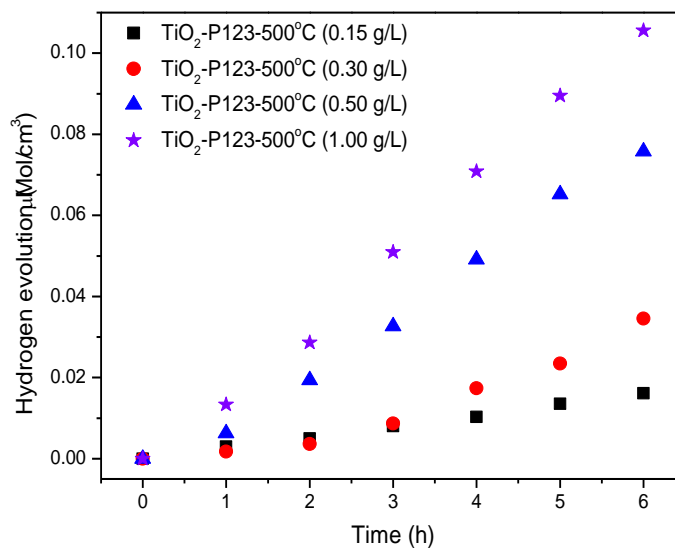


Figure 3.23 Changes of Cumulative Hydrogen Produced at Various Irradiation Times with Different Photocatalyst Loadings. Notes: a) Mesoporous TiO₂ synthesized using Pluronic P123 and calcined at 500 °C, b) Photocatalyst irradiated with a near-UV light of $\lambda=368$ nm, c) pH = 4.00 \pm 0.05, d) 2.00 % v/v ethanol scavenger. Standard deviation for repeats are \pm 6 %.

In this respect, one can notice for the three photocatalysts studied at various photocatalyst loadings, that there is a consistent zero order reaction for the hydrogen formation rate. One should note that the photocatalyst calcined at 500°C yielded the best formation rates for hydrogen production.

Figures 3.24 to 3.26 report the cumulative hydrogen production for photocatalysts synthesized with P123 and doped with 1.00 wt. %, 2.50 wt. % and 5.00 wt% of Pt.

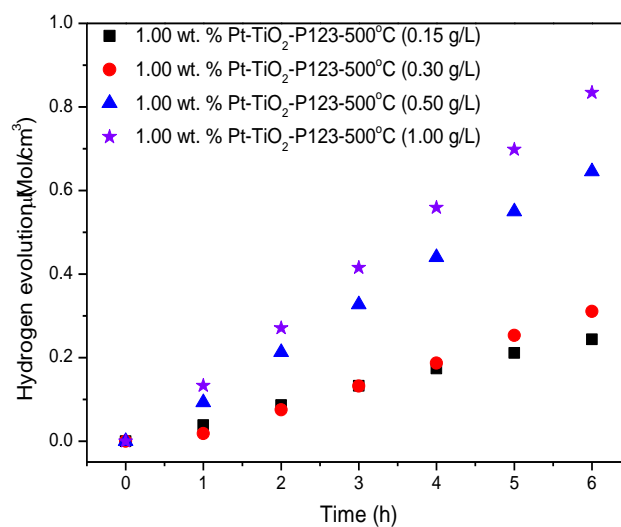


Figure 3.24 Changes of Cumulative Hydrogen Produced at Various Irradiation Times and with Different Photocatalyst Loadings. Notes: a) Mesoporous TiO₂ synthesized using Pluronic P123, doped with 1.00 wt% Pt and calcined at 500 °C, b) Photocatalyst irradiated with a UV light of $\lambda=368$ nm, c) pH = 4.00 \pm 0.05, d) 2.00 % v/v ethanol scavenger. Standard deviation for repeats \pm 6 %.

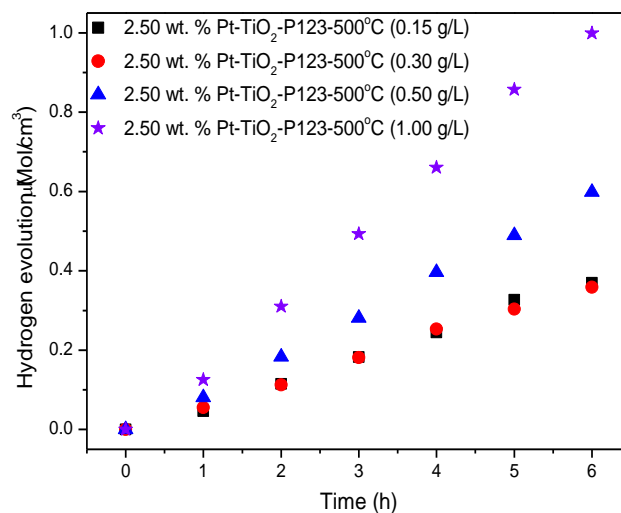


Figure 3.25 . Changes of Cumulative Hydrogen Produced at Various Irradiation Times with Different Photocatalyst Loadings. Note: a) Mesoporous TiO₂ synthesized using Pluronic P123, doped with 2.50 wt% Pt and calcined at 500 °C, b) Photocatalyst irradiated with a UV light of $\lambda=368$ nm, c) pH = 4.00 \pm 0.05 and d) 2.00 % v/v ethanol scavenger. Standard deviation for repeats \pm 6 %.

Figures 3.24 and 3.25 show: a) The significant enhancement of hydrogen production when using the Pt doped photocatalyst, which was synthesized employing the Pluronic P123 template, b) The consistent zero order formation rate for all the catalyst loadings studied. One can, for instance, notice that the cumulative hydrogen production after 6 hours of irradiation augments from 0.1 $\mu\text{Mole}/\text{cm}^3$ to 1 $\mu\text{Mole}/\text{cm}^3$, or about 10 times at the highest photocatalyst loading used of 1.00 g/L.

Furthermore, Figure 3.25 presents a similar analysis as in the previous sections but using the photocatalyst synthesized with Pluronic F127.

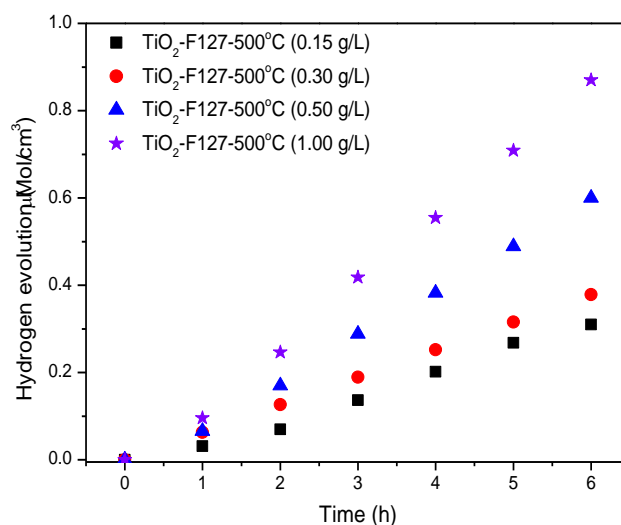


Figure 3.26 Changes of Cumulative Hydrogen Produced at Various Irradiation Times with Different Photocatalyst Loadings. Notes: a) Mesoporous TiO₂ synthesized using Pluronic F127, calcined at 500 °C b) Photocatalyst irradiated with a UV light of $\lambda=368$ nm, c) pH = 4.00 ± 0.05 , d) 2.00 % v/v ethanol scavenger. Standard deviation for repeats ± 7 %.

Figure 3.26 reports the change of template effect, from P123 (refer to Figure 2.23) to F127 in the synthesis of the photocatalyst. One can see that when F127 is used, the cumulative formation of hydrogen after 6 hours of irradiation and with a 1g/L photocatalyst loading, stays at $0.9 \mu\text{Mole}/\text{cm}^3$. This represents about 9 times the cumulative hydrogen produced with P-123. This valuable finding points to the critical importance of the TiO₂ architecture for H₂ production.

Furthermore, Figures 3.27 and 3.28 describe the cumulative H₂ production using 1.00 wt% and 2.50 wt% of Pt. These figures show that the efficiency of hydrogen formation when using TiO₂ synthesized with F127, can be further enhanced with Pt addition. In this case, the efficiency of hydrogen formation increases from $0.90 \mu\text{Mole}/\text{cm}^3$ up to $1.40 \mu\text{Mole}/\text{cm}^3$.

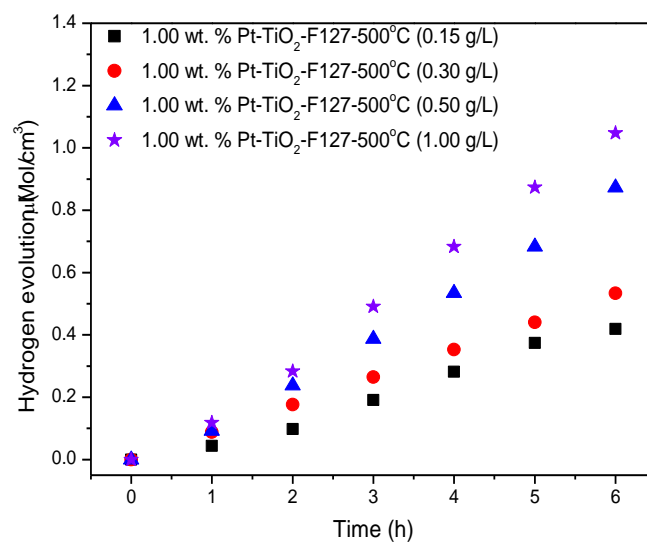


Figure 3.27 Changes of Cumulative Hydrogen Produced at Various Irradiation Times and with Different Photocatalyst Loadings. Notes: a) Mesoporous TiO₂ synthesized using Pluronic F127, doped with 1.00 wt. % and calcined at 500 °C b) Photocatalyst irradiated with a UV light of $\lambda=368$ nm) pH = 4.00 \pm 0.05 and d) 2.00 % v/v ethanol scavenger. Standard deviation for repeats \pm 7 %.

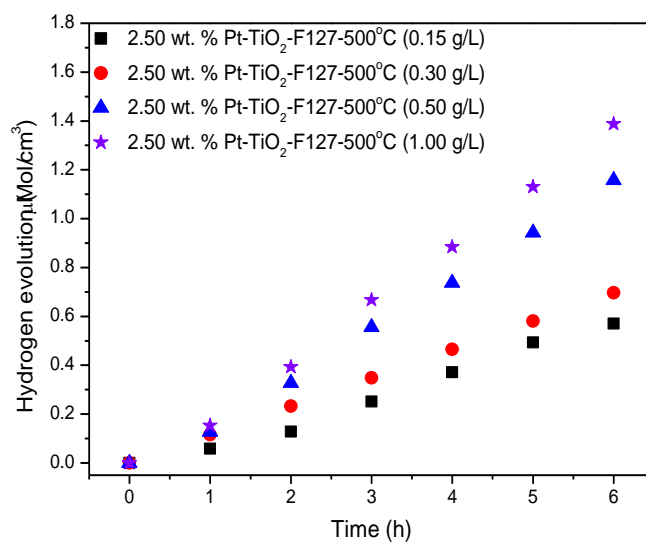


Figure 3.28 Changes of Cumulative Hydrogen Produced at Various Irradiation Times and with Different Photocatalyst Loadings. Notes: a) Mesoporous TiO₂ synthesized using Pluronic F127, doped with 2.50 wt% Pt and calcined at 500°C, b) Photocatalyst irradiated with a UV light of $\lambda=368$ nm, c) pH = 4.00 ± 0.05 , d) 2.00 % v/v ethanol scavenger. Standard deviation for repeats ± 7 %.

Supplementary photocatalytic hydrogen evolution for the rest of the synthesized semiconductors are presented in Appendix A.

In summary, it is shown via the experimental studies in the Photo-CREC-Water II Reactor that both the architecture of the synthesized TiO₂ and the Pt doping play a significant role in the production of hydrogen via water splitting.

3.5 Conclusions

The following are the significant conclusions of the present chapter:

- (a) Mesoporous TiO₂ photocatalysts were successfully synthesized using a Pluronic P123 template and a Pluronic F127 template.
- (b) The synthesized mesoporous TiO₂ were characterized using nitrogen adsorption, XRD diffraction and Scanning Electron Microscopy (SEM). The obtained nitrogen adsorption isotherms allowed one to calculate the specific surface area at the 150 cm²/g⁻¹ level, pore size of up to 40 nm.
- (c) XRD was particularly useful to identify the anatase and rutile crystalline phases in both the mesoporous TiO₂ and Pt-TiO₂ photocatalysts. Anatase was the dominant phase found in the synthesized mesoporous semiconductors.
- (d) Reactivity studies for hydrogen production demonstrate the major importance of both the mesoporous TiO₂ structure and the Pt loading. It is on this basis, and given the value of the mesoporous TiO₂ photocatalysts synthesized with Pluronic F127 up 10 times higher in photoactivity compared to the observed using Pluronic P-123, that further studies documented in Chapters 4 and 5 were developed.

3.6 References

- [1] Soler-Illia, G.J.A.A.; Sanchez, C.; Lebeau, B.; Patarin, J. Chemical strategies to design textured materials: From microporous and mesoporous oxides to nanonetworks and hierarchical structures. *Chem. Rev.* 2002, *102*, 4093–4138.
- [2] Wan, Y.; Zhao, D. On the controllable soft-templating approach to mesoporous silicates. *Chem. Rev.* 2007, *107*, 2821–2860.
- [3] Corma, A. From microporous to mesoporous molecular sieve materials and their use in catalysis. *Chem. Rev.* 1997, *97*, 2373–2420.
- [4] Corma, A. Preparation and catalytic properties of new mesoporous materials. *Top. Catal.* 1997, *4*, 249–260.
- [5] Sing, K.S.W.; Everett, D.H.; Haul, R.A.W.; Moscou, L.; Pierotti, R.A.; Rouquerol, J.; Siemieniewska, T. Reporting physisorption data for gas/solid systems with special reference to the determination of surface area and porosity. *Pure Appl. Chem.* 1985, *57*, 603–619.
- [6] Brinker, C.J. Evaporation-induced self-assembly: Functional nanostructures made easy. *MRS Bull.* 2004, *29*, 631–640.
- [7] Meynen, V.; Cool, P.; Vansant, E.F. Verified syntheses of mesoporous materials. *Microporous Mesoporous Mater.* 2009, *125*, 170–223.
- [8] Lee J, Han S, Hyeon T. Synthesis of new nanoporous carbon materials using nanostructured silica materials as templates. 2004, 478–486.
- [9] Zhang J, Zhou P, Liu J, Yu J. New understanding of the difference of photocatalytic activity among anatase, rutile and brookite TiO₂. *Phys Chem* 2014, *16*, 20382–20386.
- [10] Zhao XS, Su F, Yan Q. Templating methods for preparation of porous structures. *J Mater Chem.* 2006, *16*, 637.

Chapter 4

4 Photocatalytic Hydrogen Production Using Mesoporous TiO₂ Doped with Pt

The information presented in this chapter is based on the article entitled "Photocatalytic hydrogen production using mesoporous TiO₂ doped with Pt", published in Applied Catalysis B: Environmental Vol. 211 p. 337-348, in August 2017. The sections reported in this chapter contribute towards the fulfilment of the general objectives a) and b) of the PhD Dissertation as described in section 1.1.

4.1 Introduction

Currently, fossil energy resources are used extensively to satisfy most of the world's energy requirements. Projection of energy use and availability suggests that in the near future, there will be major issues and challenges to be faced with energy supply and demand. Additionally, combustion of fossil fuels leads to atmospheric emissions of carbon particles, CO₂ and noxious gases such as NO_x, SO_x. Thus, environmentally friendly fuels, that are both cost-effective and easily storable, are of great importance for the world's sustainable development [1].

Hydrogen is, in this respect, an ideal candidate as an energy vector [2]. Numerous technologies can be used to generate hydrogen. However, only a few of them can be considered as truly environmentally friendly. Steam hydrocarbon reforming is the current dominant technology for hydrogen production. It requires high temperatures (700–1100 °C) and emits large amounts of CO₂ [3]. Hence, efforts focused on water splitting are of great potential significance. Water splitting using solar energy is one of the most attractive approaches to produce hydrogen. Water splitting is an eco-friendly process that can be operated at ambient temperature and pressure. This process can take advantage from sunlight; an abundant and inexpensive renewable energy source [4,5,6].

The most important issue still to be addressed is the low quantum efficiency of photocatalytic materials in photocatalytic hydrogen production. This is related with restrictions in band gap excitation as well as recombination of charge carriers in

semiconductor photocatalysts. Thus, promoting too low hydrogen evolution rates, which up to date have limited the practical application of this technology on a large scale.

In photocatalytic water splitting, photons are absorbed by semiconductors, and as a result, water splits into hydrogen and oxygen. Nevertheless, water splitting is not thermodynamically favored. Current research focuses on increasing both the efficiency and stability of the materials [7,8]. This is essential to achieve the commercialization of this process [9,10].

Semiconductors are characterized by two types of mobile carriers: a) electrons in the conduction band and b) holes in the valence band. Both bands are separated by an energy gap. There is a continuous transition of electrons between bands. When a valence electron is given an energy equal or greater than the energy band gap, it is transferred to the conduction band, leading to a pair electron-hole formation. When an electron falls from the conduction band into the valence band, and into a hole, a recombination occurs.

Among the various semiconductors, TiO_2 has been extensively studied due to its photosensitivity, low cost, low toxicity, and good chemical and thermal stability. There are two main issues with TiO_2 . On one hand, TiO_2 can be activated mainly by near ultraviolet irradiation (near-UV) due to its wide band gap (3.20 eV for anatase and 3.00 eV for rutile), which limits its practical efficiency while using solar energy. In addition, near-UV radiation makes up only 4-5% of the solar spectrum, further reducing its potential applications. On the other hand, a high electron hole recombination reduces the photoelectric conversion efficiency of TiO_2 . This being one of the main limitations to the practical application of photocatalysis as a viable technology for solar light harvesting.

TiO_2 can be modified with CdS, ZnO, PbS, Cu_2O , Bi_2S_3 , and CdSe forming TiO_2 composites. Theoretically combining n-type TiO_2 with p-type semiconductors is effective in improving the photoelectric TiO_2 conversion efficiency. Many of these modified materials have received less attention due to, under illumination in contact with water, they can experience photocorrosion (*e.g.* Zn^{2+} or Cd^{2+} dissolution). A reliable alternative to improving photoelectric conversion is the addition of noble metals (*e.g.* Pt,

Au, Ag and Pd) during the semiconductor synthesis. Noble metals addition favors water splitting given the separation of photoproduced electron-hole pairs because: a) the surface plasmon resonance of noble metal particles can be excited by visible light, (b) the energy band gap is reduced, and c) the noble metal nanoparticles act as electron traps [45-47].

CREC-UWO research group developed a platinum modified TiO₂ photocatalyst [33-36]. Pt modified photocatalysts were evaluated in a Photo-CREC Water-II (PCWII) Reactor using 2% v/v ethanol water acidic solutions (pH = 4.00 ± 0.05) under near-UV light irradiation [36]. Low grade ethanol is a renewable carbon containing scavenger. Dissociated water and photon activated semiconductors yield H[•] and [•]OH. Pairs of H[•] radicals combine forming H₂, while the ethanol [•]OH scavenger forms CO₂, CH₄ and C₂H₆. Under oxygen-free conditions, Quantum Yields (QY) as high as 8 % were obtained. Hydrogen was produced in a stable process with no detectable photocatalyst deactivation.

4.2 Photocatalyst Engineering

A phenomenological approach for photocatalyst design for hydrogen production involves the followings: a) Semiconductor purity: the highest possible anatase content close to 100%. This appears to enhance under concurrent conversion of an ethanol scavengers, hydrogen production, b) Surface area of the mesoporous TiO₂: the highest possible. This can be accomplished with a mesoporous TiO₂ with a regular and nanometric pore sizes, c) Crystallite size: the smallest possible with Pt crystallites, consistent with the pore sizes and pore volume of the synthesized mesoporous TiO₂. This can lead to a nanometric Pt crystallites and high Pt metal dispersion.

4.3 Experimental Methods

4.3.1 Preparation of Mesoporous Titania Nanoparticles

The copolymer surfactant $-\text{CH}_2\text{CH}_2\text{O}-_{106}-\text{CH}_2(\text{CH}_3)\text{CHO}-_{70}-\text{CH}_2\text{CH}_2\text{O}-_{106}$ (Pluronic F127, $M_{\text{AVG}}=12600$) was used as a structure-directing template. Hydrochloric acid of 37% purity, as well as citric acid and titanium (IV) isopropoxide (Sigma Aldrich Ti(OC₃H₇)₄), were employed as co-reactants.

In a typical synthesis, 400 mL of ethanol (CH_3CH_2OH) from Commercial Alcohols (A Trade Name of Greenfield Specialty Alcohols) were acidified with 33.00 g of hydrochloric acid (37 wt. % purity). After combining these reagents, 20.00 g of Pluronic F127 were added, and the suspension was mixed until dissolution (0.5 h). Then, 6.30 g of citric acid were incorporated under intense stirring. Following this procedure, the solution pH was adjusted to 0.75. Mixing continued at ambient temperature for 1 h. Once this step was completed, 28.50 g of titanium (IV) isopropoxide were added dropwise. The resultant liquid phase, displaying a sol-gel appearance, was mixed for 24 h. At the end of this period, it was split in two equal solutions, labelled A and B. The resulting sol-gel phases were evaporated and calcined by gradually increasing the temperature, from room temperature to 773 K (500°C) for flask A and to 823 K (550°C) for flask B at a 1° C/min heating rate. Once the desired thermal level was reached (*i.e.* 773 K for A and 823 K for B), this temperature was kept during 6 h under ambient air to calcine the sample and combust the organic template.

Synthesis conditions selected secured template-free self-assembled mesoporous titania nanoparticles. Samples obtained following this process were labeled as TiO₂- Meso-500°C and TiO₂- Meso-550°C, respectively.

Given the importance of doping TiO₂ with Pt for water splitting [36], the synthesized mesoporous titania of the present study, was also doped with platinum incorporated into the TiO₂ lattice. Titanium (IV) isopropoxide template method was modified with the use of hexachloroplatinic acid hydrate (Sigma Aldrich H₂PtCl₆*xH₂O). Titanium (IV) isopropoxide was added in the sol-gel concurrently with the Pt containing species.

Samples prepared using the above described steps were designated as: a) 1.00 wt. % Pt-TiO₂-Meso-500°C and 2.50 wt. % Pt-Meso-TiO₂-500°C and b) 1.00 wt. % Pt- TiO₂- Meso-550°C, and 2.50 wt. % Pt-TiO₂- Meso-550°C.

4.3.2 Photocatalytic Performance

The photocatalytic activity of the synthesized semiconductors was determined using a Photo-CREC Water-II bench scale photoreactor (PCWII) [36] containing a hydrogen

storage tank with jet driving mixing. PCWII is comprised of a 2.65 L internally irradiated slurry annular section and a total 6.00 L slurry volume. A 15 W EIKO T8 Black-Light-Blue (BLB) lamp is the light source. This lamp displays a wavelength peak at 370 nm and emits in the range of 320 nm to 410 nm. The photocatalyst loading was evaluated in the range 0.05-1.00 g/l in an acid medium ($\text{pH} = 4.00 \pm 0.05$). A 1.00 g of $\text{TiO}_2/\text{Liter}$ loading was used with Pt embedded in the mesoporous TiO_2 . This was done to ensure that a 90 % of the incident energy was absorbed in all experiments. Absolute ethanol was used as a renewable organic scavenger. Ethanol was kept at 2 % v/v as reported in our previous studies [36].

4.3.3 Apparatus

Figure 4.1 reports a description of the Photo-CREC Water-II reactor with the following components: (1) 15-W black light lamp or (BLB), (2) Pyrex glass inner tube with a 3.58 cm diameter, (4) silica windows, (5) black polyethylene outer tube, (6) stirred tank, (7) centrifugal pump, (8) purging gas injector, and (9) sampling port. 15-W lamp, 1.33 cm radius, 41.3 cm length, black-light UV lamp is positioned at the center of the inner Pyrex tube, which was selected given its high irradiation transmittance.

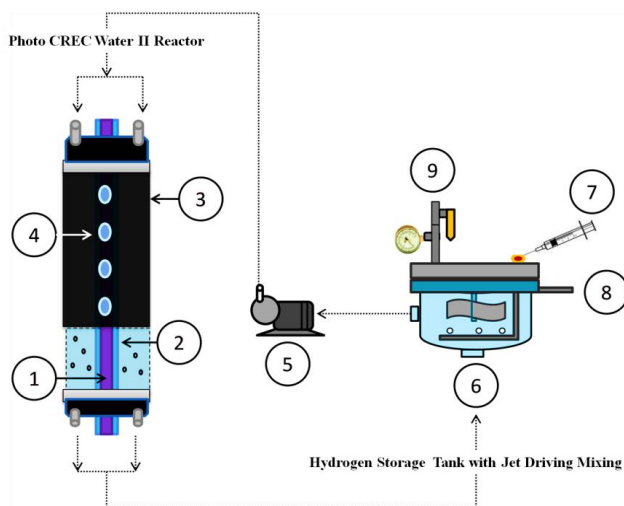


Figure 4.1 Schematic diagram of the Photo-CREC-Water-II photoreactor with a H_2 mixing tank: (1) BLB lamp, (2) Pyrex glass tube, (3) UV-opaque polyethylene cylinder, (4) fused-silica windows, (5) centrifugal pump, (6) H_2 storing/mixing tank, (7) gas sampling port, (8) purging gas injector and (9) draining gas valve.

4.4 Photocatalyst Characterization

4.4.1 XRD diffractograms

Powder XRD spectra were taken on using a Rigaku Rotating Anode X-Ray Diffractometer employing CuK α radiation. The instrument was operated at 45 kV and 160 mA. X-rays were collimated using 1° divergent and scatter slits, and a 0.15-mm receiving slit. Continuous scans were collected over the 2 θ range 20-80° with a step size of 0.02° for a dwell time of 2 seconds per step.

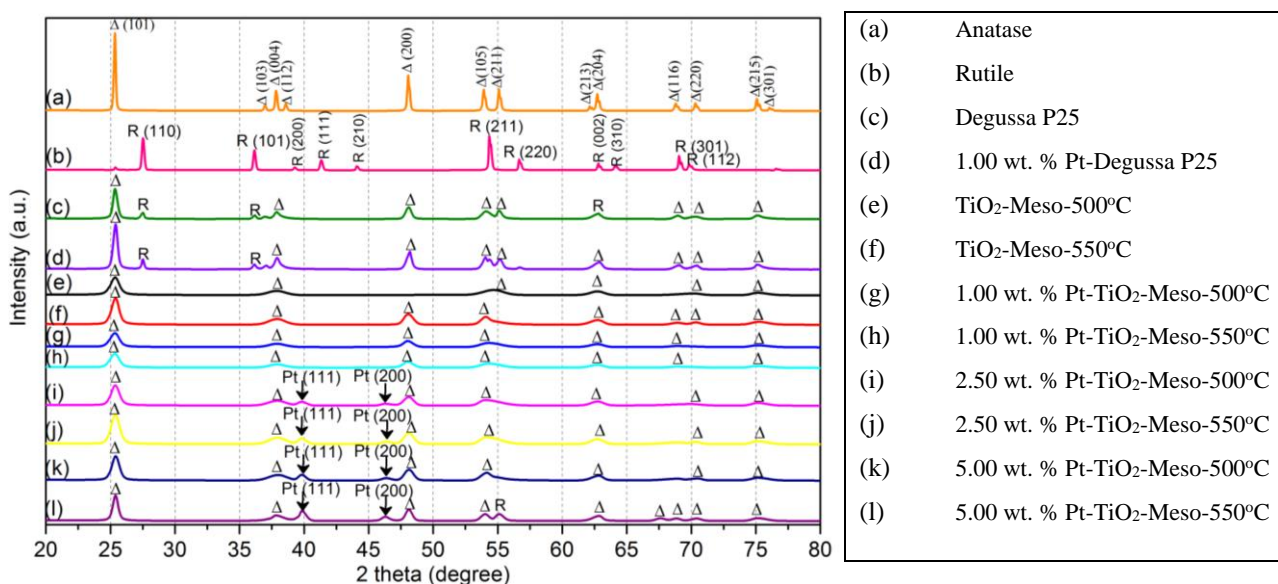


Figure 4.2 XRD diffractograms of the photoactive materials for hydrogen production. XRD diffractograms were overlapped for comparison. (Δ) represents TiO₂ in the anatase phase and (R) indicates TiO₂ in the rutile phase.

One can observe in Figure 4.2 that the characteristic crystalline phases for TiO₂ are also present in the mesoporous TiO₂ calcined at 500 °C and 550 °C, respectively. Figure 4.2 also provides XRD for other TiO₂-based photocatalysts doped with platinum, curves (g)-(l). For those cases, the characteristic anatase peaks at the 2 θ diffraction angles of 25, 38, 48, 54, 63, 69, 70.5 and 75° corresponding to the planes (101), (004), (200), (105), (204), (116), (220) and (215) were consistently observed. Figure 4.2 (d) shows small extra peaks

for the 1.00 wt.%-Pt-Degussa P25 at 27, 36, 55.1 and 57° corresponding to the rutile phase in the planes (110), (101), (211) and (220) respectively.

Furthermore, the XRD diffractograms of Figure 4.2 (i)-(l), for the loadings of 2.50 and 5.00 wt.% platinum, in the mesoporous TiO₂, report an extra peak at 47° in the 2θ scale. This can be attributed to the Pt, which modifies the TiO₂ with an extra crystalline phase. An interesting observation is that when increasing the Pt loading, the 47° peak augments in intensity. Close examination of the peaks in Figures 2 (i)-(l), reveals that two of them occurred for the samples with Pt. These peaks can be attributed to the (111) and (200) reflections of the Pto (JCPDF 01-1194) possessing a face-centered cubic structure. These peaks are weak and broad, indicating the nanocrystalline nature of the Pt particles.

Figure 4.2 also shows the effect of the Pluronic and the Pt loading on theTiO₂. It is shown that the Pluronic F127-modified mesoporous TiO₂ displays a lower crystallinity than that of non-porous TiO₂ (i.e. 1.00 wt. %-Pt/Degussa P25). However, the addition of the Pt increases crystallinity of the mesoporous TiO₂. Moreover, an increase in Pt loading leads to higher XRD intensities with a narrowing of the (111) peak, indicating a progressive growth of crystallites.

Table 4.1 reports the crystallite sizes for several TiO₂ used, as calculated with the Scherrer equation. The synthesized mesoporous TiO₂ displays 8-11 nm crystallite sizes. This is in contrast with the 21-22 nm for the Degussa P25 and the 48, 51 nm for anatase and rutile, respectively.

Table 4.1 Crystallite sizes of mesoporous TiO₂, Pt-TiO₂ with different Pt loadings

Photocatalyst	Crystallite size ^a (nm)
Meso-TiO ₂ -500°C	8
Meso-TiO ₂ -550°C	8
1.00 wt. % Pt / Meso-TiO ₂ -550°C	10
2.50 wt. % Pt / Meso-TiO ₂ -550°C	10
5.00 wt. % Pt / Meso-TiO ₂ -550°C	11
1.00 wt. % Pt / Degussa P25	22
Degussa P25	21

Anatase	48
Rutile	51

^aXRD-method.

4.4.2 N₂ adsorption-desorption isotherms of mesoporous TiO₂

In order to establish the structural differences, potentially affecting the photocatalytic activity for hydrogen formation from water splitting, the synthesized mesoporous TiO₂ were analyzed using N₂ adsorption-desorption isotherms and BET method. Nitrogen adsorption and desorption isotherms at -195°C were measured using a Micrometrics ASAP-2010 specific surface area and porosity analyzer. This was accomplished once the mesoporous TiO₂ samples were degassed in a vacuum at 250 °C for 2 h. Figure 4.3 and Figure 4.4 report typical examples of the nitrogen adsorption-desorption isotherms obtained in the present study.

Adsorption-desorption isotherm of the synthesized mesoporous materials (Figure 4.3) belongs to a Type IV classification [55-57]. This isotherm features a hysteresis loop, associated with capillary condensation in the mesopores, and a limited nitrogen uptake over a range of high P/P_0 . The initial branch of the isotherm is attributed to a monolayer coverage. Type IV isotherms are found in many mesoporous industrial adsorbents [58].

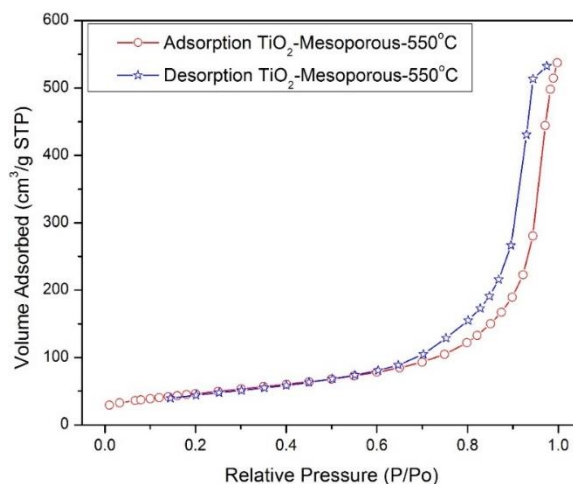


Figure 4.3 N₂ adsorption-desorption isotherm of mesoporous TiO₂ semiconductor calcined at 550 °C.

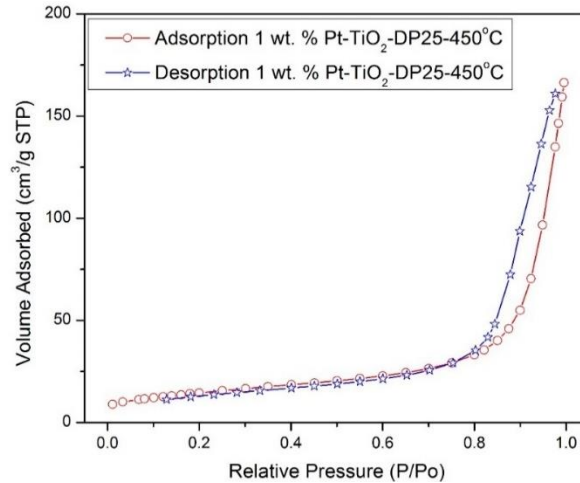


Figure 4.4 N₂ adsorption-desorption isotherm of 1.00 wt. % -Pt / Degussa P25 heated at 450 °C.

The specific surface area was calculated using the Brunauer-Emmett-Teller (BET) plot. As shown in **Table 4.2**, typical values obtained for the mesoporous TiO₂ were in the 130-170 m²/g range. This was significantly higher than the 50 m²/g for the commercial Degussa P25 and compared to the 7-8 m²/g for anatase and rutile, respectively.

Table 4.2 Specific surface area, pore volume and pore diameter for different photocatalyst materials. Also, metal dispersion for mesoporous TiO₂ materials is reported.

Photocatalyst	S _{BET} (m ² g ⁻¹)	V _p ^{BJH} (cm ³ g ⁻¹)	D _p ^{BJH} (4 V _p ^{BJH} / S _{BET})(nm)	Metal Dispersion (%)
Meso-TiO ₂ -550°C	168	0.68	16.2	N/A
1.00 wt. % Pt / Meso-TiO ₂ -550°C	136	0.45	13.2	54.2
2.50 wt. % Pt / Meso-TiO ₂ -550°C	150	0.68	18.1	45.7
5.00 wt. % Pt / Meso-TiO ₂ -550°C	155	0.66	20.1	25.7
1.00 wt. % Pt / Degussa P25	52	0.21	16.2	21.2
Degussa P25	50	0.25	20.0	N/A
Anatase	8	0.05	25.0	N/A
Rutile	7	0.05	28.6	N/A

In addition, pore size distributions were calculated by employing the Barrett-Joyner-Halenda (BJH) model. The pore volume was measured at $P/P_0 = 0.99$. Helium gas was used for dead region measurements, whereas nitrogen was utilized to establish sorbed gas.

Figure 4.5 reports the Barrett-Joyner-Halenda (BJH) pore size distribution plots, for the synthesized mesoporous semiconductor calcined at 550 °C.

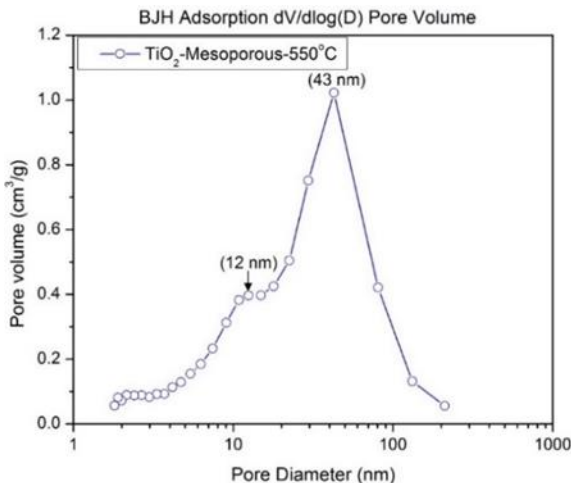


Figure 4.5 Barrett-Joyner-Halenda (BJH) pore size distribution plot of mesoporous TiO₂ calcined at 550 °C.

Figure 4.5 shows a bimodal pore size distribution plot. This bimodal pore volume distribution was consistently observed for the following TiO₂ based materials: a) Meso-TiO₂-500°C, b) Meso-TiO₂- 550°C, c) 1.00 wt.-%-Pt-Meso-TiO₂-500°C, d) 1.00 wt.-%-Pt-Meso-TiO₂-550°C, e) 2.50 wt. %-Pt- Meso-TiO₂-500°C. These distributions display pore sizes belonging to both 12-15 nm range and 30-46 nm range.

Only one TiO₂-based material studied displayed a single pore size distribution, as shown in Figure 4.6. This was found on the 1.00 wt.-%-Pt- Degussa P25-450°C. Average pore sizes were in the 4-nm range.

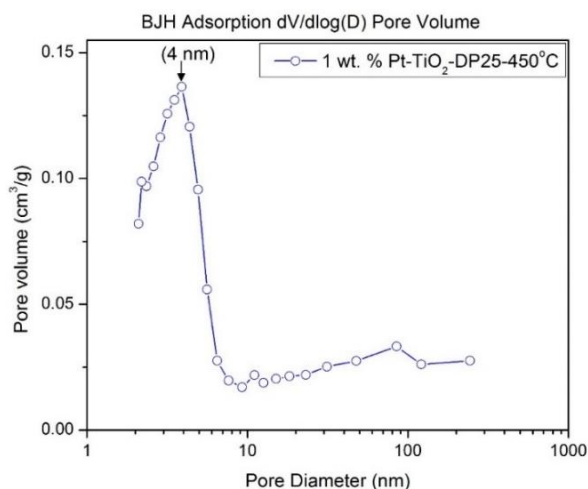


Figure 4.6 Barrett-Joyner-Halenda (BJH) pore size distribution plot of 1.00 wt. %-Pt-TiO₂ Degussa P25 semiconductor heated at 450 °C.

4.4.3 X-ray photoelectron spectroscopy (XPS)

X-ray photoelectron spectroscopy (XPS) experiments were performed to investigate: a) the concentration of the titanium and platinum in the mesoporous titania, b) species oxidation state and c) their effect on the semiconductor structure (Figure 4.7a and Figure 4.7b).

The survey spectra for all samples exhibited strong XPS peaks for titanium and oxygen. On this basis meso-TiO₂ powders were examined and this to assess the amount of Ti³⁺ versus Ti⁴⁺ ions. Moreover, the chemical state of platinum on the photocatalyst surface was also investigated with platinum species displaying moderate XPS peaks. Additional discussion of the XPS spectra obtained for the Pt-TiO₂ photocatalyst are reported in Appendix B - Supplementary material of Chapter 4.

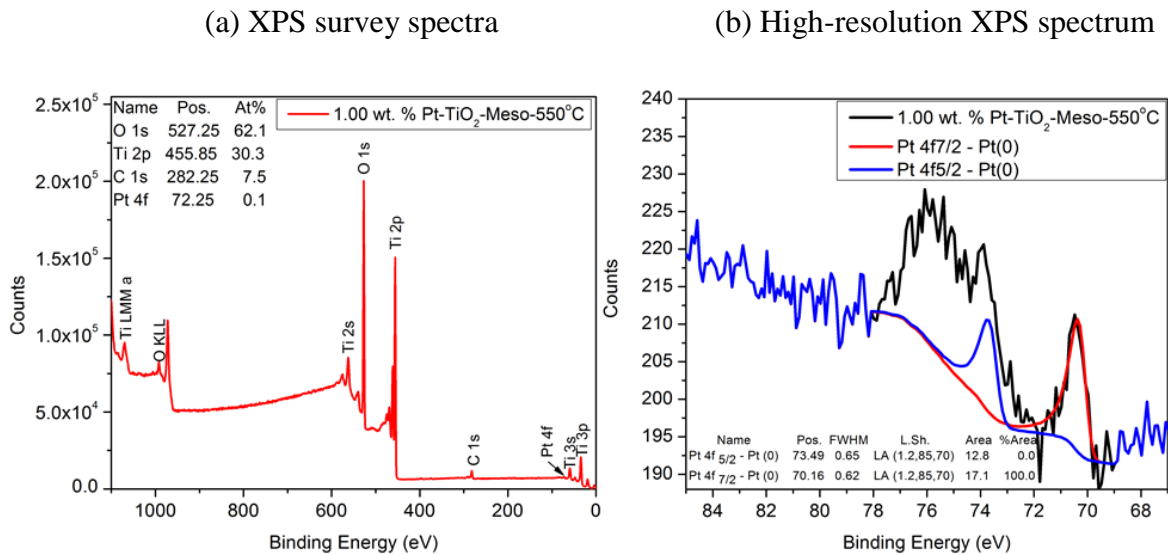


Figure 4.7 X-ray photoelectron spectroscopy (XPS) of 1.00 wt. % Pt-mesoTiO₂-550 °C.

Evidence suggests that synthesis conditions influence TiO₂ structural properties. Synthesis conditions must be carefully controlled during photocatalyst synthesis to achieve adequate pore size distribution and high specific surface area. Thus, a successful photocatalyst design with adequate properties for hydrogen production, should encompass key synthesis steps as follows: a) The preparation of 10-40 nm mesoporous TiO₂ with carefully sized pores. This can be accomplished using sol-gel synthesis and a wisely selected organic template, b) The addition of a platinum precursor in an acidic medium to achieve high platinum dispersion. This can be attained using a stable platinum containing *platinic species under acidic conditions*, c) The use of a moderate 500-550°C calcination temperature. This leads to Pt in the metallic state directly, and eliminates the requirement of further reduction steps of the photocatalyst.

4.4.4 Band gap

UV-Vis spectra of the photocatalysts in solid phase were recorded using a UV-Vis-NIR spectrophotometer (Shimadzu UV-3600) equipped with an integrating sphere using BaSO₄ as a reference.

Determination of semiconductor optical band gap is required to determine wavelengths that activate the photocatalyst. To this end, the Kubelka-Munk (K-M) function and the Tauc plot method was used [48]. “Indirect band gap” data treatment designated as the Kubelka-Munk (K-M) and a Tauc plot is highly recommended for the synthesized photocatalysts [49-50].

Figure 4.8 reports the UV-vis spectra at various wavelengths, reported at 500°C for different loadings of platinum.

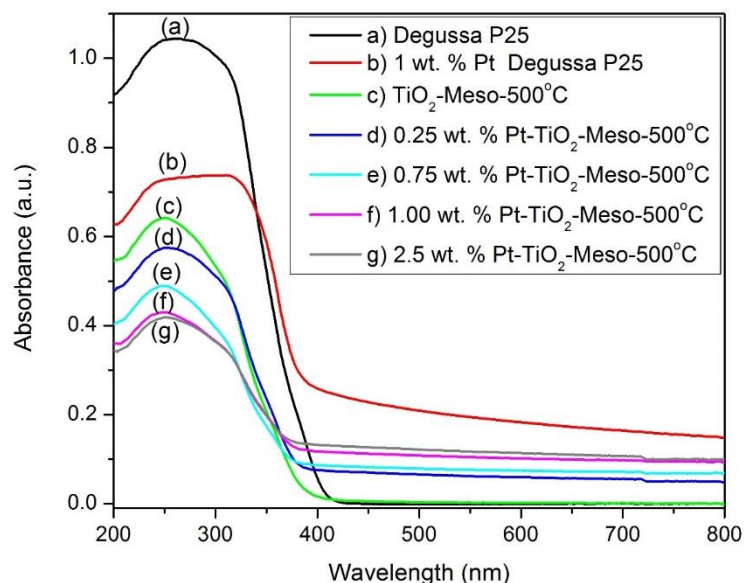


Figure 4.8 UV-vis absorption spectra of the different semiconductor materials calcined at 500°C: a) Degussa P25, b) 1.00 wt. % Pt / Degussa P25-450°C, c) Meso-TiO₂, d) 0.25 wt. % Pt- Meso-TiO₂, e) 0.75 wt. % Pt- Meso-TiO₂, f) 1.00 wt. % Pt- Meso-TiO₂ and g) 2.50 wt. % Pt- Meso-TiO₂.

Figure 4.8 shows that the commercial TiO₂ (Degussa P25) displays the highest absorbance values, whereas the prepared mesoporous materials (Meso-TiO₂), consistently gives lower absorbance. This shows as well, that Pt loading influences the UV-vis spectra, with reduced absorbance for increased platinum loadings.

Furthermore, considering the straight-line approximation and the intersection with the abscissa axis, one can determine larger wavelengths at zero absorbance or the equivalent,

a band gap reduction with increased Pt. This finding agrees with the XRD measurements described above, showing new crystalline phases with Pt addition.

Figure 4.9 reports the UV-vis absorbance as a function of the wavelength for the photocatalyst calcined at 550 °C, an increased wavelength at zero absorbance for both Meso-TiO₂ and Meso-TiO₂ with loaded Pt is observed.

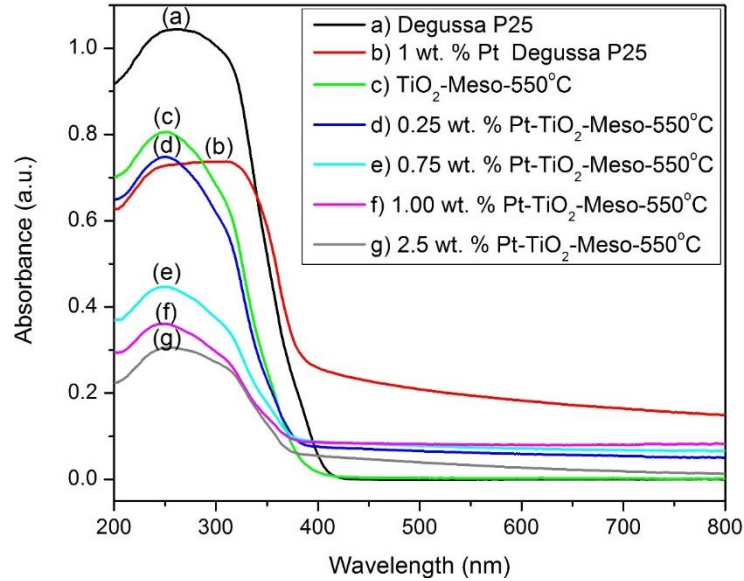


Figure 4.9 UV-vis absorption spectra of the different semiconductor materials calcined at 550°C: a) Degussa P25, b) 1.00 wt. % Pt / Degussa P25-450°C, c) Meso-TiO₂, d) 0.25 wt. % Pt- Meso-TiO₂, e) 0.75 wt. % Pt-Meso-TiO₂ f) 1.00 wt. % Pt-Meso-TiO₂ and g) 2.50 wt. % Pt- Meso-TiO₂.

Regarding the optical band gaps, the Kubelka-Munk (K-M) function coupled with “indirect” procedure (Tauc plots) was adopted as follows:

- a) The $\sqrt{\alpha h\nu}$ variable was selected for the “y” ordinate, with α representing the UV-vis absorbance.
- b) The $h\nu$ variable was chosen for the ‘x’ abscissa, with h being the Planck constant (6.63×10^{-34} Joule/s), c denoting the light speed (3.0×10^8 m/s) and $\nu = \frac{c}{\lambda}$ representing the irradiation frequency.

On this basis, TAUC plots as in Figure 4.10-4.13 were obtained.

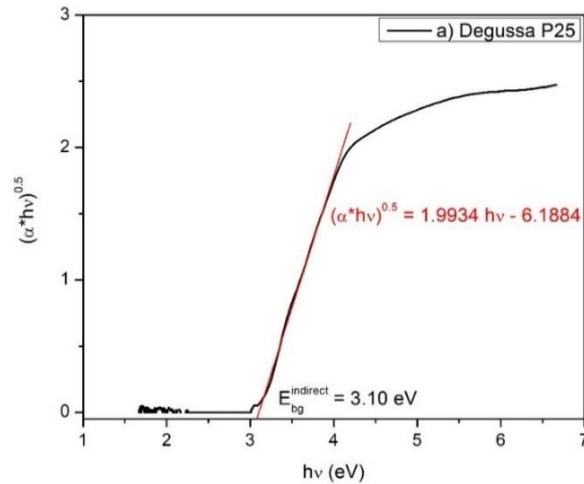


Figure 4.10 Optical band gap calculation for Degussa P25 (DP25) using the Tauc plot method. This plot was established using the UV-vis absorption spectra. Calculated using indirect band gap = 3.10 eV.

Regarding the TAUC plots method, as in Figure 4.10, the linear section close to the inflection point region has to be considered according to the Tauc plots method. The resulting straight line provides the equation $(\alpha * hv)^{1/2} = 1.9934 (hv) - 6.1884$, with a 0.996 regression coefficient. Furthermore, the intersection of this straight line with the abscissa axis at $(\alpha * hv)^{1/2} = 0$, yields $E_{bg} = hv$, $1.9934 (E_{bg}) - 6.1884 = 0$ and $E_{bg} = 6.18/1.99 = 3.10$ eV.

A similar analysis is developed in Figure 4.11 and Figure 4.12, for the cases of Meso-TiO₂-550°C and 2.50 wt. % Pt-Meso-TiO₂-550°C. The calculated band gaps are 2.99 eV and 2.34 eV, respectively.

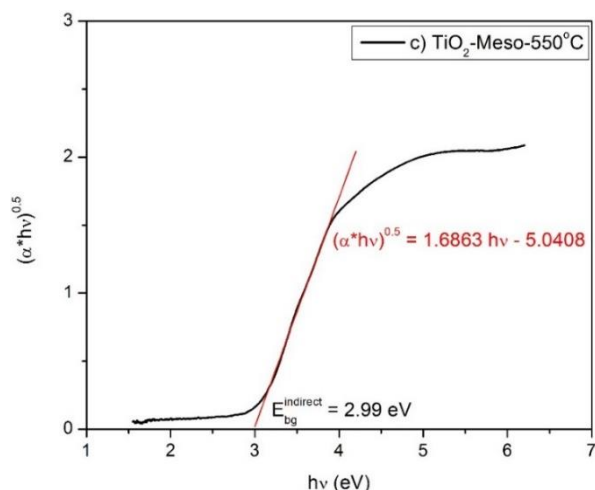


Figure 4.11 Optical band gap calculation for Meso-TiO₂-550°C using the Tauc plot. This plot was established using the UV-vis absorption spectra. Calculated indirect band gap = 2.99 eV.

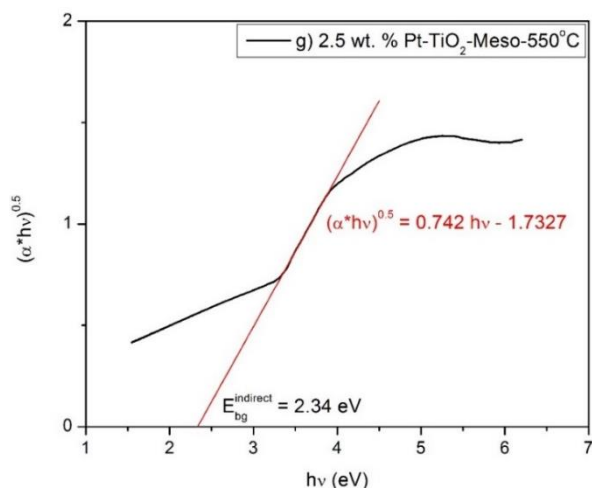


Figure 4.12 Optical band gap determination for a 2.50 wt. % Pt-Meso-TiO₂-550°C using the Tauc Plot. This plot was established on the basis of the UV-vis absorption spectra. Calculated indirect band gap = 2.34 eV.

Figure 4.13 and Figure 4.14 describe the influence of platinum loading on the optical band gaps for the semiconductors synthesized in this work.

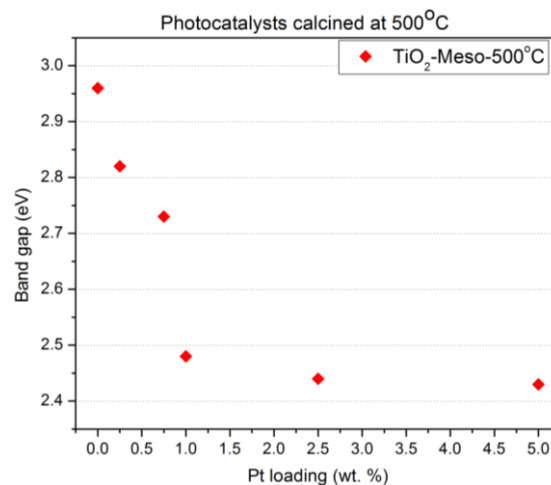


Figure 4.13 Effect of platinum loading on the optical band gap of semiconducting materials calcined at 500 °C.

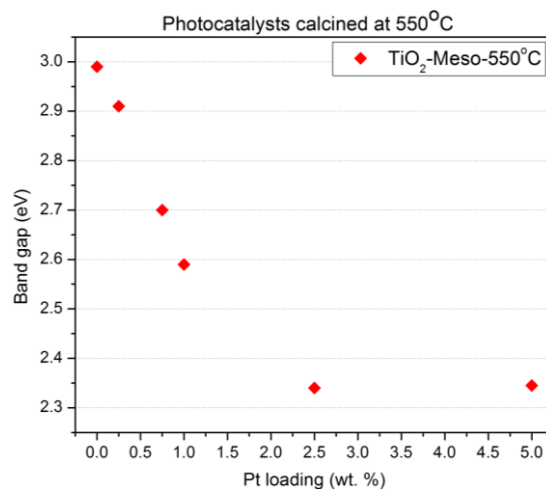


Figure 4.14 Effect of platinum loading on the optical band gap of semiconducting materials calcined at 550 °C.

Table 4.3 and Table 4.4 report a comparison of various band gaps for the materials of the presents study, showing the progressive reduction with the increased Pt loadings.

Table 4.3 Optical band gap of materials calcined at 500°C, calculated with the Kubelka-Munk (K-M) function and Tauc plot method.

Semiconductor	Band gap (eV)	Wavelength associated to the band gap, λ_{bg} (nm)	% of the visible light region absorbed (theoretically) as per equation 4.1
Degussa P25	3.10	400	0
TiO ₂ -Meso-500°C	2.96	419	0
0.25 wt % Pt-TiO ₂ -500°C	2.82	440	13.3
0.75 wt % Pt-TiO ₂ -500°C	2.73	454	18.0
1.00 wt % Pt-TiO ₂ -500°C	2.62	473	24.3
2.50 wt % Pt-TiO ₂ -500°C	2.44	508	36.0

Table 4.4 Optical band gap of materials calcined at 550°C, calculated with the Kubelka-Munk (K-M) function and Tauc plot method.

Semiconductor	Band gap (eV)	Wavelength associated to the band gap, λ_{bg} (nm)	% of the visible light region absorbed (theoretically) as per equation 4.1
Degussa P25	3.10	400	0
TiO ₂ -Meso-550°C	2.99	415	5.0
0.25 wt % Pt-TiO ₂ -550°C	2.91	426	8.7
0.75 wt % Pt-TiO ₂ -550°C	2.70	459	19.7
1.00 wt % Pt-TiO ₂ -550°C	2.59	454	18.0
2.50 wt % Pt-TiO ₂ -550°C	2.34	530	43.3

Table 4.3 and Table 4.4 report the optical band gaps for commercial TiO₂ (Degussa P25) and Meso-TiO₂-500°C and Meso-TiO₂-550°C. These results show that the TiO₂ architecture has an effect on band gaps, with this being assigned to the higher anatase content of the mesoporous TiO₂. Both Table 4.3 and Table 4.4 also show that the band gap is consistently reduced at increasing the Pt loading.

One can notice that there is a consistent band gap reduction with platinum loading. Furthermore, the higher calcination temperature of 550°C, provides a slightly enhanced λ_{bg} . Thus, on the basis of the above, one can conclude that the platinum added mesoporous materials are able to more effectively use the visible light. A quantification of this enhanced visible light irradiation can be accounted for using the following equation:

$$\text{Visible Utilized Irradiation \% (VUI)} = \frac{\int_{\lambda_{min}}^{\lambda_{bg}} I d\lambda}{\int_{\lambda_{min}} I d\lambda} \times 100\% \quad \text{Eq. (4.1)}$$

with I, being the irradiance, λ_{min} and λ_{max} representing the minimum and the maximum wavelengths of solar irradiation and λ_{bg} denoting the wavelength associated to the measured optical band gap.

Both Table 4.3 and Table 4.4 report the expected VUI% which is increased up to 36%-43%, as a result of Pt addition.

4.4.5 Scanning electron microscopy (SEM)

SEM micrographs of mesoporous TiO₂ photocatalysts with different Pt loadings are shown in Figure 4.15. One can observe, the Pt-TiO₂ powders under calcination at 550 °C exhibit increased grain and pore sizes. This may be explained due to calcination at 550 °C improving the crystallinity of TiO₂ materials and correspondingly the combustion of Pluronic F127 promoted increasing pore size.

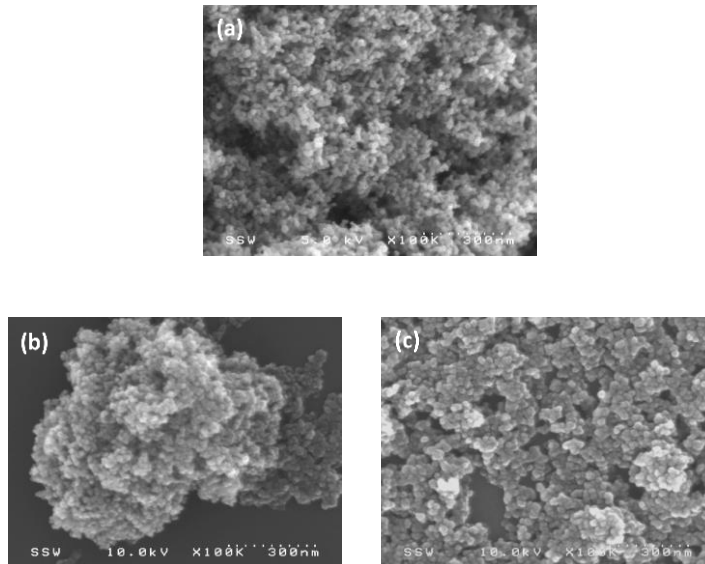


Figure 4.15 SEM images of mesoporous Pt–TiO₂ photocatalysts prepared with different platinum loading at 550°C calcination temperature. (a) 1.00 wt. % Pt-TiO₂–Mesoporous; (b) 2.50 wt% Pt-TiO₂–Mesoporous; (c) 5.00 wt. % Pt-TiO₂–Mesoporous.

4.5 Hydrogen Production via Water Splitting

Experiments of hydrogen formation via photocatalytic water splitting were performed using the Photo-CREC Water-II Reactor (refer to Figure 4.1). This unit was used with a specially designed H₂ collector tank and a BLB lamp that permits the entire use of the near-UV light irradiation spectrum. 2.00 v/v% ethanol (EtOH) was employed as a hole (h⁺) scavenger. This research also took advantage of the mesoporous semiconductor material of TiO₂ and its modifications with Pt conveniently reduced optical band gap.

Experiments in the Photo-CREC Water-II Reactor also allowed determining the production of different intermediates and by-products such as: 1) liquid phase: CH₃COOH and 2) gas phase: forms CO₂, CH₄ and C₂H₆ under oxygen free conditions. These were formed during photocatalytic hydrogen generation.

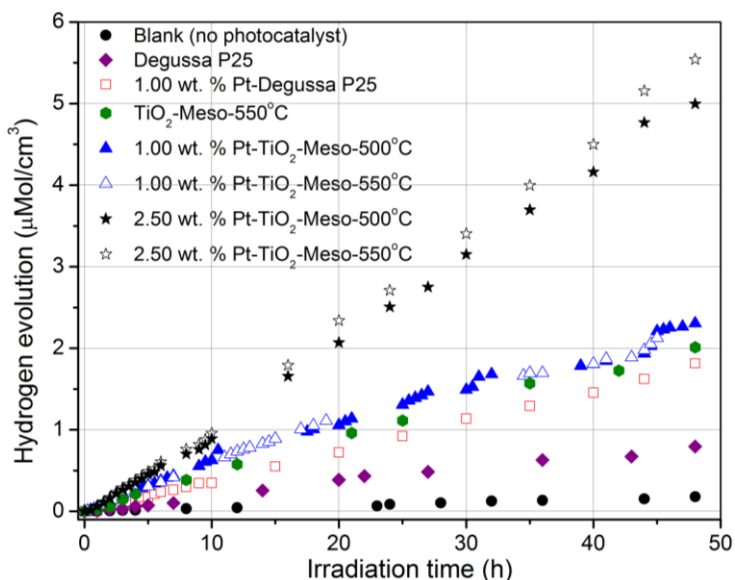


Figure 4.16 Hydrogen evolution for different semiconductor materials at pH = 4.00 ± 0.05 and 2 % v/v ethanol. Photocatalyst loading 1.00 g/l. Standard deviation for repeats ± 5 %.

Figure 4.16 shows that in all cases, there is a steady hydrogen increase throughout the entire run with no observable photocatalyst activity decay. Experiments in the Photo-CREC Water-II Reactor showed a major growth in H₂ production when Pt is added in the mesoporous TiO₂ at 2.50 wt. %. Hydrogen generation with an ethanol scavenger proceeds

consistently via a similar redox network path yielding CH₃COOH, H₂O₂, CH₄, C₂H₆, and CO₂.

4.6 Quantum Yields (QYs)

The comparison of the performance of TiO₂ semiconductors for hydrogen production needs a rigorous assessment of QY [51-54]. The adequate definition of QYs requires macroscopic energy balances allowing Q_{abs} to be measured. The so-called quantum yield is defined as the ratio of the moles of photons effectively converted into products to the moles of absorbed photons. Thus, QY can be calculated as follows:

$$QY = \frac{2 \text{ Moles of } H_2 \text{ Produced/s}}{\text{Moles of Photons Absorbed/s}} \quad \text{Eq. (4.2)}$$

In this calculation, the photons absorbed (Pa) were calculated using macroscopic balances taking into account incident, transmitted and reflected photons [36]. The number of Einstein effectively converted in hydrogen production can be easily calculated as twice the moles of hydrogen formed, due to two electrons being needed to produce one hydrogen molecule.

A significant increase, from the 7.9 % of the previous QY values reported [36], to the 9.6 % and to the 22.6 % QY values for 1 wt. %-Pt-TiO₂-Meso-550 °C and 2.50 wt. %-Pt-TiO₂-Meso-550°C photocatalysts is observed, respectively. These QY enhancements are assigned to the favourable influence of mesoporous architectures of the synthesized semiconductors in the present study.

Table 4.5 reports the QY (%) of the semiconductors prepared in this study. The 2.50 wt. %-Pt- TiO₂-Meso-550°C displays a 22.6 % QY, about 6 times greater than that for bare DP25 displaying only a 3.5 % QY. Appendix C reports additional clarifications concerning the QYs calculations.

Table 4.5 Quantum yields for mesoporous platinum modified TiO₂, showing the effect of different loadings of Pt with a pH = 4.00 ± 0.05 in the Photo-CREC Water-II reactor.

Photocatalyst	QY (%)
Meso-TiO ₂ -550°C	9.3
1.00 wt % Pt/ Meso-TiO ₂ -550°C	9.6
2.50 wt % Pt/ Meso-TiO ₂ -550°C	22.6
5.00 wt % Pt/ Meso-TiO ₂ -550°C	13.7
1.00 wt % Pt/ TiO ₂ Degussa P25	7.0
Degussa P25 TiO ₂	3.5
Anatase	N/A
Rutile	N/A

Thus, and on the basis of results obtained in the present study, one can establish that doped Pt in mesoporous TiO₂, using near UV irradiation and ethanol as a scavenger, can yield considerably enhanced QY for hydrogen production from water splitting. It is our view that the proposed mesoporous TiO₂-Pt data may be most valuable for the engineering of scaled up photoreactors for hydrogen production.

4.7 Conclusions

The following are the conclusions of this chapter:

- a) The mesoporous photocatalysts of the present study, prepared by a sol-gel method, display large surface areas (up to 150 cm²/g⁻¹ level) and a bimodal pore size distribution (on one hand 10 nm and on the other 40 nm).
- b) These mesoporous photocatalysts have a dominant anatase crystalline phase and show a decrease of the band gap (2.34 eV level vs. 3.20 eV for bare TiO₂) with 2.50 wt. % Pt addition.
- c) These semiconductors are shown to display a zero-order reaction for hydrogen production with this being true for all photocatalysts studied.
- d) Hydrogen formation is proven to increase with Pt loading when using ethanol at 2.00 % v/v concentration. This shows the very important role played by Pt reducing the semiconductor band gap and trapping the electrons generated.
- e) The synthesized Pt-mesoporous semiconductors are shown to display promising QYs of 22.6 % for the 2.50 wt. % Pt-TiO₂-Meso.

4.8 References

- [1] Mao, S.; Shen, S. & Guo, L. Nanomaterials for renewable hydrogen production, storage and utilization. *Progress in Natural Science: Materials International*. 22 (2012) 522-534.
- [2] Jing, D.; Guo, L.; Zhao, L.; Zhang, X.; Liu, H.; Li, M.; Shen, S.; Liu, G. & Hu, X. Efficient solar hydrogen production by photocatalytic water splitting: From fundamental study to pilot demonstration. *International Journal of Hydrogen Energy*. 35 (2010) 7087-7087.
- [3] Häussinger, P.; Lohmüller, R. & Watson, A. Hydrogen, 1. Properties and Occurrence. *Ullmann's Encyclopedia of Industrial Chemistry*, 2011, pp. 1-15.
- [4] Navarro, Y.; Rufino M.; Álvarez-Galván, M.C.; Del Valle, F.; Villoria De La Mano, J.A. & Fierro, J.L.G. Water Splitting on Semiconductor Catalysts under Visible-Light Irradiation. *ChemSusChem*. 2 (2009) 471-85.
- [5] Navarro, R.M.; Del Valle, F.; Villoria De La Mano, J.A.; Álvarez-Galván, M.C. & Fierro, J.L.G. Photocatalytic Water Splitting Under Visible Light: Concept and Catalysts Development. *Photocatalytic Technologies. Advances in Chemical Engineering*. 36 (2009)111-43.
- [6] Maeda, K.; Teramura, K.; Lu D.; Takata, T.; Inoue, S.; & Domen, K. Photocatalyst releasing hydrogen from water. *Nature*. 440 (2006) 295-295.
- [7] Nakata, K. & Fujishima, A. TiO₂ photocatalysis: Design and applications. *Journal of Photochemistry and Photobiology C: Photochemistry Reviews*, 13 (2012) 169-189.
- [8] Nowotny J.; Sorrell, C.C.; Sheppard, L.R. & Bak, T. Solar-hydrogen: Environmentally safe fuel for the future. *International Journal of Hydrogen Energy*, 30 (2005) 521-544.
- [9] U.S. Department of Energy. Hydrogen production. Fuel cells and infrastructure technologies program, 3 (2009)1-20.
- [10] Honda, K and Fujishima, A. Electrochemical Evidence for the Mechanism of the Primary Stage of Photosynthesis. *Bulletin of the Chemical Society of Japan*. 44 (1971) 1148-1150.
- [11] Honda, K and Fujishima, A. Electrochemical Photolysis of Water at a Semiconductor Electrode. *Nature*. 238 (1972) 37-38.

- [12] Du, P.; Schneider, J.; Li, F.; Zhao, W.; Patel, U.; Castellano, F.N. & Eisenberg, R. Bi- and terpyridyl platinum(II) chloro complexes: Molecular catalysts or the photogeneration of hydrogen from water or simply precursors for colloidal platinum? *Journal of the American Chemical Society*. 130 (2008) 5056-5058.
- [13] Lei, P.; Hedlund, M.; Lomoth, R.; Rensmo, H.; Johansson, O. & Hammarstrom, L. The role of colloid formation in the photoinduced H₂ production with a Ru(II)-Pd(II) supramolecular complex a study by GC, XPS, and TEM. *J. of the American Chemical Society*. 130 (2008) 26-27.
- [14] Domen, K.; Naito, S.; Soma, M.; Onishi, T.; Tamaru, K. *J. Chem. Soc., Chem. Commun.* 12 (1980) 543-544.
- [15] Sato, S.; White, J. M. *Chem. Phys. Lett.* 72 (1980) 83-86.
- [16] Lehn, J. M.; Sauvage, J. P.; Ziessel, R. *Nouv. J. Chim.* 1980, 4623-4627.
- [17] Domen, K.; Naito, S.; Onishi, T.; Tamaru, K. *Chem. Phys. Lett.* 92 (1982) 433-434.
- [18] Sayama, K.; Arakawa, H. *J. Phys. Chem.* 97 (1993) 531-533
- [19] Inoue, Y.; Kubokawa, T & Sato, K. Photocatalytic activity of sodium hexatitanate, Na₂Ti₆O₁₃, with a tunnel structure for decomposition of water. *Journal of the Chemical Society, Chemical Communications*. 19 (1990)1298–1299
- [20] Inoue, Y.; Niiyama, T.; Asai, T. & Sato, K. Stable photocatalytic activity of BaTi₄O₉ combined with ruthenium oxide for decomposition of water. *Journal of the Chemical Society, Chemical Communications*. (1992) 579–580
- [21] Ikeda, S.; Itani, T.; Nango, K.; Matsumura, M. *Catal. Lett.* 98 (2004) 229-233
- [22] Takata, T.; Furumi, Y.; Shinohara, K.; Tanaka, A.; Hara, M.; Kondo, J. N.; Domen, K. *Chem. Mater.* 9 (1997) 1063-1064.

- [23] Ikeda, S.; Hara, M.; Kondo, J. N.; Domen, K.; Takahashi, H.; Okubo, T.; Kakihana, M. *J. Mater. Res.* 13 (1998) 852-855.
- [24] Kudo, A.; Kato, H. *Chem. Lett.* 26 (1997) 867-877.
- [25] Kim, H. G.; Hwang, D. W.; Kim, J.; Kim, Y. G.; Lee, J. S. *Chem. Commun.* 1999, 1077-1078.
- [26] Cerdá, J.; Marchetti, J. L.; Cassano, A. E. Radiation efficiencies in elliptical photoreactors. *Lat. Am. J. Heat Mass Transfer.* 1 (1977) 33-63.
- [27] Ibrahim, H.; de Lasa, H. Photo-catalytic degradation of air borne pollutants. Apparent quantum efficiencies in a novel photo-CREC-air reactor. *Chem. Eng. Sci.* 58 (2003) 943-949.
- [28] Ibrahim, H. Photo-catalytic reactor for the degradation of airborne pollutants: photo-conversion efficiency and kinetics modeling. Ph.D. dissertation. The University of Western Ontario, London, Canada. 2001
- [29] de Lasa, H.; Serrano, B.; Salaices, M. *Photocatalytic Reaction Engineering*, First Ed., Springer: New York, 2005.
- [30] Hoffmann, M. R.; Martin, S.T.; Choi, W. Environmental Applications of Semiconductor Photocatalysis, *Chem. Rev.* 95 (1995) 69-77.
- [31] Tahiri, H.; Serpone, N.; Le Van Mao, R. Application of concept of relative photonic efficiencies and surface characterization of a new titania photocatalyst designed for environmental remediation. *J. Photochem. Photobiol., A: Chem.* 93 (1996) 199-203.
- [32] Kisch, H. On the Problem of comparing Rates or Apparent Quantum Yields in Heterogeneous Photocatalysis. *Angew. Chem. Int. Ed.* 49 (2010) 9588-9589.
- [33] Escobedo-Salas, S., Serrano-Rosales B., de Lasa, H. Quantum Yield in a Photo-CREC reactor for hydrogen production. *AIChE Annual Meeting* 2012.
- [34] Moreira, J.; Serrano, B.; Ortiz, A. & de Lasa, H. TiO₂ absorption and scattering coefficients using Monte Carlo method and macroscopic balances in a photo-CREC

- unit. *Chemical Engineering Science*. 66 (2011) 5813 – 582.
- [35] Serrano, B.; Ortiz, A.; Moreira, J. & de Lasa, H. Energy efficiency in photocatalytic reactors for the full span of reaction times. *Industrial and Engineering Chemistry Research*. 48 (2009) 9864–9876.
- [36] Escobedo-Salas, S.; Serrano-Rosales B., de Lasa, H. Quantum Yield with Platinum Modified TiO₂ Photocatalyst for Hydrogen Production. *Applied Catalysis-B; Environmental*. 140 (2013) 523-536.
- [37] Valadés-Pelayo, P. J.; Moreira, J.; Solano-Flores, P.; Serrano, Benito; De Lasa, Hugo. Establishing photon absorption fields in a Photo-CREC Water II Reactor using a CREC-Spectroradiometric probe. *Chemical Engineering Science*. 116 (2014) 406-417.
- [38] Swapan K. Das.; Manas K. Bhunia and Asim Bhaumik. Self-assembled TiO₂ nanoparticles: mesoporosity, optical and catalytic properties. *The Royal Society of Chemistry. Dalton Trans.*, 39 (2010) 4382–4390.
- [39] C.C. Nguyen, N.-N. Vu, Trong-On Do, Recent Advances in the Development of Sunlight-Driven Hollow Structure Photocatalysts and their Applications, *Journal of Materials Chemistry A*, 2015, Review Article, 7, 8187-8208.
- [40] M. Reza Gholipour, C.-T. Dinh, F. Beland, Trong-On Do, Nanocomposite heterojunctions as sunlight-driven photocatalysts for hydrogen production from water splitting, *Nanoscale*, Review Article. 7 (2015) 8187-8208.
- [41] C.-T. Dinh, Y. Hoang, f. Kleitz, Trong-On Do, Three-Dimensional Ordered Assembly of Thin-Shell Au/TiO₂ Hollow Nanospheres for Enhanced Visible-Light Driven Photocatalysis. *Angew. Chem. Int. Ed. Engl.*, 2014.
- [42] C.-T. Dinh, M.-H. Pham, Y. Seo, F. Kleitz, Trong-On Do, Design of multicomponent photocatalysts for hydrogen production under visible light using water-soluble titanate nanodisks, *Nanoscale*, 2014.
- [43] Wang, X., Yu, J. C., Yip, H. Y., Wu, L., Wong, P. K. and Lai, S. Y., A Mesoporous Pt/TiO₂ Nanoarchitecture with Catalytic and Photocatalytic Functions. *Chem. Eur. J.*, 11: 2997–3004, 2005.
- [44] Chih-Chieh Chan, Chung-Chieh Chang, Wen-Chia Hsu, Shih-Kai Wang, Jerry Lin, Photocatalytic activities of Pd-loaded mesoporous TiO₂ thin films, *Chemical Engineering Journal*, Volume 152, Issues 2–3, Pages 492-497, 15 October 2009.

- [45] Yan-Feng Zhu, Lu Xu, Juan Hu, Juan Zhang, Rong-Gui Du, Chang-Jian Lin, Fabrication of heterostructured SrTiO₃/TiO₂ nanotube array films and their use in photocathodic protection of stainless steel, *Electrochimica Acta*, Volume 121, 1 March 2014, 361-368.
- [46] Weijiong Dai, Junqing Yan, Ke Dai, Landong Li, Naijia Guan, Ultrafine metal nanoparticles loaded on TiO₂ nanorods: Synthesis strategy and photocatalytic activity, *Chinese Journal of Catalysis*, Volume 36, Issue 11, Pages 1968-1975, November 2015.
- [47] Chapter 6: Diodes. *Fundamentals of Electrical Engineering*. 2nd ed. New York, New York: Oxford UP, 1996. 352-54.
- [48] R. Borja-Urby, L.A. Diaz-Torres, I. Garcia-Martinez, D. Bahena-Urbe, Gilberto Casillas, A. Ponce, M. Jose-Yacaman, Crystalline and narrow band gap semiconductor BaZrO₃: Bi–Si synthesized by microwave–hydrothermal synthesis, *Catalysis Today*, Volume 250, 15 July 2015, Pages 95-101.
- [49] Shamsa Munir, Syed Mujtaba Shah, Hazrat Hussain, Razaqat Ali Khan, Effect of carrier concentration on the optical band gap of TiO₂ nanoparticles, *Materials & Design*, Volume 92, 15 February 2016, Pages 64-72, ISSN 0264-1275.
- [50] E. Barajas-Ledesma, M.L. García-Benjume, I. Espitia-Cabrera, M. Ortiz-Gutiérrez, F.J. Espinoza-Beltrán, J. Mostaghimi, M.E. Contreras-García, Determination of the band gap of TiO₂–Al₂O₃ films as a function of processing parameters, *Materials Science and Engineering: B*, Volume 174, Issues 1–3, 25 October 2010, Pages 71-73.
- [51] Aaron Ortiz-Gomez, Benito Serrano-Rosales, Jesus Moreira-del-Rio, Hugo de-Lasa, Mineralization of Phenol in an Improved Photocatalytic Process Assisted with Ferric Ions: Reaction Network and Kinetic Modeling, *Advances in Chemical Engineering*, Academic Press, 2009, Volume 36, Pages 69-110.
- [52] P.J. Valadés-Pelayo, Jesus Moreira del Rio, Pastor Solano-Flores, B. Serrano, H. de Lasa. Establishing photon absorption fields in a Photo-CREC Water II Reactor using a CREC-Spectro radiometric probe, *Chemical Engineering Science*, Volume 116, 6 September 2014, Pages 406-417.
- [53] P.J. Valadés-Pelayo, J. Moreira, B. Serrano, H. de Lasa, Boundary conditions and phase functions in a Photo-CREC Water-II reactor radiation field, *Chemical Engineering Science*, Volume 107, 7 April 2014, Pages 123-136.

- [54] P.J. Valadés-Pelayo, F. Guayaquil Sosa, B. Serrano, H. de Lasa, Eight-lamp externally irradiated bench-scale photocatalytic reactor: Scale-up and performance prediction, *Chemical Engineering Journal*, Volume 282, 15 December 2015, Pages 142-151.
- [55] Sing, K.S.W.; Everett, D.H.; Haul, R.A.W.; Moscou, L.; Pierotti, R.A.; Rouquerol, J.; Siemieniewska, T. Reporting physisorption data for gas/solid systems with special reference to the determination of surface area and porosity. *Pure Appl. Chem.* 1985, 57, Pages 603–619.
- [56] Broekhoff, J.C.P. Mesopore determination from nitrogen sorption isotherms: Fundamentals, scope, limitations. *Stud. Surf. Sci. Catal.* 1979, 3, Pages 663–684.
- [57] Shields, J.E.; Lowell, S.; Thomas, M.A.; Thommes, M. *Characterization of Porous Solids and Powders: Surface Area, Pore Size and Density*; Kluwer Academic Publisher: Boston, MA, USA, 2004, Pages 43–45.
- [58] Alothman, Z.A. A Review: Fundamental Aspects of Silicate Mesoporous Materials. *Materials* 2012, 5, Pages 2874-2902.

Chapter 5

5 Hydrogen Production via Water Dissociation Using Pt–TiO₂ Photocatalysts: An Oxidation–Reduction Network

The information presented Chapter 5 is based on the article entitled " *Hydrogen Production via Water Dissociation Using Pt–TiO₂ Photocatalysts: An Oxidation–Reduction Network*", published in *Catalysts* Vol. 7 Issue 11 p. 324–345, in October 2017. The sections of this chapter contribute towards the fulfilment of the general objectives a), b) and c) of the PhD dissertation as described in section 1.1 of Chapter 1.

5.1 Introduction

Heterogeneous photocatalysis is a technique based on the excitation of a semiconductor. Photons having enough energy can promote the transition of an electron from the valence band to the conduction band. In this way, a couple of electrical charges are generated: the electron (e^-) and the hole (h^+). It is in this promoted outer semiconductor particle surface site, that the various redox reactions are initiated [1,2,3,4]. Hydroxide ions (OH^-) from dissociated water may react with electron holes (h^+) yielding $\cdot OH$ radicals. These $\cdot OH$ radicals may be consumed by ethanol at 1.00–2.00% v/v concentrations. The efficiency of the photocatalytic process can be enhanced by the addition of so-called sacrificial reagents (i.e., ethanol, methanol) [5–7]. Ethanol is an attractive organic renewable scavenger that can be produced from sugars or agricultural waste fermentation processes at a low cost. Electrons may eventually react with protons (H^+) to form H^\bullet radicals. H^\bullet radicals may dimerize, forming molecular hydrogen (H_2).

Nowadays, TiO₂ is the most widely used photocatalyst due to its photocatalytic activity, chemical stability in aqueous solutions and favourable band gap energy (3.20 eV in anatase) [5]. However, new materials such as modified TiO₂ combined with noble metals are gaining importance in hydrogen production because of the reported reduced band gaps [1,2,6,7]. In 2005, Galinska et al. [4] performed photocatalytic water splitting over Pt–TiO₂ (Degussa P25) using various sacrificial reagents under UV irradiation. Nevertheless, these authors did not report values for the quantum yield. Despite this progress, the value of

doped noble metals on TiO₂ semiconductors for hydrogen production has not yet been established and remains broadly unreported. To address this issue, this PhD thesis describes hydrogen formation via water splitting in a Photo CREC Water-II Reactor (PCW-II) using 2.00% v/v ethanol under inert gas. A diversity of Pt–TiO₂ photocatalysts are evaluated, showing the criticality of the preparation method. This is important to achieve the 22% level of high quantum yield reported in the previous chapter using sol-gel method.

5.2 Quantum Efficiencies

An assessment of photocatalyst performance can be established using quantum efficiency, as shown in Equation (5.1). This is the case for the conversion of organic species in both air and water.

In the case of hydrogen production, a Quantum Yield (QY) can be defined as the ratio between the number of generated chemical species molecules and the number of photons absorbed by the photocatalysts [8]:

$$\text{QY} = \frac{\text{number of produced molecules}}{\text{number of photons absorbed by catalyst}} \quad (5.1)$$

or

$$\% \text{ QY} = \frac{2 \times \left[\frac{dN_{H^\bullet}}{dt} \right]}{P_a} \times 100, \quad (5.2)$$

where (a) the $\frac{dN_{H^\bullet}}{dt}$ represents the rate of moles of formed hydrogen radicals at any time during the photocatalyst irradiation and (b) P_a is the number of moles of photons absorbed by the catalyst per unit of time. Additional details of the P_a calculation are provided in Appendix D.

Regarding the $\frac{dN_{H^\bullet}}{dt}$ rate, it can be calculated by multiplying the slope of the cumulative hydrogen produced by 2. It has to be mentioned that, in this respect, Equation

(5.2) applies to all the photocatalysts considered in the present study. Additional information regarding $\frac{dN_{H^*}}{dt}$ is given in Appendix F.

However, to favour hydrogen production with high quantum yields, one can provide additional electron sites (i.e., inner metal sites) as illustrated in Figure 1. These sites act as electron reservoirs on the photocatalyst inner surface. This approach for enhanced hydrogen production using an organic scavenger over mesoporous TiO₂ doped with Pt has not been reported.

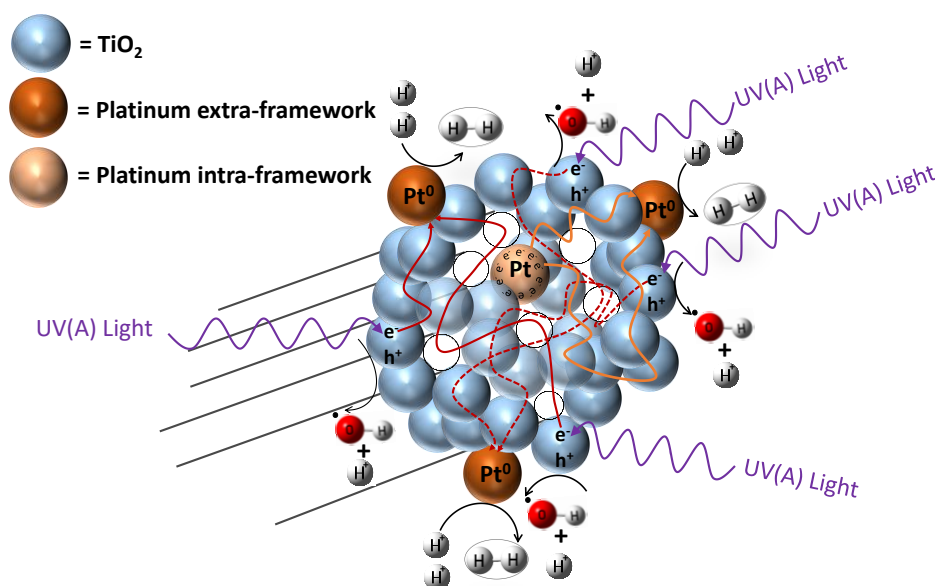


Figure 5.1 Schematic diagram of a TiO₂ photocatalyst with added Pt. Pt sites are shown inside and outside semiconductor particles. Inner sites are dominant electron reservoirs enhancing hydrogen production.

5.3 Experimental Methods

The photocatalysts of the present study were doped with platinum using incipient wetness impregnation, wet impregnation and a sol-gel method. The TiO₂ semiconductors synthesized and doped with Pt exhibit a light grey colour for small Pt loadings (<1.00 wt. %) and a dark grey colour for high Pt concentrations (>1.00 wt. %) These photocatalysts were characterized using BET analysis, UV spectroscopy with diffuse reflectance, and X-

ray diffraction (XRD). Furthermore, a near UV lamp was employed during the runs in the Photo-CREC-Water II Reactor. Various methodologies used for photocatalyst preparation as well as for hydrogen production experiments are described in the upcoming sections of this thesis.

5.3.1 Photocatalyst Preparation of Pt/TiO₂

5.3.1.1 Incipient Wetness Impregnation Method

An incipient wetness impregnation technique can be used to prepare a modified Pt–TiO₂ photocatalyst. The material utilized as a support was a Degussa P25 semiconductor of titanium dioxide (TiO₂) from Evonik Degussa Co. Platinum was added on the outer surface of the TiO₂ particles by employing a 99.90 wt. % H₂PtCl₆ xH₂O reagent from Sigma-Aldrich Co. This prepared material was used as a reference, for assessing the performance of two other synthesized photocatalysts of the present study.

5.3.1.2 Wet Impregnation Method

The wet impregnation method was developed by incorporating 2.00 grams of Degussa P25 (TiO₂) in a solution of 10.00 mL deionized water, under continuous stirring. The doping solution was prepared with a dihydrogen-dinitro-sulphate platinate solution (H₂Pt NO₂ SO₄) at different concentrations. This was done to obtain platinum loadings on TiO₂ in the 0.42–1.70 wt. % range. This solution was added to the TiO₂, and mixed for one hour. A reducing agent of 0.03 M of sodium borohydride (NaBH₄) was then employed. The resulting solution was mixed for another 10 h. Then, the obtained solids were filtered, dried at 110 °C for 18 h, and finally calcined at 450 °C for 3 h.

5.3.1.3 Sol-Gel Method

Regarding this method, two different routes, labelled sol-gel A and sol-gel B, were developed.

Sol-Gel A

The synthesis of the sol-gel A was achieved using titanium (IV) isopropoxide (C₁₂H₂₈O₄Ti, Sigma-Aldrich 97.00%), isopropanol (C₃H₇OH, J.T. Baker 99.90%), and dihydrogen

dinitro-sulphate platinate(II). 70.00 mL of isopropanol reagent (organic solvent) was poured into a flask, under nitrogen bubbling flow. Then, the titanium (IV) isopropoxide was added dropwise. Once this step was completed, the resulting blend was mixed for 20 min to remove all the dissolved oxygen. Then, 7.50 mL of the dihydrogen dinitro-sulphate palatinate(II) solution were added dropwise. The resulting solution was allowed to stand for 20 min. $\text{H}_2\text{Pt}(\text{NO}_2)_2\text{SO}_4$ concentrations were carefully selected to obtain Pt loadings of 0, 0.42, 0.82 and 1.70 wt. %. Finally, and to reduce platinum into its metal state, a 0.03 M of sodium borohydride (NaBH_4) reducing solution was used. The prepared solution was placed in a 1200 W microwave unit for 30 min, at 215 °C and allowed to rest for 1 h. The resulting slurry was filtered and washed with distillate water. The obtained wet-paste was dried out at 110 °C for 18 h and later calcined at 450 °C for 3 h.

Sol-Gel B

The sol-gel B method first involves the dissolution of 2.00 g of Pluronic F127 in 40 mL of ethanol ($\text{CH}_3\text{CH}_2\text{OH}$) and 3.30 g of hydrochloric acid (37 wt. % purity) as reported in the previous chapter. Once this is achieved, 0.63 g of citric acid were added and mixed continuously at room temperature for 2 h. When this step was completed, 2.85 g of titanium (IV) isopropoxide were added to the resulting blend. This method was used to prepare the mesoporous titanium dioxide. This sol-gel synthesis process gives a Pt loaded TiO_2 with the following valuable properties: 150 m^2/g of specific surface area, 10–40 nm pore sizes, 0.68 cm^3/g pore volume, 100% anatase content, 10 nm Pt crystallite sizes.

5.4 Photocatalytic Reactor

Figure 5.2 reports a schematic diagram of the Photo-CREC Water II Reactor and its accessories for hydrogen production used in the present study. This modified Photo-CREC Water II Reactor is a “well mixed” batch unit that produces hydrogen. Figure 5.2 also shows the overall unit configuration: a sealed stirred tank chamber connected in series with a tubular photocatalytic reactor. The Photo-CREC Water II Reactor includes the additional following components: (i) a BLB Lamp; (ii) a Pyrex glass tube; (iii) a UV-opaque polyethylene cylinder; (iv) fused-silica windows; (v) a centrifugal pump; (vi) a H_2 storing/mixing tank; (vii) a gas sampling port; (viii) a slurry sampling port; (ix) a purging

gas injector; (x) a jet driving mixing port; (xi) a self-driven mixing impeller and (xii) a draining gas valve.

The experimental runs of the present study were performed by employing the following: (a) 6 L of distillate deionized water; (b) 0.90 g of photocatalyst and (c) 2 M of H₂SO₄ to adjust the solution pH to 4.00 ± 0.05 . As well, the near UV lamps of the present study were characterized using a Solatell Spectroradiometer capable of measuring UV intensities in the 1×10^{-7} to 2×10^{-2} W/cm² range. This was used to determine the energy flux of the BLB lamp absorbed in the Photo-CREC Water II Reactor unit. Additional details regarding lamp characterization and macroscopic balances are reported in Appendix B. Table 5.1 reports the flux of absorbed photons for each photocatalyst using the macroscopic balance methodology described in Appendix F and E.

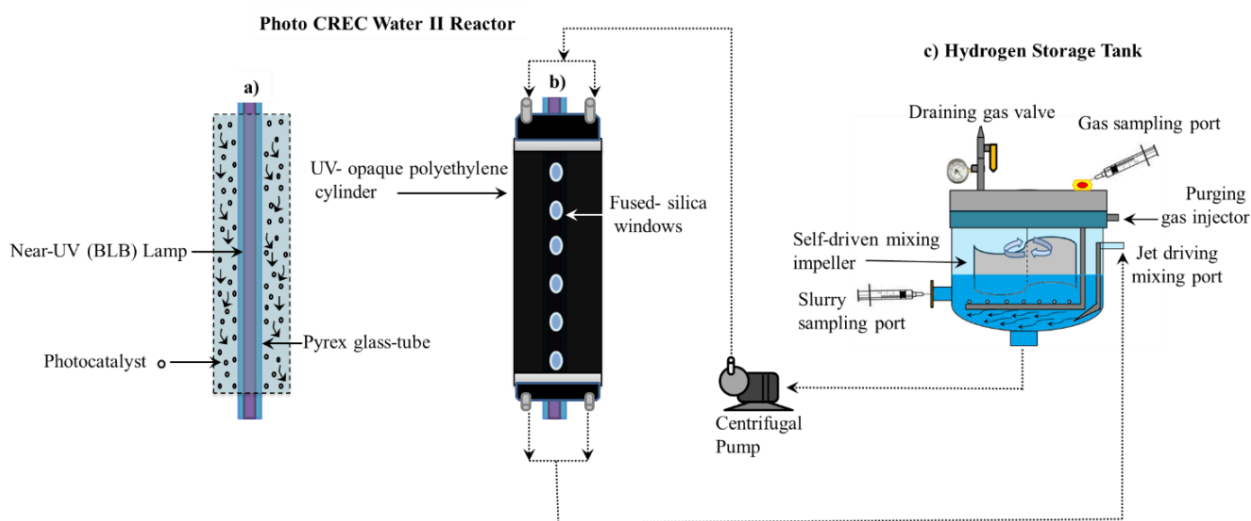


Figure 5.2 Schematic diagrams of the Photo-CREC Water II Reactor with a H₂ mixing/storage tank: (a) Longitudinal cross-section of the Photo-CREC Water II unit showing the downflow slurry circulation in the annular channel; (b) overall view of Photo-CREC Water II showing windows and recirculation pump and (c) hydrogen storage tank with its components.

Table 5.1 Absorbed photon fluxes for the various photocatalysts of the present study. P_i , represents the incident radiation whereas P_t , is the transmitted radiation and P_a is the absorbed radiation.

Photocatalyst Type	P_i (Einstein/h)	P_t (Einstein/h)	P_{bs} (Einstein/h)	P_a (Einstein/h)	Percent Absorption Efficiency
<i>Incipient Impregnation, 1.00 wt. % Pt</i>	0.0187	0.0023	0.0007	0.0157	84%
<i>Wet Impregnation, 1.70 wt. % Pt</i>	0.0180	0.0019	0.0005	0.0156	87%
<i>Sol-gel A, 1.70 wt. % Pt</i>	0.0124	0.0013	0.0005	0.0106	85%
<i>Sol-gel B, 2.50 wt. % Pt</i>	0.0107	0.0003	0.0001	0.0103	96%

Table 5.1 shows that there is no significant difference between the photon absorption efficiencies of the various photocatalysts prepared either via incipient and wet impregnation. These absorption efficiencies remain in the 84–87% range. On the other hand, one can observe that the sol-gel synthesized mesoporous Pt photocatalysts displayed slightly higher efficiencies, with these small differences being attributed to the different surface morphology properties of the synthesized photocatalysts.

5.5 Analytical Methods

To quantify the chemical species (ethanol, acetaldehyde, methane, ethane, carbon monoxide, carbon dioxide and hydrogen) present during every run, combined FID and TCD GC analysis were implemented. Carbon balances developed using these species data are reported in Appendix G.

5.6 Photocatalyst Characterization

Three photocatalyst characterization techniques were employed in this study: (a) Specific surface area determined using a Micromeritics, ASAP 2010 unit, through nitrogen adsorption; (b) The band gap energy (E_{bg}) obtained from diffuse reflectance measurements (Cary 500 UV-Vis NIR Varian spectrophotometer) and (c) The x-ray diffraction (XRD)

developed by employing a diffractometer RIGAKU Ultima IV and a multi-purpose diffractometer.

It is, in this respect, anticipated that semiconductors with larger specific surface areas doped with novel metals may lead to a higher density of metal active sites. Hence, this could enhance hydrogen evolution. Thus, specific surface areas were calculated using the Brunauer–Emmett–Teller (BET) method while the pore volume distributions were measured with the Barrett–Joyner–Halenda (BJH) model.

Figure 5.3 reports both adsorption and desorption isotherms type V for the Pt–TiO₂ prepared via wet impregnation with 1.70 wt. % Pt loading.

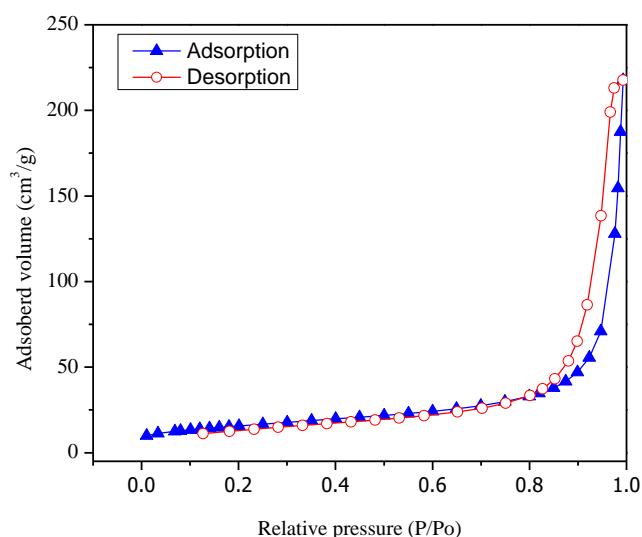


Figure 5.3 Adsorption–desorption isotherms for Pt–TiO₂. Pt was added by wet impregnation.

Figure 5.4 shows the adsorption isotherm for the sol-gel A synthesized TiO₂ with 1.70 wt. % Pt. One can notice that the sol-gel A synthesized semiconductors display a type IV isotherm.

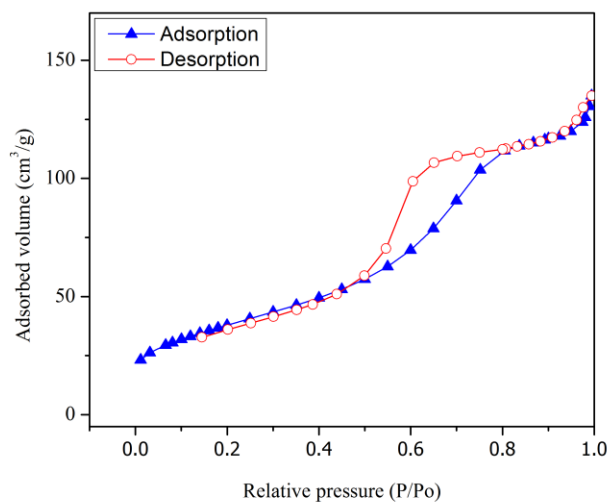


Figure 5.4 Adsorption–desorption of N₂ on TiO₂ with 1.70 wt. % Pt prepared via the sol-gel A method.

Table 5.2 reports the specific surface area of the photocatalysts synthesized by different methods.

Table 5.2 Specific surface areas for the prepared photocatalysts.

	1.00 wt. % Pt–Degussa P25 (Incipient Wetness Impregnation)	1.70 wt. % Pt-sol-gel (Method A)	2.50 wt. % Pt-sol-gel (Method B)
Specific Surface Area (m ² /g)	52	116	150

One can also observe a 52 m²/g for the specific surface area of the Degussa P25 impregnated via incipient wetness with a Pt precursor. This specific surface area increases progressively to 116 and 150 m²/g for sol-gel A and sol-gel B, respectively. These findings point towards higher promoted specific surface areas for platinum-sol-gel prepared photocatalysts.

Figure 5.5 gives a Barrett–Joyner–Halenda plot that shows the pore size distribution of the Pt–TiO₂. One can clearly see in this figure that the doped Pt–TiO₂ obtained via incipient wet impregnation and the sol-gel A and sol-gel B TiO₂ doped with Pt differ in both pore size distribution and pore volume.

In this respect, and as shown in Figure 5.5, the Pt–TiO₂ obtained via incipient impregnation shows a 4.0 nm average pore size, while the Pt added on sol-gel prepared via method A displays a 6.5 nm average pore size.

Furthermore, the Pt-doped photocatalyst synthesized using sol-gel method B shows a bimodal pore size distribution with dominant 12.0 nm and 43.0 nm pore sizes. As reported in Figure 5.5, one can notice for the Pt on sol-gel prepared photocatalysts, and especially for the Pt on sol-gel prepared by method B, there is an increased volume fraction in the mesoporous pore range.

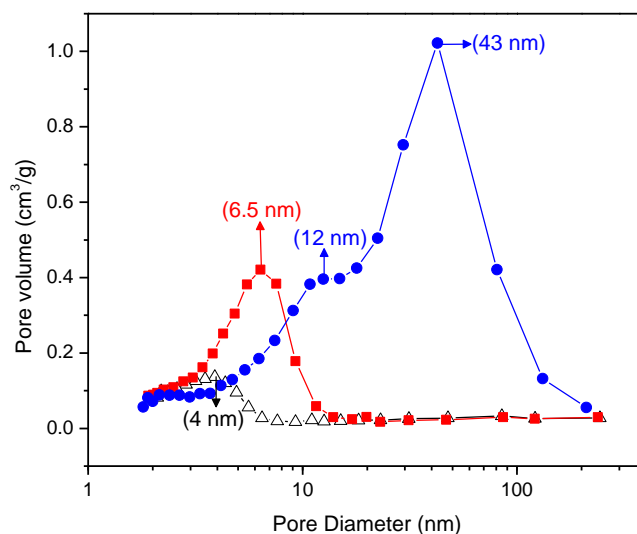


Figure 5.5 Pore size distribution of the Pt–TiO₂ prepared via incipient wetness impregnation; (●) mesoporous TiO₂ thermally treated at 550 °C (sol-gel B), (■) mesoporous TiO₂ calcined at 450 °C (sol-gel A), (Δ) Degussa P25 impregnated with 1.00 wt. % Pt and calcined at 450 °C.

The band gap energy can be estimated using the Kubelka–Munk equation and the Tauc plot. Figure 5.6 reports the Tauc plots for sol-gel materials with different platinum loadings.

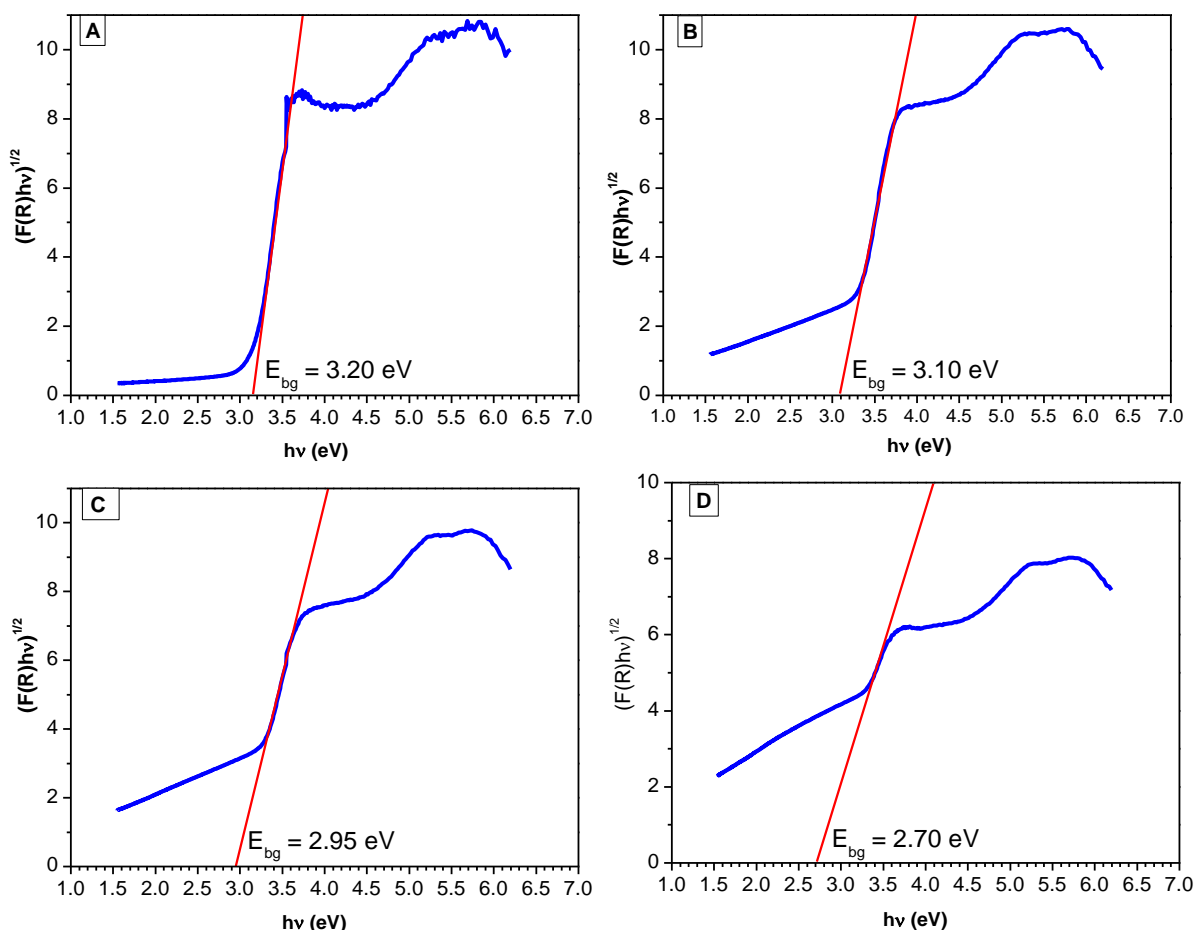


Figure 5.6 Tauc Plots for sol-gel A based TiO₂ photocatalysts calcined at 450 °C: (A) TiO₂ sol-gel A; (B) TiO₂ sol-gel A with 0.42 wt. % Pt; (C) TiO₂ sol-gel A with 0.82 wt. % Pt; (D) TiO₂ sol-gel A with 1.70 wt. % Pt. E_{bg} was calculated using the intersection of Tauc's line with the abscissa axis; $(\alpha h\nu)^{1/2} \approx h\nu - E_{bg}$.

Based on the red line slope extrapolation in Figure 5.6, one can calculate the band gap energy with the higher platinum loading photocatalysts yielding reduced band gaps. These band gaps range from 3.20 eV (Pristine TiO₂ via sol-gel A and B) to 2.70 eV (TiO₂-1.70 wt. % Pt). Additionally, one can see that the Pt doped on TiO₂ via sol-gel yields

semiconductors with the lowest band gap. This reduction of the band gap energy allows one to speculate about the enhanced activation of these semiconductors under visible light.

Figure 5.7 reports the effect of the platinum loading on the photocatalyst band gap, for the photocatalysts prepared by sol-gel. One can observe that the band gap for the Degussa P25 impregnated via incipient wetness with a Pt precursor, remains in the 2.75–3.20 eV range. Moreover, Pt–TiO₂ photocatalysts being prepared using both sol-gel methods leads to a significant reduction of the band gap from 3.20 to 2.70 eV as a function of the platinum loading.

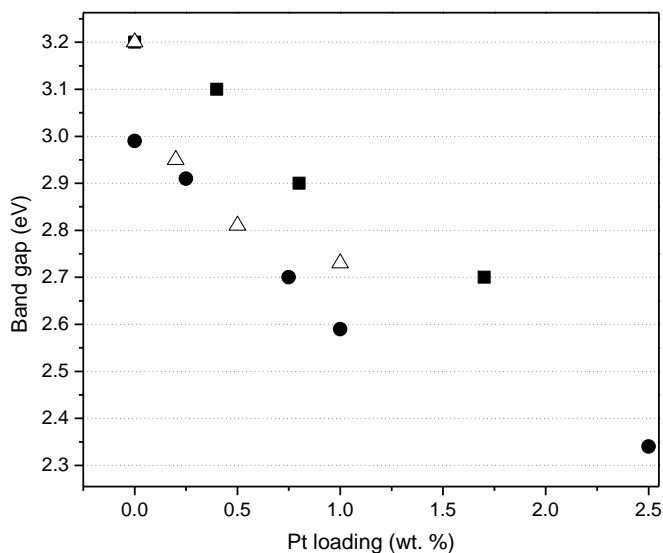


Figure 5.7 Influence of platinum loading on the band gap of the photocatalysts: (●) TiO₂—Mesoporous, thermally treated at 550 °C (sol-gel B) [8], (■) TiO₂—Mesoporous, calcined 450 °C (sol-gel A), (△) Degussa P25 impregnated and calcined at 450 °C. Note: The band gap for Degussa P25 without Pt loaded was recorded at 3.20 eV.

Thus, it is confirmed, as reported in Figure 5.7, that for the various platinum-loaded TiO₂ photocatalysts of the present study, Pt has a consistent beneficial effect, reducing the band gap energy.

Figure 5.8 reports a typical XRD diffractogram for TiO₂-based materials prepared by either wet or incipient impregnation. In addition, one can recognize the characteristic peaks of the two crystalline phases of titanium dioxide (anatase and rutile), with platinum also being included.

Figure 5.8 reports a change of the different XRD peaks for the wet and incipient platinum impregnated TiO₂-Degussa P25. One can notice that both photocatalysts display rutile (110) crystal plane and that this giving the characteristic 27° Bragg angle band. One can also observe, as reported in Table 5.3, that for the various sol-gel Pt-TiO₂, there is no recordable 27° Bragg angle. As a result, this shows that the various synthesized sol-gel Pt-TiO₂ are free of rutile (110) facet.

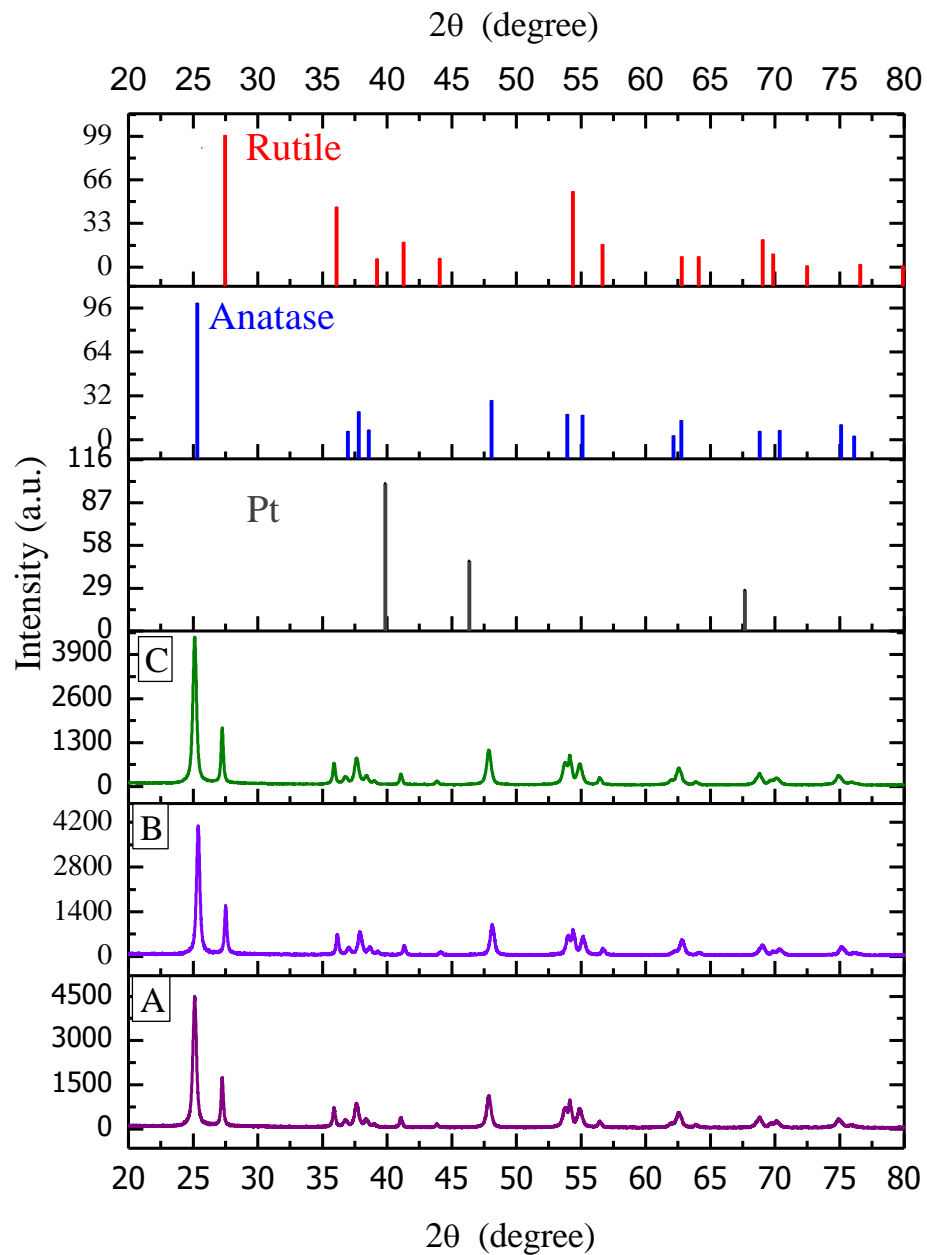


Figure 5.8 X-ray diffractogram for: (A) TiO₂, Degussa P25; (B) wet impregnated with 1.70 wt. % Pt on TiO₂ Degussa P25; (C) incipiently impregnated with 1.00 wt. % Pt on TiO₂ Degussa P25.

Table 5.3 Relative composition of rutile and anatase in the prepared photocatalysts as assessed using the 25° Bragg angle and the 27° Bragg angle bands in the 2 θ scale.

<i>Photocatalyst</i>	<i>Anatase (%)</i>	<i>Rutile (%)</i>	<i>Rutile (110)/Anatase (101)</i>
<i>Degussa P25</i>	80	20	0.25
<i>Incipient Impregnation, 1.00 wt. % Pt</i>	80	20	0.25
<i>Wet Impregnation, 1.70 wt. % Pt</i>	80	20	0.25
<i>Sol-gel (Method A), 1.70 wt. % Pt</i>	100	0	0
<i>Sol-gel (Method B), 2.50 wt. % Pt</i>	100	0	0

5.7 Photocatalytic Reaction Mechanism for Hydrogen Production

Experiments of hydrogen production using heterogeneous photocatalysis were carried out using the modified Photo-CREC Water II Reactor. There was a minimum of three repeats for each experimental condition considered. Hydrogen generation runs were performed at room temperature and pressure, under an inert argon atmosphere, with a 2.00% v/v ethanol concentration, and with a pH of 4.00 ± 0.05 .

Figure 5.9 reports the cumulative hydrogen produced using the wet impregnated photocatalyst with platinum loadings in the 0.42 to 1.70 wt. % range. Photocatalyst loading in all experiments was 0.15 g/L.

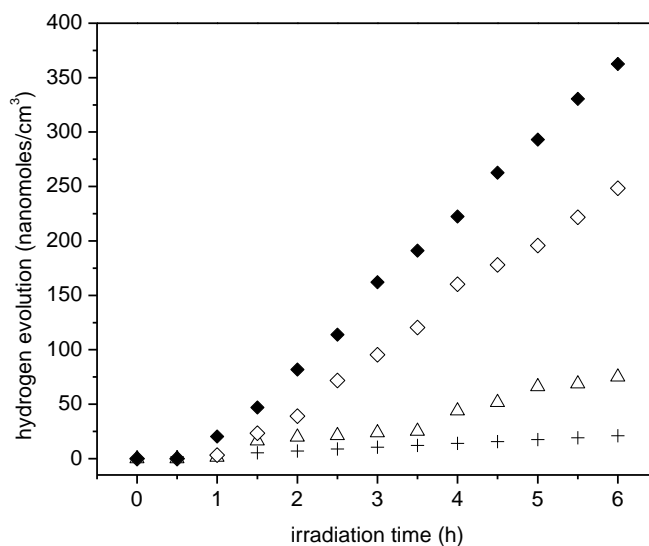


Figure 5.9 Cumulative hydrogen formation under an argon atmosphere for various photocatalysts: (♦,◇) Pt–TiO₂ prepared via incipient wetness impregnation with 1.70 wt. % and 0.82 wt. % of Pt loadings on TiO₂ Degussa P25, (Δ) Degussa P25 and (+) Blank run [no photocatalyst]. Photoreaction conditions: pH = 4.00 ± 0.05, 2.00% v/v ethanol, photocatalyst loading: 0.15 g/L. Standard deviation for repeats was ±4.5%.

It can be noticed in Figure 5.9 that the cumulative hydrogen production increases both with irradiation time and platinum loading. This is noteworthy after 1 h of experiment. The first 30 minutes can be established as induction period due to no hydrogen molecules were detected. Thus, it appears that augmenting the Pt loadings from 0.82 wt. % to 1.70 wt. % leads to higher Pt surface density sites and provides increased electron storage capacity. This augmented electron storage capacity helps in reducing electron-hole recombination, contributing to H⁺ conversion into H•.

Furthermore, one can observe from these experiments that there is a consistent linear trend with irradiation time and the cumulative hydrogen being produced. This shows zero-order hydrogen formation kinetics with no detectable activity decay. Thus, it can be concluded that all the prepared photocatalysts are very stable, with performance unaffected by the extent of irradiation.

Figure 5.10 reports the cumulative hydrogen production for TiO₂ prepared using sol-gel method A. One can observe an increase of hydrogen production when using TiO₂ prepared via the sol-gel A method and compared to that obtained with Degussa P25. Furthermore, one can notice a further enhancement of the hydrogen production with the Pt–TiO₂ prepared via sol-gel A with 1.70 wt. % of Pt loadings. This cumulative hydrogen production is again of zero order in all cases, with no observable photocatalyst deactivation.

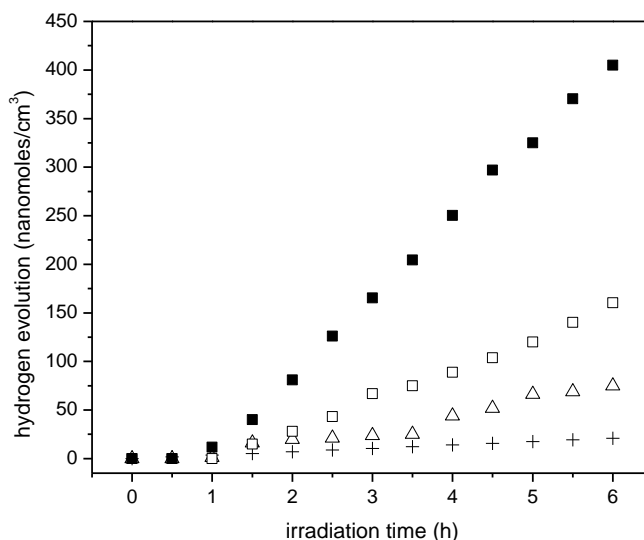


Figure 5.10 Cumulative hydrogen formation under an argon atmosphere for various photocatalysts using: (■) Pt–TiO₂ prepared via sol-gel A with 1.70 wt. % of Pt loadings, (□) TiO₂ prepared via sol-gel A and (Δ) Degussa P25, (+) Blank run [no photo catalyst loaded]. Photoreaction conditions: pH = 4.00 ± 0.05, 2.00% v/v ethanol, photocatalyst loading: 0.15 g/L. Standard deviation for repeats was ±5%.

Figure 5.11 shows the cumulative hydrogen production for the Pt–TiO₂ synthesized photocatalysts using the sol-gel Method B. The first 30 minutes can be established as induction period due to no hydrogen molecules were detected. One can recognize that the observed linear trend is consistent with the photocatalyst prepared using the sol-gel Method A and with respect to Degussa P25.

Additionally, one can notice that Pt addition leads to a further improvement of the hydrogen production. Hence, consistent increase of hydrogen production with Pt loadings is observed. This cumulative hydrogen production is again of zero order with no observable photocatalyst deactivation.

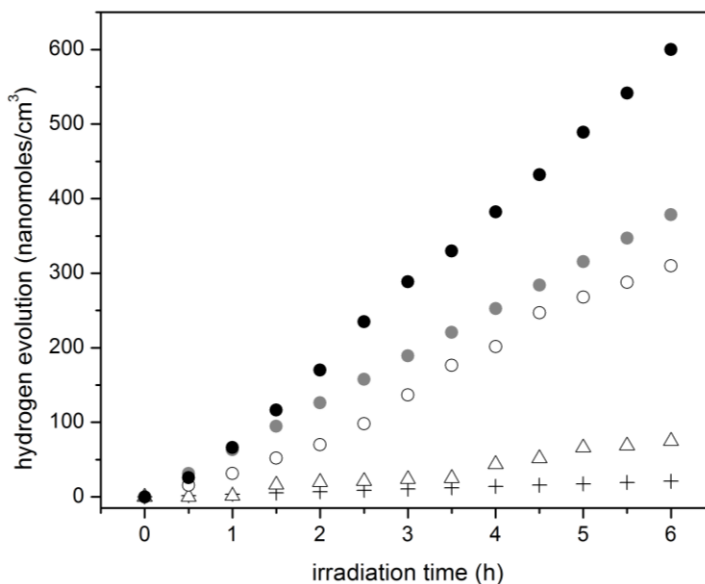


Figure 5.11 Cumulative hydrogen formation under an argon atmosphere for various photocatalysts using: (●) (●) (○) Pt–TiO₂ prepared via sol-gel B with 2.50 wt. % and 1.00 wt. % Pt, (Δ) Degussa P25, (+) Blank run [no photocatalyst]. Photoreaction conditions: pH = 4.00 ± 0.05, 2.00% v/v ethanol, photocatalyst loading: 0.15 g/L. Standard deviation for repeats was ±5%.

If one compares the cumulative hydrogen production of the 1.70 wt. % Pt–TiO₂ of Figure 5.9 with respect to that of Figure 5.10, one can observe that sol-gel A displayed a mildly increased hydrogen production versus the one prepared via incipient impregnation: from 350 nanomoles/cm³ to 400 nanomoles/cm³.

Furthermore, if one considers the hydrogen production when using the 1.00 wt. % Pt–TiO₂ sol-gel B (refer to Figure 5.11), one can see that this photocatalyst yields essentially the same amount of hydrogen as the one with a higher Pt loading (1.70 wt. % Pt–TiO₂ sol-gel Method A, refer to Figure 5.10). As well, after 5 h of irradiation, a further increase of Pt

up to 2.50 wt. % in sol-gel B gives a valuable 600 nanomoles/cm³ of cumulative hydrogen after 6 h.

5.8 Hydrogen Formation with Ethanol Scavenger

Hydrogen formation with the consumption of an ethanol scavenger, using a Pt–TiO₂ photocatalyst, can be described as the contribution of two photocatalyst sites: (a) a TiO₂ site promoting oxidation reactions; and (b) a TiO₂ site enhanced by Pt promoting hydrogenation (reduction) reactions. Hence, both oxidation and reduction networks are of series-parallel type. This series-parallel network character can be assigned to: (a) the variability of irradiated photons and thus the h⁺ changing density on TiO₂; and (b) the changing extent of stored electron density in the Pt sites.

Therefore, as described in Figure 5.12, the resulting series-parallel network is of the redox type [9]. Included in this process is the formation of hydrogen peroxide. Additional details of various oxidation and reduction steps are provided in Table 4 and Table 5, respectively.

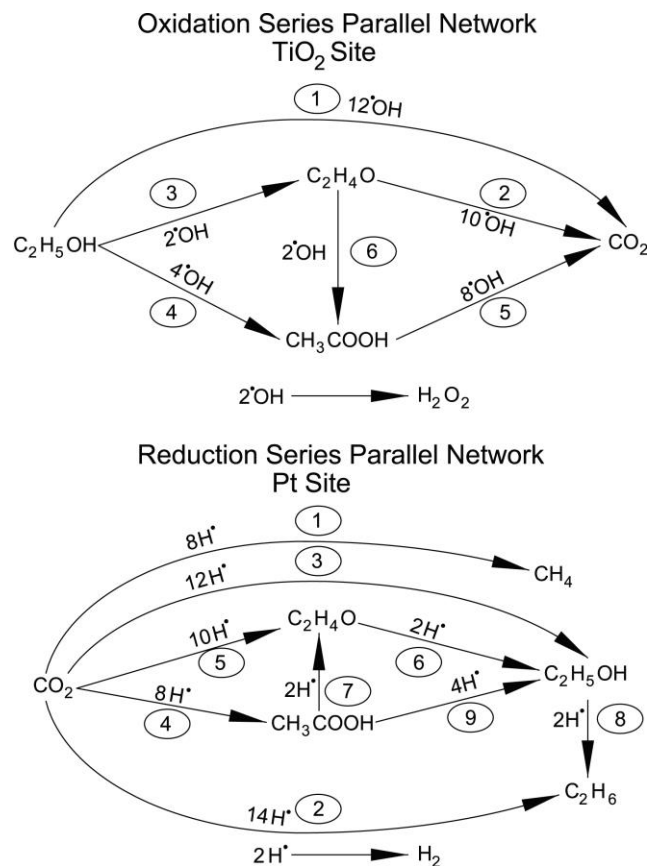


Figure 5.12 Oxidation–reduction network promoted by TiO₂ and Pt sites in the Pt–TiO₂ photocatalysts.

Figure 5.13 reports the progressive and consistent methane formation for various Pt-doped photocatalysts prepared using incipient impregnation, wet impregnation and sol-gel. The Degussa P25 photocatalyst without Pt addition is reported as a reference.

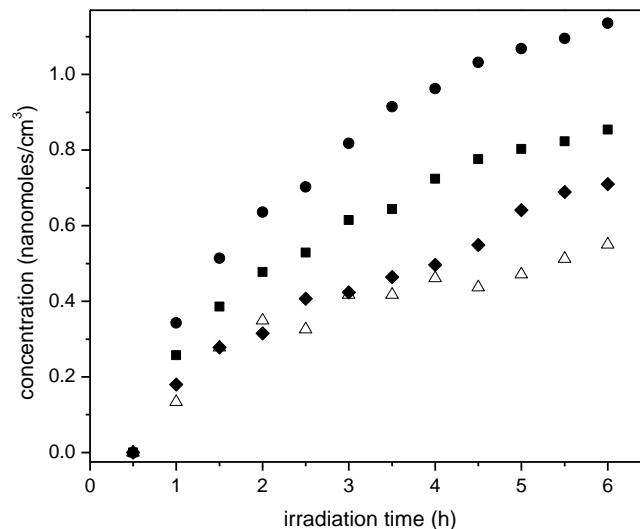


Figure 5.13 Methane increase with irradiation time for: (●) 2.50 wt. % Pt-TiO₂ (sol-gel B), (■) 1.70 wt. % Pt-TiO₂ (sol-gel A), (◆) 1.70 wt. % Pt-TiO₂ (wetness impregnation) and (Δ) Degussa P25. Standard deviation for repeats is within $\pm 7.5\%$.

One can see in Figure 5.13 that methane formation augments yet tends to stabilize with irradiation time. This is a consistent trend for all the photocatalysts of the present study. Thus, these findings highlight the photocatalytic reduction character of the proposed reaction network. Furthermore, it is observed that 1.70 wt. % wet impregnation, and 1.70 wt. % Pt sol-gel A photocatalysts yield comparable methane concentrations. These methane concentrations are however, surpassed when 2.50 wt. % Pt on TiO₂ (sol-gel B) is considered. This case shows an enhanced hydrogenating activity at higher Pt loadings, with this being consistent with the results reported in Figure 5.10.

Figure 5.14 reports ethane cumulative formation with irradiation time for the various photocatalysts of the present study.

Figure 5.14 shows that ethane increases linearly with irradiation time. Thus, it appears that ethane is a main reduction final product of the proposed series-parallel network. Again, here the highest ethane concentration levels were obtained using the sol-gel B with the 2.50 wt. % Pt loadings. In other words, it can be concluded that the photocatalytic conversion

of the ethanol scavenger is significantly affected by several reduction steps leading to the formation of both methane and ethane.

On the other hand, Figure 5.15 reports the acetaldehyde obtained, with acetaldehyde formation increasing progressively with irradiation time. This described trend was observed consistently for all the studied photocatalysts with added Pt.

Thus, as shown in Figure 5.15, photocatalysis with loaded Pt leads to the oxidation of the ethanol scavenger. One should notice in this respect, that acetaldehyde is a characteristic representative species of primary oxidation products of the network oxidation branch, as described in Table 5.4. One can notice in Figure 5.15 that the 1.70 wt. % Pt-sol-gel A yields the highest acetaldehyde concentrations, consistent with higher overall photocatalytic activity.

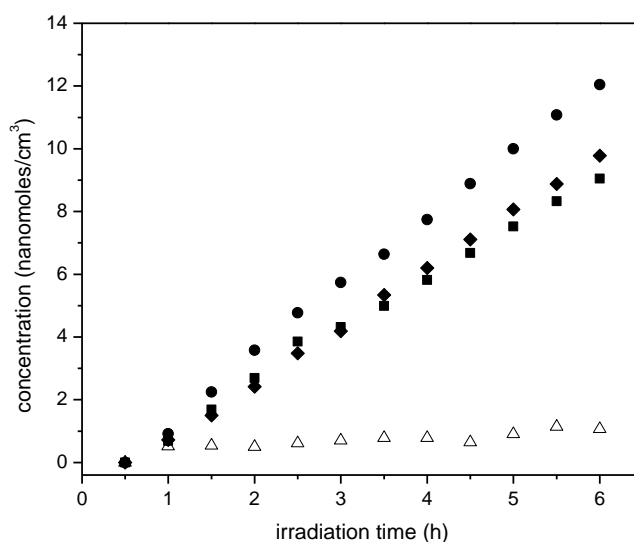


Figure 5.14 Ethane increase with irradiation time for: (●) 2.50 wt. % Pt-TiO₂ (sol-gel B), (■) 1.70 wt. % Pt-TiO₂ (sol-gel A), (◆) 1.70 wt. % Pt-TiO₂ (wetness impregnation) and (Δ) Degussa P25. Standard deviation for repeats is within $\pm 7\%$.

Table 5.4 Proposed oxidation reactions over TiO₂ sites.

Step	Reaction
I.1	$C_2H_5OH + 12^{\bullet}OH \rightarrow 2CO_2 + 9H_2O$
I.2	$C_2H_4O + 10^{\bullet}OH \rightarrow 2CO_2 + 7H_2O$
I.3	$C_2H_5OH + 2^{\bullet}OH \rightarrow C_2H_4O + 2H_2O$
I.4	$C_2H_5OH + 4^{\bullet}OH \rightarrow CH_3COOH + 3H_2O$
I.5	$CH_3COOH + 8^{\bullet}OH \rightarrow 2CO_2 + 6H_2O$
I.6	$C_2H_4O + 2^{\bullet}OH \rightarrow CH_3COOH + H_2O$

Table 5.5 Proposed reduction reactions on Pt sites.

Step	Reaction
II.1	$CO_2 + 8H^{\bullet} \rightarrow CH_4 + 2H_2O$
II.2	$2CO_2 + 14H^{\bullet} \rightarrow C_2H_6 + 4H_2O$
II.3	$2CO_2 + 12H^{\bullet} \rightarrow C_2H_5OH + 3H_2O$
II.4	$2CO_2 + 8H^{\bullet} \rightarrow CH_3COOH + 2H_2O$
II.5	$2CO_2 + 10H^{\bullet} \rightarrow C_2H_4O + 3H_2O$
II.6	$C_2H_4O + 2H^{\bullet} \rightarrow C_2H_5OH$
II.7	$CH_3COOH + 2H^{\bullet} \rightarrow C_2H_4O + H_2O$
II.8	$C_2H_5OH + 2H^{\bullet} \rightarrow C_2H_6 + H_2O$
II.9	$CH_3COOH + 4H^{\bullet} \rightarrow C_2H_5OH + H_2O$

In order to validate the proposed redox mechanism, various detectable chemical species (methane, ethane, acetaldehyde, ethanol, hydrogen peroxide, hydrogen) were identified and quantified both in the gas phase as well in the liquid phase. This was done at various stages (every 30 min of the 6-h irradiation period). This approach was consistently used in all runs utilizing the various photocatalysts of the present study.

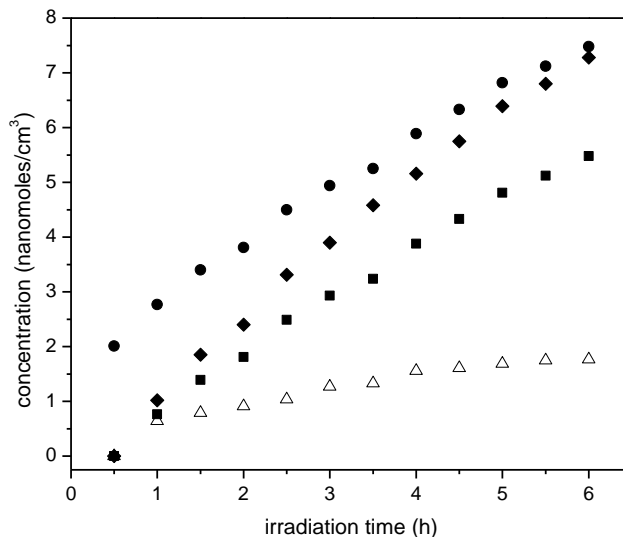


Figure 5.15 Acetaldehyde increase with irradiation time: (●) 2.50 wt. % Pt-TiO₂ (sol-gel B), (■) 1.70 wt. % Pt-TiO₂ (sol-gel A), (◆) 1.70 wt. % Pt-TiO₂ (wetness impregnation) and (Δ) Degussa P25. Standard deviation for repeats was within $\pm 6.5\%$.

Furthermore, Figure 16 reports carbon dioxide concentrations augmenting steadily with irradiation. This carbon dioxide presence in the product gases points to a complete oxidation of some ethanol contained carbons during the photocatalytic reaction.

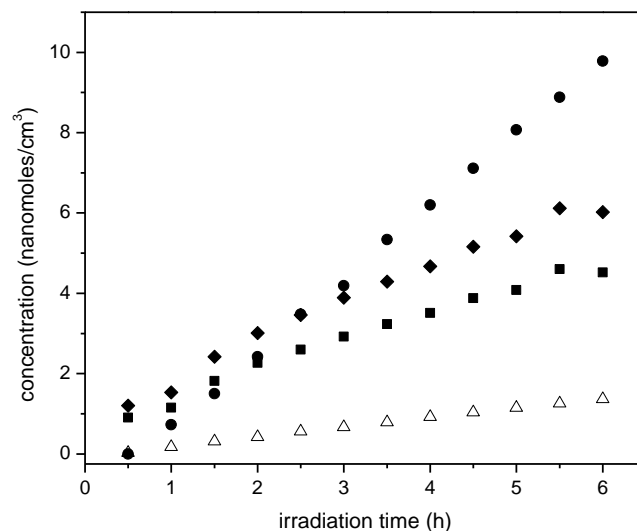


Figure 5.16 CO₂ increase with irradiation time for: (●) 2.50 wt. % Pt–TiO₂ (sol-gel B), (■) 1.70 wt. % Pt–TiO₂ (sol-gel A), (◆) 1.70 wt. % Pt–TiO₂ (wetness impregnation) and (Δ) Degussa P25. Standard deviation for repeats is within $\pm 7.5\%$.

One can notice in Figure 5.16 the formation of CO₂ even at the early stages of irradiation. This observation, combined with the concurrent formation of acetaldehyde at short irradiation times, points towards a series-parallel network for the photoconversion of water and air pollutants as reported by our research group in earlier studies [5,9].

Furthermore, and to establish the total amount of CO₂ at every stage of the irradiation process, vapour–liquid equilibrium calculations for CO₂ shall be considered, as described in Appendix H.

Figure 5.17 reports the ethanol scavenger concentration changes in the liquid phase with radiation time. These changes of ethanol with irradiation time are reported for the various Pt-doped photocatalysts of the present study.

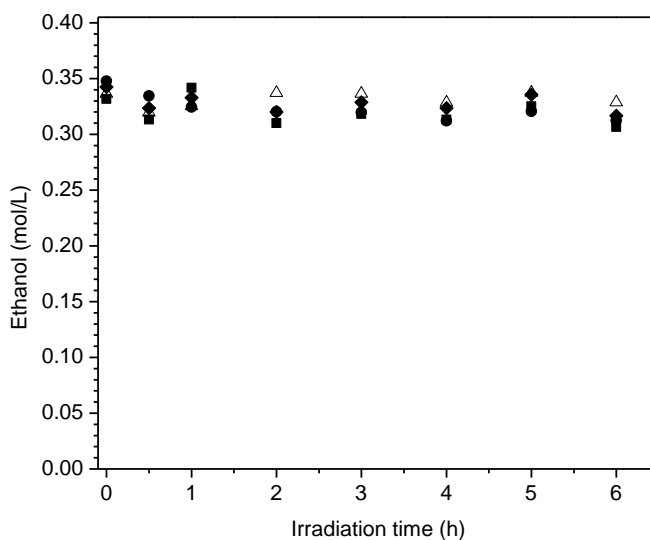


Figure 5.17 Ethanol concentration changes with irradiation time for: (●) 2.50 wt % Pt–TiO₂ (sol-gel B), (■) 1.70 wt. % Pt–TiO₂ (sol-gel A), (◆) 1.70 wt. % Pt–TiO₂ (wetness impregnation) and (Δ) Degussa P25. Notes: a) Initial ethanol concentration: 2.00% v/v or 0.345 mole/L.

One can observe in Figure 5.17 a progressive and mild decline of the ethanol scavenger concentration with irradiation time. This tendency for net ethanol to decrease is in line with an oxidation–reduction network where ethanol may be consumed and formed simultaneously.

5.9 Quantum Yields for Different Semiconducting Materials

In order to evaluate photocatalytic efficiency, a quantum yield can be defined as described with Equation (2) based on the moles of H[•] produced.

Figure 5.18 reports the quantum yield efficiencies for the various photocatalysts of the present study using sol-gel as well as wet impregnation methods. These photocatalysts contain various Pt loadings.

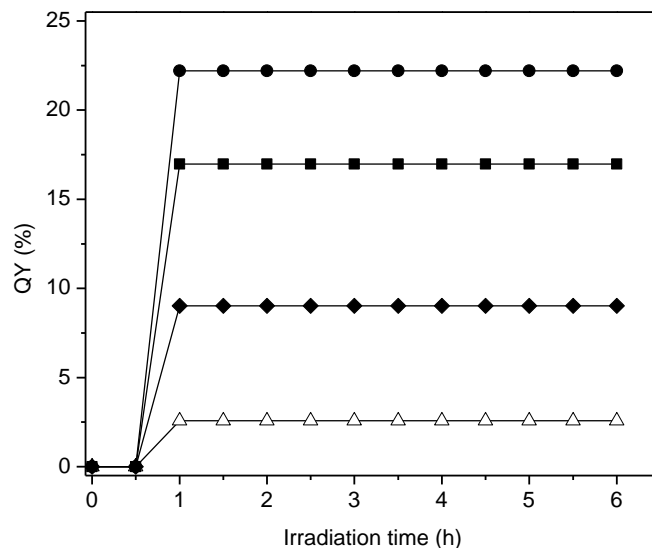


Figure 5.18 Quantum yields at various irradiation times for: (●) 2.50 wt. % Pt-TiO₂ (sol-gel B), (■) 1.70 wt. % Pt-TiO₂ (sol-gel A), (◆) 1.70 wt. % Pt-TiO₂ (wetness impregnation) and (Δ) Degussa P25. Note: TiO₂ (Degussa P25) is reported as a reference.

One can notice in Figure 5.18 that in all cases the quantum yields display a first irradiation period with progressively increasing values. Following this initial phase, quantum yields stabilize and remain essentially unchanged during the remaining 5 h of the run. These results point towards a very important property of the synthesized photocatalysts: showing no photoactivity decay. Additionally, one can observe that the increase of Pt loading augments the moles of H[•] produced. Thus, quantum yields reach valuable levels as high as 22.2% for 2.50 wt. % of Pt-TiO₂ sol-gel B catalyst.

5.10 Conclusions

The following are the major conclusions of the present chapter:

- (a) Pt-loaded photocatalysts can be prepared using both wet impregnation and sol-gel synthesis. These photocatalysts are used very effectively to produce hydrogen via water dissociation with 2.00% v/v ethanol as an organic scavenger.
- (b) The Pt–TiO₂ sol-gel photocatalysts showed a reduced 2.34 eV band gap. This reduced band gap can be attributed to the role of Pt in the modified semiconductor. In addition, the XRD for the Pt–TiO₂ sol-gel photocatalysts showed a dominant anatase content, contributing to enhanced photocatalytic activity for hydrogen production.
- (c) A common series-parallel reaction network with reduction–oxidation steps included was observed for all photocatalysts studied for hydrogen production, using ethanol as an organic scavenger. Both reduced species (methane, ethane) and oxidized species (acetaldehyde, carbon dioxide) were consistently detected in all experiments.
- (d) The proposed reaction network was found to be consistent with the overall carbon balance, accounting for various carbon-containing species involved in both oxidation and reduction steps.

5.11 References

- [1] Bahruji, H.; Bowker, M.; Davies, P.R.; Pedrono, F. New insights into the mechanism of photocatalytic reforming on Pd/TiO₂. *Appl. Catal. B Environ.* 2011, 107, 205–209, doi:10.1016/j.apcatb.2011.07.015.
- [2] Bahruji, H.; Bowker, M.; Davies, P.R.; Al-Mazroai, L.S.; Dickinson, A.; Greaves, J.; James, D.; Millard, L.; Pedrono, F. Sustainable H₂ gas production by photocatalysis. *J. Photochem. Photobiol. Chem.* 2010, 216, 115–118, doi:10.1016/j.jphotochem.2010.06.022.
- [3] Kudo, A. Recent progress in the development of visible light-driven powdered photocatalysts for water splitting. *Int. J. Hydrog. Energy* 2007, 32, 2673–2678, doi:10.1016/j.ijhydene.2006.09.010.
- [4] Galińska, A.; Walendziewski, J. Photocatalytic Water Splitting over Pt-TiO₂ in the Presence of Sacrificial Reagents. *Energy Fuels* 2005, 19, 1143–1147, doi:10.1021/ef0400619.
- [5] Escobedo Salas, S.; Serrano Rosales, B.; de Lasa, H. Quantum yield with platinum modified TiO₂ photocatalyst for hydrogen production. *Appl. Catal. B Environ.* 2013, 140–141, 523–536.
- [6] Bahruji, H.; Bowker, M.; Brookes, C.; Davies, P.R.; Wawata, I. The adsorption and reaction of alcohols on TiO₂ and Pd/TiO₂ catalysts. *Appl. Catal. Gen.* 2013, 454, 66–73, doi:10.1016/j.apcata.2013.01.005.
- [7] Yoong, L.S.; Chong, F.K.; Dutta, B.K. Development of copper-doped TiO₂ photocatalyst for hydrogen production under visible light. *Energy* 2009, 34, 1652–1661, doi:10.1016/j.energy.2009.07.024.

- [8] Guayaquil-Sosa, J.F.; Serrano-Rosales, B.; Valadés-Pelayo, P.J.; de Lasa, H. Photocatalytic hydrogen production using mesoporous TiO₂ doped with Pt. *Appl. Catal. B Environ.* 2017, 211, 337–348, doi:10.1016/j.apcatb.2017.04.029.
- [9] Escobedo, S.; Serrano, B.; Calzada, A.; Moreira, J.; de Lasa, H. Hydrogen production using a platinum modified TiO₂ photocatalyst and an organic scavenger. Kinetic modeling. *Fuel* 2016, 181, 438–449.
- [10] Cerdá, J.; Marchetti, J.L.; Cassano, A.E. Radiation efficiencies in elliptical photoreactors. *Lat. Am. J. Heat Mass Transfer.* 1977, 1, 33–63.

Chapter 6

6 Conclusions and Recommendations

As discussed in the literature review section of this PhD thesis, there is a need to design and synthesize novel materials that enhance the photocatalytic hydrogen production via water dissociation. If successful, one can foresee the development of larger externally irradiated demonstration scale photoreactors. This technology has the potential of being of benefit to isolated communities in Canada. Hydrogen could be used as an energy vector and as a mean of storing solar energy in the summer for usage in the winter. Alternatively, one could envision the usage of the photocatalytic technology for hydrogen production for the utilization of current excesses of electrical energy in Ontario and Quebec. The hydrogen produced could be used in individual vehicles powered-driven by fuel cells. As well it could be co-fed with other hydrocarbon feedstocks (e.g. methane), as a fuel, in power stations thus reducing CO₂ emissions.

To accomplish this, there is the need of progress in the area of photocatalytic reactors, to surpass the current relatively low Quantum Yields (1-10 %) achieving higher Quantum Yields (in the 45% range). This is particularly true in the case of photocatalytic hydrogen production, which requires two simultaneous or quasi-simultaneous photons to interact with two adjacent semiconductor sites. Thus, and in this respect, the present PhD dissertation, strive to open new ground for hydrogen production under near-UV irradiation using mesoporous TiO₂, doped with platinum.

This PhD also contributes to a better understanding the oxidation-reduction network for photocatalytic hydrogen production using ethanol as organic scavenger. This PhD research reports an original study on the synthesis, characterization and photoactivity of mesoporous titanium dioxide, doped with platinum for hydrogen generation, using ethanol as an organic scavenger. Moreover, the morphology of the prepared mesoporous TiO₂ are rigorously characterized using surface science techniques. The photocatalytic activity of this semiconductor is established in a Photo-CREC-Water II Reactor, using ethanol as organic scavenger (electron donor), at 2 % v/v and with a pH of 4.00. The obtained Quantum Yields (QYs) in this PhD study were a notable 0.226 (22.6%).

6.1 Conclusions

The following conclusions can be considered as the most important contributions of this PhD research:

(a) It was shown that the mesoporous TiO_2 photocatalyst can be successfully synthesized using Pluronic P123 and Pluronic F127 templates by using a sol-gel method.

(b) It was proven that the synthesized TiO_2 photocatalysts display the expected mesoporous properties which are specific surface area, pore volume and average pore diameter. This was confirmed using nitrogen adsorption, X-ray diffraction (XRD) and Scanning Electron Microscopy (SEM). The obtained nitrogen adsorption isotherms allowed showing that the mesoporous TiO_2 prepared by a sol-gel method, displays large surface areas as well as bimodal pore size distribution.

(c) It was established that the synthesized mesoporous Pt– TiO_2 photocatalysts displayed a reduced 2.34 eV band gap. This reduced band gap was attributed to the effect of Pt on the modified semiconductors. In addition, the XRD of the Pt– TiO_2 sol-gel photocatalysts showed a dominant anatase composition which appeared to contribute to the enhancement of the photocatalytic activity for hydrogen production via water dissociation.

(d) It was shown that the Pt-loaded photocatalysts prepared using both wet impregnation and sol-gel synthesis are very effective compared to the commercial Degussa P25 in the production of hydrogen via water dissociation with 2.00% v/v ethanol as an organic scavenger. Additionally, it was demonstrated that Pt plays a very important role in reducing the semiconductor band gap and trapping generated electrons.

(e) Through reactivity studies, the major importance of both the mesoporous TiO_2 architecture and the Pt loading for hydrogen production were proven. It is on this basis, and given the valuable hydrogen production rates, that further studies with mesoporous TiO_2 synthesized with Pluronic F127 were developed as documented in Chapters 4 and 5.

(f) It was demonstrated that all the synthesized semiconductors displayed a zero-order reaction for hydrogen production, with no indication of photocatalyst activity decay.

Furthermore, it was established that all the photocatalysts studied shared a series-parallel reaction network involving both reduction and oxidation. In this respect and while using ethanol as an organic scavenger, both reduced species (methane, ethane) and oxidized species (aldehyde, carbon dioxide) were consistently detected. It was also shown that this proposed reaction network was consistent with the overall carbon balance, accounting for various carbon-containing species involved in both oxidation and reduction steps.

(g) It was confirmed that the synthesized mesoporous Pt-TiO₂ semiconductors exhibited promising energy efficiencies as quantified with the QYs of 22.6 % observed for the mesoporous 2.50 wt. % Pt-TiO₂-550°C.

6.2 Future Work

There are several key issues that have emerged, based on the results examined and the observations made during this PhD thesis dissertation. Furthermore, there are areas of opportunity and possible valuable approaches for future work. Such developments are needed if one aims to extensively apply photocatalytic reactors for hydrogen production via water dissociation at the commercial scale.

In this respect, the following recommendations outline areas for possible future work:

- a) Determining the semiconductor optical properties for a range of pHs, mixing conditions and photocatalyst concentrations. This would provide insights into the influence of radiation absorption efficiency using these parameters.
- b) Characterizing particle agglomerates formed while using different scavenger concentrations, pH and photocatalyst concentration. On this basis, the photocatalyst that provides the best external specific surface area (BET), could be selected. Furthermore, by taking into account this parameter, photocatalytic hydrogen production and the effect of particle agglomeration could be accounted for.
- c) Comprehensively evaluating the synthesized photocatalyst performance of this PhD thesis under visible light irradiation using mesoporous TiO₂ decorated with other noble metals (i.e. Pd).

Appendices

Appendix A - Supplementary material of Chapter 3

Photocatalytic Hydrogen Evolutions via Water Dissociation using Mesoporous TiO₂ with Pluronic P123 and F127.

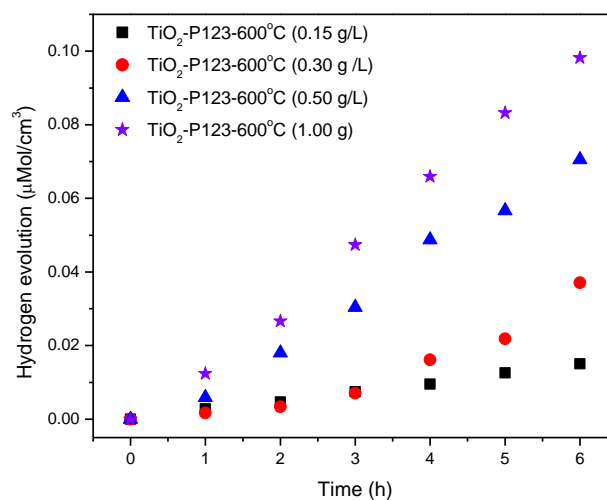


Figure A.0.1 Changes of Cumulative Hydrogen Produced at Various Irradiation Times with Different Photocatalyst Loadings. Notes: a) Mesoporous TiO₂ synthesized using Pluronic P123 and calcined at 600 °C, b) Photocatalyst irradiated with a near-UV light of $\lambda=368$ nm, c) pH = 4.00 ± 0.05 , d) 2.00 % v/v ethanol scavenger. Standard deviation for repeats are ± 5.5 %.

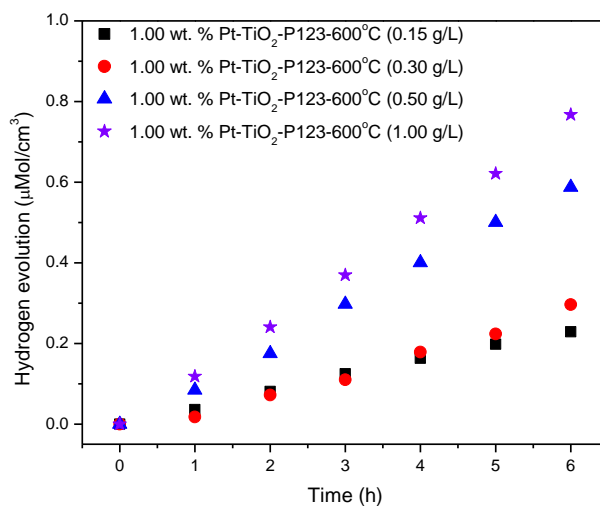


Figure A.0.2 Changes of Cumulative Hydrogen Produced at Various Irradiation Times and with Different Photocatalyst Loadings. Notes: a) Mesoporous TiO₂ synthesized using Pluronic P123, doped with 1.00 wt% Pt and calcined at 600 °C, b) Photocatalyst irradiated with a UV light of $\lambda=368$ nm, c) pH = 4.00 \pm 0.05 , d) 2.00 % v/v ethanol scavenger. Standard deviation for repeats \pm 5.5 %.

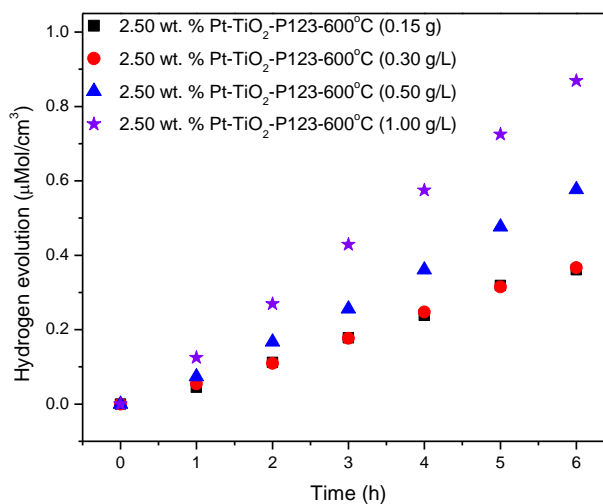


Figure A.0.3 . Changes of Cumulative Hydrogen Produced at Various Irradiation Times with Different Photocatalyst Loadings. Note: a) Mesoporous TiO₂ synthesized using

Pluronic P123, doped with 2.50 wt% Pt and calcined at 600 °C, b) Photocatalyst irradiated with a UV light of $\lambda=368$ nm, c) pH = 4.00 ± 0.05 and d) 2.00 % v/v ethanol scavenger. Standard deviation for repeats ± 5.5 %.

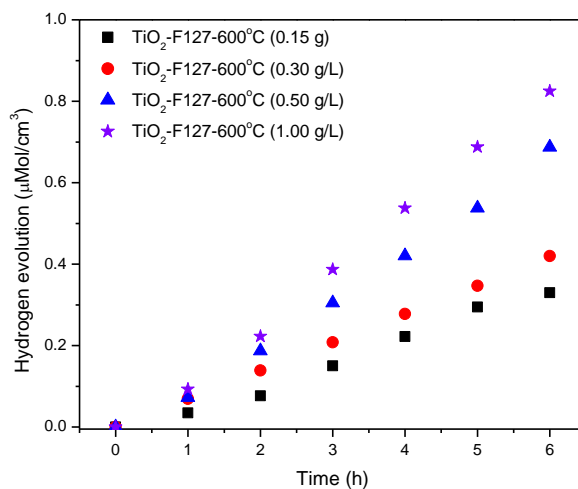


Figure A.0.4 Changes of Cumulative Hydrogen Produced at Various Irradiation Times with Different Photocatalyst Loadings. Notes: a) Mesoporous TiO₂ synthesized using Pluronic F127, calcined at 600 °C b) Photocatalyst irradiated with a UV light of $\lambda=368$ nm, c) pH = 4.00 ± 0.05 , d) 2.00 % v/v ethanol scavenger . Standard deviation for repeats ± 4.5 %.

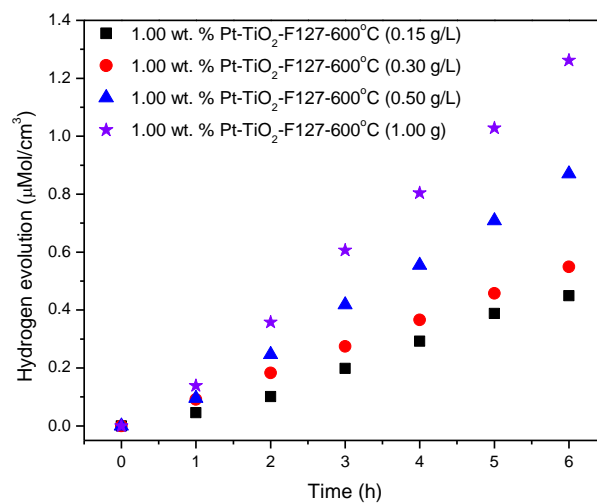


Figure A.0.5 Changes of Cumulative Hydrogen Produced at Various Irradiation Times and with Different Photocatalyst Loadings. Notes: a) Mesoporous TiO₂ synthesized using Pluronic F127, doped with 1.00 wt% and calcined at 600 °C b) Photocatalyst irradiated with a UV light of $\lambda=368$ nm) pH = 4.00 \pm 0.05 and d) 2.00 % v/v ethanol scavenger . Standard deviation for repeats \pm 4.5 %.

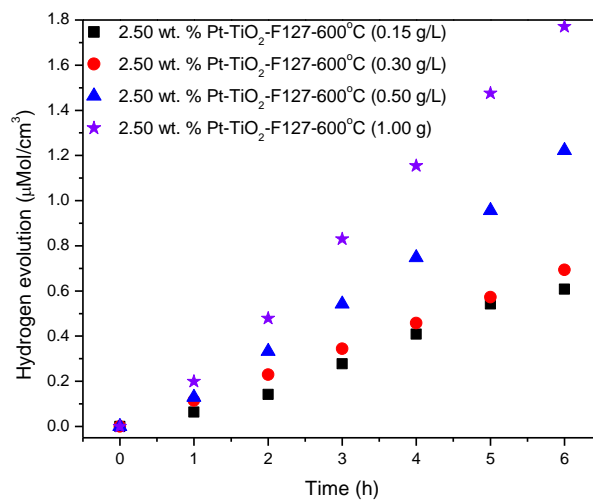


Figure A.0.6 Changes of Cumulative Hydrogen Produced at Various Irradiation Times and with Different Photocatalyst Loadings. Notes: a) Mesoporous TiO₂ synthesized using Pluronic F127, doped with 2.50 wt% Pt and calcined at 500°C, b) Photocatalyst irradiated with a UV light of $\lambda=368$ nm, c) pH = 4.00 \pm 0.05, d) 2.00 % v/v ethanol scavenger . Standard deviation for repeats \pm 4.5 %.

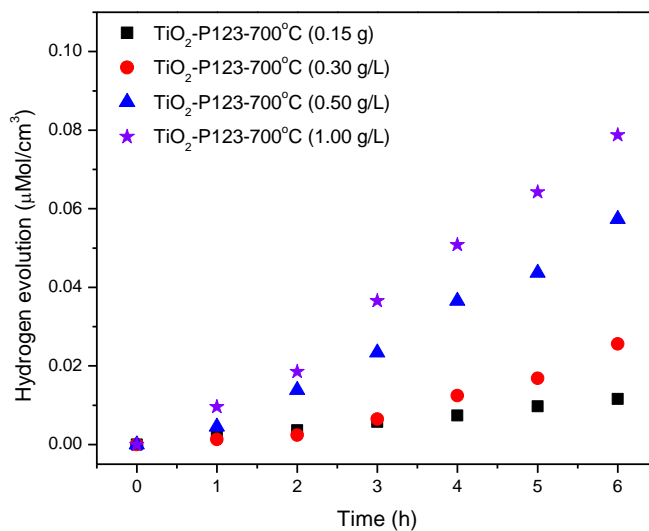


Figure A.0.7 Changes of Cumulative Hydrogen Produced at Various Irradiation Times with Different Photocatalyst Loadings. Notes: a) Mesoporous TiO₂ synthesized using Pluronic P123 and calcined at 700 °C, b) Photocatalyst irradiated with a near-UV light of $\lambda=368$ nm, c) pH = 4.00 \pm 0.05, d) 2.00 % v/v ethanol scavenger . Standard deviation for repeats are \pm 7.5 %.

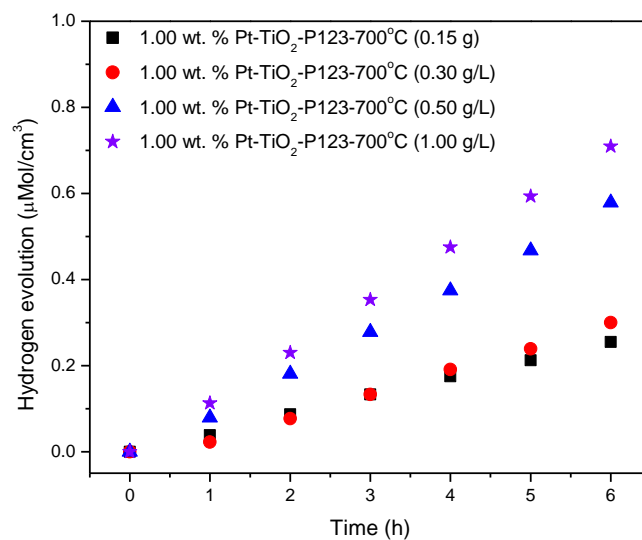


Figure A.0.8 Changes of Cumulative Hydrogen Produced at Various Irradiation Times and with Different Photocatalyst Loadings. Notes: a) Mesoporous TiO₂ synthesized using Pluronic P123, doped with 1.00 wt% Pt and calcined at 700 °C, b) Photocatalyst irradiated with a UV light of $\lambda=368$ nm, c) pH = 4.00 ± 0.05 , d) 2.00 % v/v ethanol scavenger. Standard deviation for repeats ± 7.5 %.

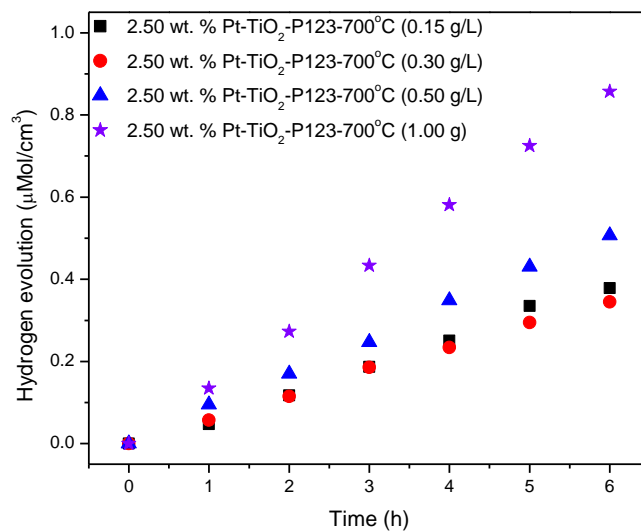


Figure A.0.9 . Changes of Cumulative Hydrogen Produced at Various Irradiation Times with Different Photocatalyst Loadings. Note: a) Mesoporous TiO₂ synthesized using Pluronic P123, doped with 2.50 wt% Pt and calcined at 700 °C, b) Photocatalyst irradiated with a UV light of $\lambda=368$ nm, c) pH = 4.00 ± 0.05 and d) 2.00 % v/v ethanol scavenger. Standard deviation for repeats ± 7.5 %.

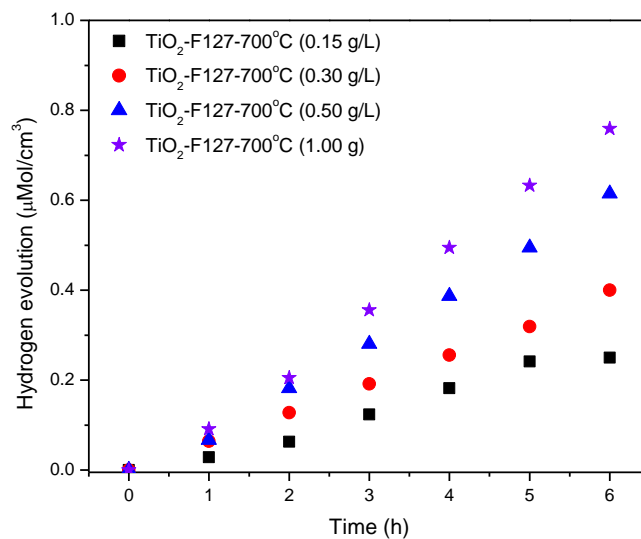


Figure A.0.10 Changes of Cumulative Hydrogen Produced at Various Irradiation Times with Different Photocatalyst Loadings. Notes: a) Mesoporous TiO₂ synthesized using Pluronic F127 , calcined at 700 °C b) Photocatalyst irradiated with a UV light of $\lambda=368$ nm, c) pH = 4.00 \pm 0.05, d) 2.00 % v/v ethanol scavenger . Standard deviation for repeats \pm 6.5 %.

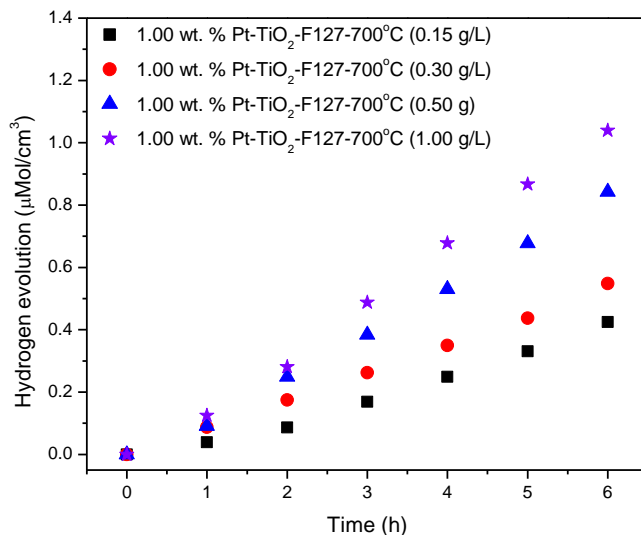


Figure A.0.11 Changes of Cumulative Hydrogen Produced at Various Irradiation Times and with Different Photocatalyst Loadings. Notes: a) Mesoporous TiO₂ synthesized using Pluronic F127, doped with 1.00 wt% and calcined at 700 °C b) Photocatalyst irradiated with a UV light of $\lambda=368$ nm) pH = 4.00 \pm 0.05 and d) 2.00 % v/v ethanol scavenger . Standard deviation for repeats \pm 6.5 %.

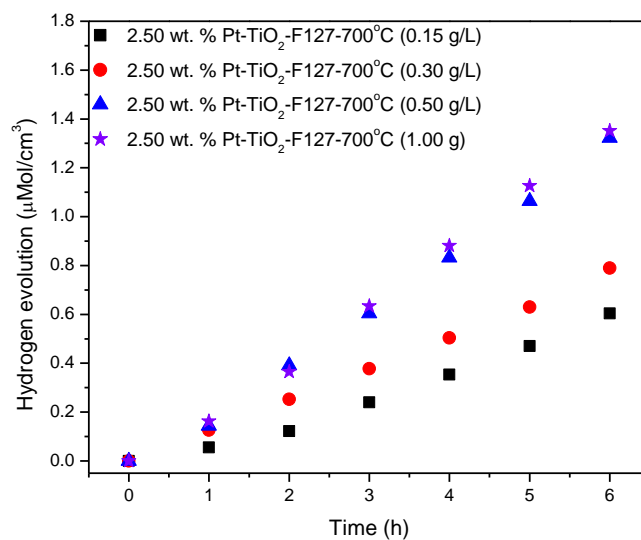


Figure A.0.12 Changes of Cumulative Hydrogen Produced At Various Irradiation Times and with Different Photocatalyst Loadings. Notes: a) Mesoporous TiO₂ synthesized using Pluronic F127, doped with 2.50 wt% Pt and calcined at 500°C, b) Photocatalyst irradiated with a UV light of $\lambda=368$ nm, c) pH = 4.00 ± 0.05 , d) 2.00 % v/v ethanol scavenger . Standard deviation for repeats ± 6.5 %.

Appendix B - Supplementary material of Chapter 4

XPS for the Photocatalysts of Mesoporous TiO₂

This appendix provides together with Chapter 4 additional information regarding the XPS analysis for the photocatalyst of the present study. In particular, Figure A.14 reports photoelectron spectroscopy (XPS) survey for the 2.50 wt. % Pt-mesoTiO₂-550 °C.

Regarding XPS it was valuable to establish the electronic state of Pt in the prepared photocatalysts. One can see in Fig. A1 (a) the peaks for Ti, O, C, and Pt elements. Regarding the carbon peak, it can be attributed to the residual carbon from the pluronic precursor.

Furthermore, and concerning the Ti2p peak at 455.85 eV, the O1 s peak at 527.25 eV and the Pt4f peak at 70.15 eV. These peaks reveal the presence of Ti, O, and Pt elements in Pt-TiO₂. Fig.A.2 shows the high-resolution XPS spectra in the 67 to 85 eV range. These findings confirm the presence of Pt, as Pt4f_{7/2} at 70.05 eV and Pt4f_{5/2} at 73.41 eV). There is also the calculated splitting of the Pt4f doublet at 3.36 eV. All these three peaks at the above-mentioned binding energies, unquestionably confirm that platinum is present in Pt-TiO₂ at the metallic state. One should notice that the reported XPS in terms of the Pt and Ti species and their reduced and oxidation states respectively are consistent with the ones reported in Figures 7a and 7b of the main text,

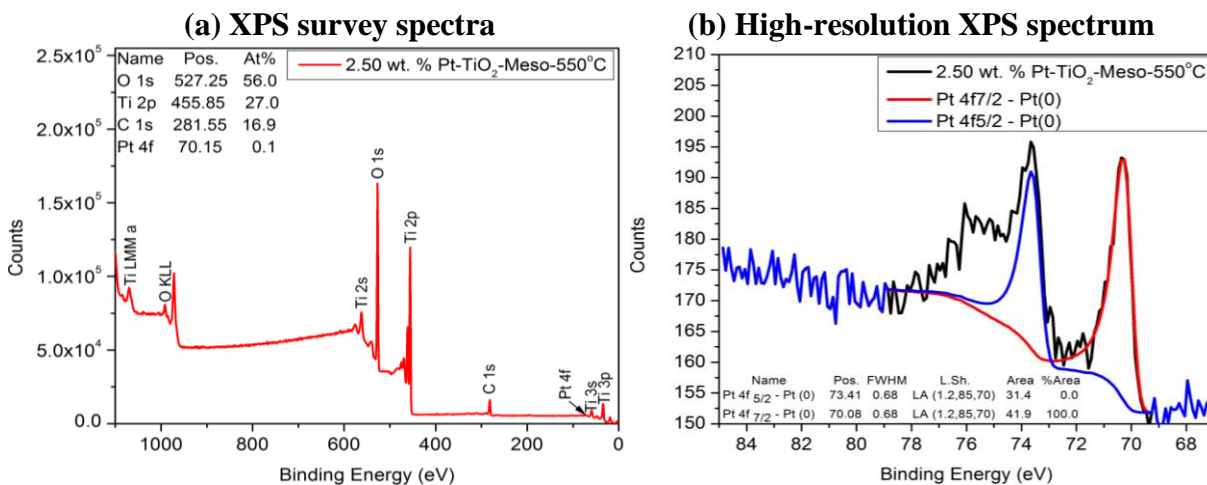


Figure B.1 X-ray photoelectron spectra (XPS) of 2.50 wt. % Pt-mesoTiO₂-550 °C.

Appendix C - Supplementary material of Chapter 4

Quantum Yield Calculation in Photo-CREC

The Quantum Yield provides photonic efficiencies in a photo-catalytic reactor. An appropriate definition for the QY is the ratio of twice H₂ produced over the photons absorbed on mesoporous TiO₂ with a wavelength smaller than 415 nm (*i.e.* 2.99 eV), such as:

$$QY = \frac{2. \text{Rate of } H_2 \text{ moles produced}}{\text{rate of photons absorbed by the photocatalyst with } \lambda \leq \lambda_0} \quad (C.1)$$

With λ_0 being the wavelength that corresponds to the value of the optical band gap for the semiconductor material considered.

In order to calculate the absorbed photons by the photocatalyst, macroscopic balances as allowed in Photo-CREC-Water II unit, includes the measurement of: a) Incident photons to the semiconductor (P_i), b) Photons transmitted by the semiconductor (P_t) and c) Photons backscattered by the semiconductor (P_{bs}).

In this regard, one can consider the calculation of the absorbed photons by the photocatalyst applying the algebraic addition of the P_i , P_t , P_{bs} ration as follows:

$$P_a(t) = P_i(t) - P_t(t) - P_{bs}(t) \quad (C.2)$$

With the units of all these terms being in photons/s.

The Quantum Yield calculation equation (C.1), in the denominator accounts for radiation variation in each location of the r , θ and λ axis as follows:

$$P_a = \frac{\int_{\lambda_{min}}^{\lambda_0} \int_0^{\infty} \int_0^{2\pi} q(\theta, z, \lambda) r d\theta dz d\lambda}{\bar{E}} \quad (C.3)$$

where \bar{E} is the average energy of a photon at a wavelength range, J/mol photon.

The near-UV lamp spectrum was characterized as reported in Figure C.1 using a spectrophotoradiometer.

Figure C.1 reports the measurements of radiation distribution in the Photo-CREC-Water II Reactor. These measurements were carried out to calculate the total absorbed radiation using eq. (C.2) and subsequently to evaluate the quantum yield with eq. (C.3).

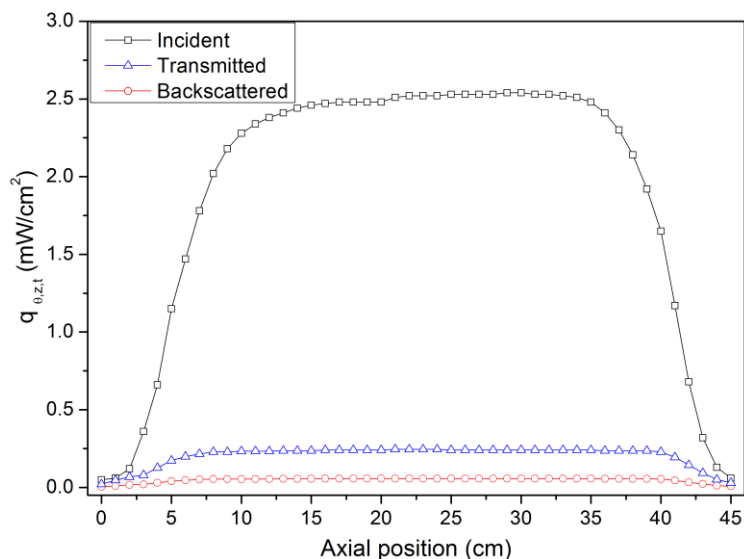


Figure C.1 Radiation distribution along axial position in the Photo-CREC-Water II Reactor. Three measurement locations were performed: a) Incident radiation on the mesoporous TiO₂ (□), b) Transmitted radiation through photocatalyst (Δ), and c) Backscattered radiation by the semiconductor (○).

Hence, the Quantum Yield is calculated taken in account the considerations of equation (A.3). Thus, the equation (4) converts to equation (A.4),

$$QY = \frac{2 \frac{dH^{\square}}{dt}}{\frac{\int_{\lambda_{\min}}^{\lambda_o} \int_0^{\infty} \int_0^{2\pi} q_a(\theta, z, \lambda) r d\theta dz d\lambda}{\bar{E}}} \quad (A.4)$$

where q_a accounts for the absorbed radiation in $\mu\text{W}/\text{cm}^2$. The denominator is calculated using macroscopic balances as described in equation (C.2).

As an illustration of this calculation, one can consider the hydrogen evolution rate exhibited by the 2.50 wt. %-Pt-TiO₂-Meso-550°C as 0.117 μmol H₂ / cm³ h¹, V_g volume of the gas phase in the storage tank as 5716 cm³ [36], P_a = 9.89 x 10¹⁷ photons/s, N_A = 6.022 x 10²³ / mol H₂, the quantum yield (QY) can be calculated as follows:

$$QY = \frac{2 * \frac{0.117 \times 10^{-6} \text{ mol H}_2}{\text{cm}^3 \text{ h}} * 5716 \text{ cm}^3 * \frac{6.022 \times 10^{23}}{\text{mol H}_2} * \frac{1 \text{ h}}{3600 \text{ s}}}{\frac{9.89 \times 10^{17} \text{ photons}}{\text{s}}} \times 100 \%$$

$$= 22.6 \%$$

Thus, on this basis one can conclude that the QY for the 2.50 wt. %-Pt-TiO₂-Meso-550°C in the present article reaches the 22.6% value.

Appendix D - Supplementary material of Chapter 4 and 5.

P_a Absorbed Photon Energy

The calculation of the P_a absorbed photon energy involves: (a) the amount of incident photons on the semiconductor surface (P_i); (b) the number of photons transmitted by the semiconductor (P_t); and (c) the photons backscattered by the semiconductor (P_{bs}).

One calculates the number of absorbed photons by the photocatalyst through the algebraic addition of the P_i , P_t , P_{bs} ratios as follows:

$$P_a(t) = P_i(t) - P_t(t) - P_{bs}(t) , \quad (\text{D.1})$$

with the units of all these terms being in photons/s.

Appendix E - Supplementary material of Chapter 4 and 5

E_{av} Average Photon Energy

The average photon energy can be calculated by using the spectrum of the lamp and the following equation:

$$E_{av} = \frac{\int_{\lambda_{min}}^{\lambda_{max}} I(\lambda)E(\lambda)d\lambda}{\int_{\lambda_{min}}^{\lambda_{max}} I(\lambda)d\lambda}, \quad (E.1)$$

where $I(\lambda)$ represents the intensity of the emitted photons in W/cm^2 , which can be calculated via $I(\lambda) \approx q(\theta, z, \lambda, t)\Delta\lambda$, with $q(\theta, z, \lambda, t)$ representing the irradiance in $W/(cm^2 \text{ nm})$ as per in Figure E.1.

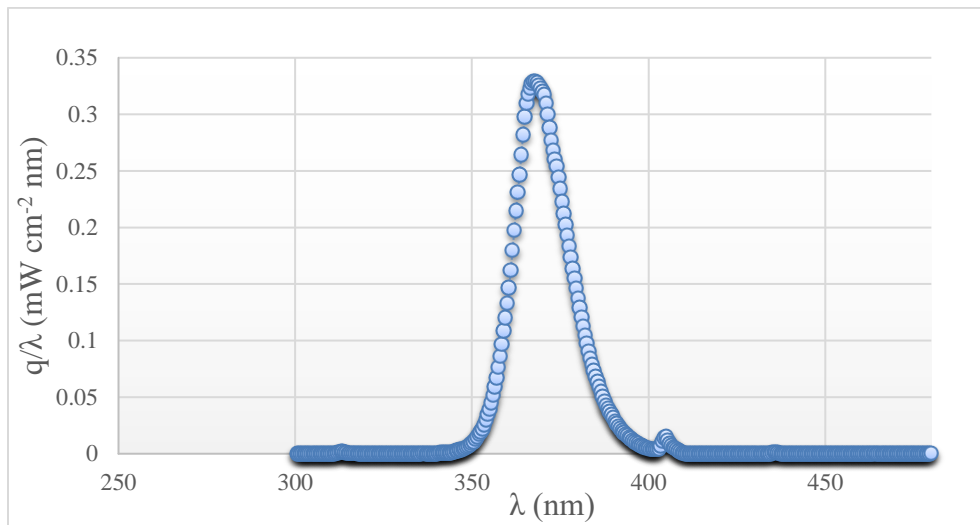


Figure E1. q at λ various wavelengths.

As a result, the average E_{av} photon energy is as follows:

$$E_{av} = \frac{\int_{\lambda_{min}}^{\lambda_{max}} q(\theta, z, \lambda, t)E(\lambda)d\lambda}{\int_{\lambda_{min}}^{\lambda_{max}} q(\theta, z, \lambda, t)d\lambda} = \frac{\int_{\lambda_{min}}^{\lambda_{max}} q(\theta, z, \lambda, t) \frac{hc}{\lambda} d\lambda}{\int_{\lambda_{min}}^{\lambda_{max}} q(\theta, z, \lambda, t)d\lambda} \quad (E.2)$$

and

$$E_{av} = \frac{hc \int_{\lambda_{\min}}^{\lambda_{\max}} \frac{q(\theta, z, \lambda, t)}{\lambda} d\lambda}{\int_{\lambda_{\min}}^{\lambda_{\max}} q(\theta, z, \lambda, t) d\lambda} = \frac{6.48 \frac{\mu W}{\text{cm}^2 \text{nm}} \left(1.8 \times 10^{-16} \frac{J \text{ nm}}{\text{photon}} \right)}{2407 \frac{\mu W}{\text{cm}^2}} = 5.35 \times 10^{-19} \frac{J}{\text{photon}} \quad (\text{E.3})$$

Appendix F - Supplementary material of Chapter 4 and 5

Rate of H• Formation

The rate of formation of H• is described in this appendix for the 1.70 wt. % Pt prepared by sol-gel method A. In this case, the H• radical concentrations at 2.5 h and 3.0 h are considered:

$$[H_2]_{t=2.5h} = 125.8 \frac{\text{nanomoles}}{\text{cm}^3}, [H_2]_{t=3.0h} = 165.4 \frac{\text{nanomoles}}{\text{cm}^3}.$$

Thus, the moles of H• radicals at these two irradiation times are:

$$H^*_{t=2.5h} = 125.8 \frac{\text{nanomoles}}{\text{cm}^3} (5715 \text{ cm}^3) \left(2 \frac{\text{moles of } H^*}{\text{moles of } H_2} \right) = 1.44 \times 10^6 \text{ nanomoles}$$

$$H^*_{t=3.0h} = 165.4 \frac{\text{nanomoles}}{\text{cm}^3} (5715 \text{ cm}^3) \left(2 \frac{\text{moles of } H^*}{\text{moles of } H_2} \right) = 1.89 \times 10^6 \text{ nanomoles}.$$

Then, the rate of H• formation can be defined as:

$$\frac{dN_{H^*}}{dt} = \frac{(1.89 \text{ nanomoles} - 1.44 \text{ nanomoles}) \times 10^6}{3.0 \text{ h} - 2.5 \text{ h}} = 9 \times 10^5 \frac{\text{nanomoles}}{\text{h}}.$$

Quantum Yield Calculation

Based on the information provided in previous Appendices, one can establish the quantum yield for 1.70 wt. % Pt prepared by sol-gel method A as:

$$\% \phi = \frac{2 \left[\frac{dN_{H^*}}{dt} \right]}{P_a} \times 100 = \frac{2 \left(9 \times 10^5 \frac{\text{nanomoles}}{\text{h}} \right) \left(\frac{1 \times 10^{-9} \text{ moles}}{\text{nanomole}} \right)}{0.0106 \frac{\text{Einstein}}{\text{h}}} \times 100\% = 16.98\%.$$

Appendix G - Supplementary material of Chapter 5

Carbon Balances

Carbon balances are required to establish the reliability of each of the experiments developed. In order to accomplish this, one has to compare the sum of moles of carbon as found in each of the species detected, with the initial moles of carbon fed to the photocatalytic reactor as ethanol.

An example of a carbon balance calculation is reported for a photocatalyst prepared via incipient impregnation with 1.00 wt. % of platinum:

(a) Moles of carbon at irradiation time zero:

$$\eta_{EtOH} = 0.342 \frac{\text{moles}}{\text{L}} (6.0 \text{ L}) = 2.05 \text{ moles of ethanol}$$
$$\eta_C = (2.05 \text{ moles}) \left(2 \frac{\text{moles of carbon}}{\text{moles of ethanol}} \right) = 4.11 \text{ moles of C}$$

(b) Moles of carbon observed at the end of the experiment in both gas and liquid phases following 6 h of irradiation:

(b.1) Moles of ethanol in both liquid and gas phase:

$$\eta_{EtOH} = 1.98 \text{ moles}$$
$$\eta_C = (1.98 \text{ moles}) \left(2 \frac{\text{moles of carbon}}{\text{moles of ethanol}} \right) = 3.96 \text{ moles of C}$$

(b.2) Moles of methane in the gas phase:

$$\eta_{CH_4} = 0.0050 \frac{\mu\text{moles}}{\text{mL}} (5716 \text{ mL}) = 2.86 \times 10^{-5} \text{ moles}$$
$$\eta_C = (2.86 \times 10^{-5} \text{ moles}) (1) = 2.86 \times 10^{-5} \text{ moles of C}$$

(b.3) Moles of ethane in the gas phase:

$$\eta_{C_2H_6} = 0.0058 \frac{\mu\text{moles}}{\text{mL}} (5716 \text{ mL}) = 3.36 \times 10^{-5} \text{ moles}$$
$$\eta_C = (3.36 \times 10^{-5} \text{ moles}) (2) = 6.72 \times 10^{-5} \text{ moles of C}$$

(b.4) Moles of acetaldehyde in the gas phase:

$$\eta_{C_2H_6O} = 0.0015 \frac{\mu\text{moles}}{\text{mL}} (5716 \text{ mL}) = 8.574 \times 10^{-6} \text{ moles}$$

$$\eta_C = (8.57 \times 10^{-6} \text{ moles})(2) = 1.71 \times 10^{-5} \text{ moles de C}$$

(b.5) Moles of carbon dioxide in both liquid and gas phase:

$$\eta_{CO_2} = 7.2 \times 10^{-4} \text{ moles}$$

$$\eta_C = (7.2 \times 10^{-4} \text{ moles})(1) = 7.210^{-4} \text{ moles of C}$$

Thus, the sum of all the moles of carbon contained in various chemical species after six hours of irradiation is:

$$\eta_c|_{t=6.0h} = (3.96 \text{ moles}) + (2.86 \times 10^{-5} \text{ moles}) +$$

$$+ (6.72 \times 10^{-5} \text{ moles}) + (1.71 \times 10^{-5} \text{ moles}) + (7.2 \times 10^{-4} \text{ moles})$$

$$\eta_c|_{t=6.0h} = 3.97 \text{ moles}$$

While this quantity is compared with the moles of ethanol fed, one can see that the percentage error in the carbon balance is as follows:

$$\% \text{ error} = \frac{C_{t=0} - C_{t=6h}}{C_{t=0}} \times 100 = \frac{4.11 - 3.97}{4.11} \times 100 = 3.37\%$$

Thus, a percentage error in the 3% range is assessed. This is acceptable and provides confirmation that all relevant species containing carbon were included in the reaction product analysis.

Appendix H - Supplementary material of Chapter 5

Ratio of •OH and H• Consumed

The ratio of •OH moles and H• moles consumed can be calculated using the following equation:

$$R = \frac{-r_{\bullet\text{OH}}}{-r_{\text{H}\bullet}} = \frac{(r_{\text{CO}_2\text{ liq}} + r_{\text{CO}_2\text{ gas}})v_{\text{CO}_2} + r_{\text{C}_2\text{H}_4\text{O}}v_{\text{C}_2\text{H}_4\text{O}} + r_{\text{H}_2\text{O}_2}v_{\text{H}_2\text{O}_2}}{r_{\text{CH}_4}v_{\text{CH}_4} + r_{\text{C}_2\text{H}_6}v_{\text{C}_2\text{H}_6} + r_{\text{H}_2}v_{\text{H}_2}},$$

with $v_{\text{CO}_2} = 6$, $v_{\text{C}_2\text{H}_4\text{O}} = 2$, $v_{\text{H}_2\text{O}_2} = 2$, $v_{\text{CH}_4} = 8$, $v_{\text{C}_2\text{H}_6} = 14$, $v_{\text{H}_2} = 2$.

For the 2.50 wt. % Pt–TiO₂ photocatalyst prepared via sol-gel B, $\dot{r}_{\text{CO}_2\text{ gas}} = 1.63$ nanomoles/cm³h, $\dot{r}_{\text{C}_2\text{H}_4\text{O}} = 1.246$ nanomoles/cm³h, $\dot{r}_{\text{CH}_4} = 0.227$ nanomoles/cm³h, $\dot{r}_{\text{C}_2\text{H}_6} = 2.066$ nanomoles/cm³h, $\dot{r}_{\text{H}_2} = 100$ nanomoles/cm³h. These values were obtained from Figures of photocatalytic hydrogen evolutions. The concentration with respect to time for hydrogen peroxide was tracked experimentally using titration with a solution of potassium permanganate (KMnO₄) [11], the rate $r_{\text{H}_2\text{O}_2} = 1.77 \times 10^{-12}$ nanomoles/h was found. For $\dot{r}_{\text{CO}_2\text{ liq}}$ the value of 39.16 nanomoles/cm³h was assessed using thermodynamic equilibrium calculations, assuming both ideal gas and ideal solution assumptions.

$$\begin{aligned} R &= \frac{-r_{\bullet\text{OH}}}{-r_{\text{H}\bullet}} \\ &= \frac{6 \left(40.790 \frac{\text{nanomoles}}{\text{cm}^3\text{h}} (5715 \text{ cm}^3) \right) + 2 \left(1.246 \frac{\text{nanomoles}}{\text{cm}^3\text{h}} (5715 \text{ cm}^3) \right) + 2 \left(2.95 \times 10^{-16} \frac{\text{nanomoles}}{\text{cm}^3\text{h}} (6000 \text{ cm}^3) \right)}{2 \left(0.227 \frac{\text{nanomoles}}{\text{cm}^3\text{h}} (5715 \text{ cm}^3) \right) + 14 \left(2.066 \frac{\text{nanomoles}}{\text{cm}^3\text{h}} (5715 \text{ cm}^3) \right) + 2 \left(100 \frac{\text{nanomoles}}{\text{cm}^3\text{h}} (5715 \text{ cm}^3) \right)} \\ &= 1.07 \end{aligned}$$

Appendix I -Royal Society of Chemistry License for Chapter 2

ROYAL SOCIETY OF CHEMISTRY LICENSE TERMS AND CONDITIONS

Feb 07, 2018

This Agreement between Dr. Jesus Fabricio Guayaquil Sosa ("You") and Royal Society of Chemistry ("Royal Society of Chemistry") consists of your license details and the terms and conditions provided by Royal Society of Chemistry and Copyright Clearance Center.

License Number	4284410872347
License date	Feb 07, 2018
Licensed Content Publisher	Royal Society of Chemistry
Licensed Content Publication	Chemical Society Reviews
Licensed Content Title	Heterogeneous photocatalyst materials for water splitting
Licensed Content Author	Akihiko Kudo,Yugo Miseki
Licensed Content Date	Nov 18, 2008
Licensed Content Volume	38
Licensed Content Issue	1
Type of Use	Thesis/Dissertation
Requestor type	non-commercial (non-profit)
Portion	figures/tables/images
Number of figures/tables/images	1
Format	electronic
Distribution quantity	1
Will you be translating?	no
Order reference number	
Title of the thesis/dissertation	Photocatalytic Hydrogen Production using a Mesoporous TiO ₂ Doped with Pt: Semiconductor Synthesis, Oxidation-Reduction Network and Quantum Efficiencies
Expected completion date	Feb 2018
Estimated size	170
Requestor Location	Dr. Jesus Fabricio Guayaquil Sosa Western Univeristy London, ON N6H4T7 Canada Attn: Dr. Jesus Fabricio Guayaquil Sosa
Billing Type	Invoice
Billing Address	Dr. Jesus Fabricio Guayaquil Sosa 690 Western Univeristy London, ON N6H4T7 Canada Attn: Dr. Jesus Fabricio Guayaquil Sosa
Total	
Terms and Conditions	

This License Agreement is between {Requestor Name} ("You") and The Royal Society of Chemistry ("RSC") provided by the Copyright Clearance Center ("CCC"). The license consists of your order details, the terms and conditions provided by the Royal Society of Chemistry, and the payment terms and conditions.

RSC / TERMS AND CONDITIONS

INTRODUCTION

The publisher for this copyrighted material is The Royal Society of Chemistry. By clicking "accept" in connection with completing this licensing transaction, you agree that the following terms and conditions apply to this transaction (along with the Billing and Payment terms and conditions established by CCC, at the time that you opened your RightsLink account and that are available at any time at .

LICENSE GRANTED

The RSC hereby grants you a non-exclusive license to use the aforementioned material anywhere in the world subject to the terms and conditions indicated herein. Reproduction of the material is confined to the purpose and/or media for which permission is hereby given.

RESERVATION OF RIGHTS

The RSC reserves all rights not specifically granted in the combination of (i) the license details provided by you and accepted in the course of this licensing transaction; (ii) these terms and conditions; and (iii) CCC's Billing and Payment terms and conditions.

REVOCAION

The RSC reserves the right to revoke this license for any reason, including, but not limited to, advertising and promotional uses of RSC content, third party usage, and incorrect source figure attribution.

THIRD-PARTY MATERIAL DISCLAIMER

If part of the material to be used (for example, a figure) has appeared in the RSC publication with credit to another source, permission must also be sought from that source. If the other source is another RSC publication these details should be included in your RightsLink request. If the other source is a third party, permission must be obtained from the third party. The RSC disclaims any responsibility for the reproduction you make of items owned by a third party.

PAYMENT OF FEE

If the permission fee for the requested material is waived in this instance, please be advised that any future requests for the reproduction of RSC materials may attract a fee.

ACKNOWLEDGEMENT

The reproduction of the licensed material must be accompanied by the following acknowledgement:

Reproduced ("Adapted" or "in part") from {Reference Citation} (or Ref XX) with permission of The Royal Society of Chemistry.

If the licensed material is being reproduced from New Journal of Chemistry (NJC), Photochemical & Photobiological Sciences (PPS) or Physical Chemistry Chemical Physics (PCCP) you must include one of the following acknowledgements:

For figures originally published in NJC:

Reproduced ("Adapted" or "in part") from {Reference Citation} (or Ref XX) with permission of The Royal Society of Chemistry (RSC) on behalf of the European Society for Photobiology, the European Photochemistry Association and the RSC.

For figures originally published in PPS:

Reproduced ("Adapted" or "in part") from {Reference Citation} (or Ref XX) with permission of The Royal Society of Chemistry (RSC) on behalf of the Centre National de la Recherche Scientifique (CNRS) and the RSC.

For figures originally published in PCCP:

Reproduced ("Adapted" or "in part") from {Reference Citation} (or Ref XX) with permission of the PCCP Owner Societies.

HYPertext LINKS

With any material which is being reproduced in electronic form, you must include a

hypertext link to the original RSC article on the RSC's website. The recommended form for the hyperlink is <http://dx.doi.org/10.1039/DOI> suffix, for example in the link <http://dx.doi.org/10.1039/b110420a> the DOI suffix is 'b110420a'. To find the relevant DOI suffix for the RSC article in question, go to the Journals section of the website and locate the article in the list of papers for the volume and issue of your specific journal. You will find the DOI suffix quoted there.

LICENSE CONTINGENT ON PAYMENT

While you may exercise the rights licensed immediately upon issuance of the license at the end of the licensing process for the transaction, provided that you have disclosed complete and accurate details of your proposed use, no license is finally effective unless and until full payment is received from you (by CCC) as provided in CCC's Billing and Payment terms and conditions. If full payment is not received on a timely basis, then any license preliminarily granted shall be deemed automatically revoked and shall be void as if never granted. Further, in the event that you breach any of these terms and conditions or any of CCC's Billing and Payment terms and conditions, the license is automatically revoked and shall be void as if never granted. Use of materials as described in a revoked license, as well as any use of the materials beyond the scope of an unrevoked license, may constitute copyright infringement and the RSC reserves the right to take any and all action to protect its copyright in the materials.

WARRANTIES

The RSC makes no representations or warranties with respect to the licensed material.

INDEMNITY

You hereby indemnify and agree to hold harmless the RSC and the CCC, and their respective officers, directors, trustees, employees and agents, from and against any and all claims arising out of your use of the licensed material other than as specifically authorized pursuant to this licence.

NO TRANSFER OF LICENSE

This license is personal to you or your publisher and may not be sublicensed, assigned, or transferred by you to any other person without the RSC's written permission.

NO AMENDMENT EXCEPT IN WRITING

This license may not be amended except in a writing signed by both parties (or, in the case of "Other Conditions, v1.2", by CCC on the RSC's behalf).

OBJECTION TO CONTRARY TERMS

You hereby acknowledge and agree that these terms and conditions, together with CCC's Billing and Payment terms and conditions (which are incorporated herein), comprise the entire agreement between you and the RSC (and CCC) concerning this licensing transaction, to the exclusion of all other terms and conditions, written or verbal, express or implied (including any terms contained in any purchase order, acknowledgment, check endorsement or other writing prepared by you). In the event of any conflict between your obligations established by these terms and conditions and those established by CCC's Billing and Payment terms and conditions, these terms and conditions shall control.

JURISDICTION

This license transaction shall be governed by and construed in accordance with the laws of the District of Columbia. You hereby agree to submit to the jurisdiction of the courts located in the District of Columbia for purposes of resolving any disputes that may arise in connection with this licensing transaction.

LIMITED LICENSE

The following terms and conditions apply to specific license types:

Translation

This permission is granted for non-exclusive world English rights only unless your license was granted for translation rights. If you licensed translation rights you may only translate this content into the languages you requested. A professional translator must perform all translations and reproduce the content word for word preserving the integrity of the article.

Intranet

If the licensed material is being posted on an Intranet, the Intranet is to be password-protected and made available only to bona fide students or employees only. All content posted to the Intranet must maintain the copyright information line on the bottom of each image. You must also fully reference the material and include a hypertext link as specified above.

Copies of Whole Articles

All copies of whole articles must maintain, if available, the copyright information line on the bottom of each page.

Other Conditions

v1.2

Gratis licenses (referencing \$0 in the Total field) are free. Please retain this printable license for your reference. No payment is required.

If you would like to pay for this license now, please remit this license along with your payment made payable to "COPYRIGHT CLEARANCE CENTER" otherwise you will be invoiced within 48 hours of the license date. Payment should be in the form of a check or money order referencing your account number and this invoice number {Invoice Number}.

Once you receive your invoice for this order, you may pay your invoice by credit card.

Please follow instructions provided at that time.

Make Payment To:

Copyright Clearance Center
29118 Network Place
Chicago, IL 60673-1291

For suggestions or comments regarding this order, contact Rightslink Customer Support: customercare@copyright.com or +1-855-239-3415 (toll free in the US) or +1-978-646-2777.

Questions? customercare@copyright.com or +1-855-239-3415 (toll free in the US) or +1-978-646-2777.

Curriculum Vitae

Jesús Fabricio Guayaquil Sosa

Post-secondary Education and Degrees:

Doctor of Philosophy in Chemical and Biochemical Engineering
The University of Western Ontario
London, Ontario, Canada
2013-2018 Ph.D.

Master of Science in Chemical Engineering
Autonomous Metropolitan University – Campus I
Mexico city, Mexico
2010-2012 M.Sc.

Bachelor of Chemical Engineering
Autonomous Metropolitan University – Campus I
Mexico city, Mexico
2004-2009 B.Eng.

Honours and Awards:

Full Scholarship for International PhD studies.
Sponsored by the Federal Government of Mexico through the
National Council of Science and Technology (CONACYT).
2013-2018

Supplement Bursary for International PhD studies.
Sponsored by the Federal Government of Mexico through the
Secretariat of Public Education (SEP).
2013-2018

Dean's Honours List with a GPA of 98/100.
Autonomous Metropolitan University – Campus I, Mexico city,
Mexico. 2012

Dean's Honours List with a GPA of 97/100.
Autonomous Metropolitan University – Campus I, Mexico city,
Mexico. 2009.

Related Work Experience

Research Assistant
The University of Western Ontario
2013-2017

Teaching Assistant
The University of Western Ontario
2014-2017

Publications:

International peer-reviewed publications

1. J.F. Guayaquil-Sosa, B. Serrano-Rosales, P. J. Valadés-Pelayo, H. de Lasa. (2017). Photocatalytic Hydrogen Production using Mesoporous TiO₂ Doped with Pt. *Applied Catalysis B: Environmental*, 211, 337-348. Impact Factor: 9.446.
2. J.F. Guayaquil-Sosa.; Calzada, A.; Serrano, B.; Escobedo, S.; de Lasa, H. (2017). Hydrogen Production via Water Dissociation Using Pt–TiO₂ Photocatalysts: An Oxidation–Reduction Network. *Catalysts*, 7, 324. Impact Factor: 3.082.
3. B. Serrano Rosales, Jesús Moreira del Rio, Jesús Fabricio Guayaquil Sosa, H. de Lasa. (2016) Photodegradation Efficiencies in a Photo-CREC Water-II Reactor Using Several TiO₂ Based Catalysts. *International Journal of Chemical Reactor Engineering*, 14, (3), 685-701. Impact Factor: 0.623.
4. P.J. Valadés-Pelayo, F. Guayaquil Sosa, B. Serrano, H. de Lasa. (2015). Eight Lamp Externally Irradiated Bench-Scale Photocatalytic Reactor: Scale-up and Performance Prediction. *Chemical Engineering Journal*, 282, 142-151. Impact Factor: 6.216.
5. P. J. Valadés-Pelayo, F. Guayaquil Sosa, B. Serrano, H. de Lasa. (2015). Photocatalytic Reactor Under Different External Irradiance Conditions: Validation of a Fully Predictive Radiation Absorption Model. *Chemical Engineering Science*, 126, 42-54. Impact Factor: 2.895.